Computer Simulations of Li–N–H Systems

Phillip L. Marks

St Cross College

A thesis submitted for the degree of

Doctor of Philosophy

Inorganic Chemistry Laboratory

University of Oxford

Trinity Term 2019

> “Good programmers know what to write. Great ones know what to rewrite (and reuse).”
>
> **Eric S. Raymond**[1]

Contents

Abstract

The Li–N–H system (lithium compounds with nitrogen and/or hydrogen based anions) is a promising family of materials for chemical energy storage applications; the development of efficient energy storage materials is one of the key challenges for global renewable energy utilisation. The Li–N–H system is of importance for both hydrogen storage and in facilitating the storage of energy as ammonia. Lithium hydride and lithium imide, two materials in this family, were investigated in this thesis.

The interactions of ammonia on the surface of lithium hydride represent the hydrogen formation step in the lithium amide-lithium hydride hydrogen storage system. The study of these interactions through DFT and MD simulations has led to new insights from geometric considerations of ammonia into both its movement across the surface and its stable configuration. Molecules on the lithium hydride surface with tetrahedral geometries closely related to ammonia were investigated to better understand the surface interactions due to the distorted tetrahedral structure of ammonia. This lithium hydride surface study is the foundation for future investigations of ammonia on more complex Li–N–H surfaces, namely lithium imide, which is the dehydrogenated form of the hydrogen store, and itself an active catalyst for ammonia decomposition. The structure and dynamics of bulk lithium imide were investigated between 300–700 K with a particular attention to lithium-ion mobility through the structure. The evolution of the structure was observed from ensemble average nitrogen environments of the hydrogen and lithium ions. On heating to 700 K, a monoclinic to cubic phase transition ($I112/b \rightarrow Fm\bar{3}m$) was observed with the structural transition around 500 K. Frenkel defect formations with lithium ions displaced from tetrahedra into octahedra were traced through the structure and two different defect arrangements were obtained at low-temperature using different temperature gradients.

Acknowledgements

First and foremost, I would like to thank Bill David for his support at all stages of my DPhil and encouraging me to pursue my own academic interests. I would like to thank Josh Makepeace and Tom Wood for their encouragement and guidance which has gotten me through these past four years. Josh, I thank for his patience, calming influence and all of his proofreading. He always reassured me that I would finish this thesis at times when I didn't believe it for myself. Tom, I thank for always being able to make me laugh and his brilliance in programming; without his help with Python this project would not have been possible. I would also like to thank Keith Refson for his time and advice. My fellow DPhil's, Jake and Jonny, I thank for their individual acts of kindness (especially whilst writing up), and the part II students (Alisha, Fergus, Jack, Mikey and Sophie-Ann) for filling the office with laughter—it would not have been anywhere near as fun without them! Lastly, I'd like to thank my friends (especially the blues team of OURC) and family. My parents for their unwavering belief in me throughout all of my pursuits (however seemingly far-fetched), and to my partner Charlotte, whose support and kindness I would be lost without.

Abbreviations

°C	degrees Celsius
K	Kelvin
GPa	gigapascal
Å	angstrom, 10^{-10} m
ps	picosecond, 10^{-12} s
fs	femtosecond, 10^{-15} s
ppm	parts per million
wt%	weight percent
ICSD	Inorganic Crystal Structure Database
DFT	Density Functional Theory
MD	Molecular Dynamics
CASTEP	Cambridge Serial Total Energy Package
SCARF	Scientific Computing Application Resource for Facilities

1 Introduction

1.1 Transitioning to renewable energy technologies

Arguably, the greatest challenge of the early twenty-first century is ending our reliance on burning fossil fuels (coal, oil, natural gas) and transitioning to renewable energy sources. Since the beginning of the Industrial Revolution some 250 years ago the use of coal, oil and gas has mechanised unprecedented social, economic and technological advancements and with it our global dependence on fossil fuels. But fossil fuels are a finite resource formed over geological timescales and substantially exhausted over the past two centuries. And, of more immediate significance and importance, the combustion of fossil fuels and attendant release of carbon dioxide is the principal contributor to global warming; CO_2 corresponds to 77 % of the impact of greenhouse gas emission.

The Intergovernmental Panel on Climate Change (IPCC) 5th Assessment Report concluded, with 95% confidence, that the rise in global temperature over the past 50 years has been the result of human-caused greenhouse gases.[2] Since the beginning of the Industrial Revolution, atmospheric CO_2 levels have increased from ∼280 ppm to over 400 ppm, and half of the anthropogenic CO_2 emissions between 1750–2010 have occurred since 1970.[2]. Current global temperatures are 1 °C above pre-industrial levels and this is the direct cause of both rising sea levels and more extreme weather events.[3] Limiting global warming to below 2 °C from pre-industrial levels had been the target; however, this was recently revised down to 1.5 °C.[4] This reduction limits ecosystem damage and species loss, and reduces by two-thirds (37 %→14 %) the human population that is exposed to severe heat.[3] While statistics on how long fossil fuels reserves will last vary considerably, even the most optimistic forecasts do not predict supplies to last beyond the early twenty-second century. For example, British Petroleum estimates that proven sources of oil and natural gas will run out in 50 years and coal in 110 years.[5] McGlade and Ekins calculated that to avert the critical 2 °C temperature rise from pre-industrial times, much of the known fossil fuel reserves (33 % of oil, 50 % of gas, 80 % of coal) have to remain unused.[6] The scientific evidence strongly asserts that the fossil fuel era must end and that global energy demands must be met entirely by renewable sources; this is very likely to include nuclear energy. The energy-transition to renewables presents many technical challenges that must be overcome but it is an imperative to ensure the future of humanity.

Renewable energy technologies such as solar and wind energy have reached a maturity where unsubsidised costs are competitive with traditional fossil fuels.[7] Renewable electricity prices vary significantly around the world depending on the different renewable source availability. And renewables have substantial challenges such as intermittency and lack of portability. The solution to both of these is energy storage, as the capture of energy for use elsewhere in place and later in time. Transportation is a large contributor to greenhouse gases (14 %)[2] and represents a major energy storage problem because portable systems inherently require a high gravimetric energy density, and this is difficult to accomplish. The challenge for global renewable energy utilisation is not generation but storage.

Batteries and pumped hydroelectric have been the traditional methods of storing energy, with pumped hydroelectric the most important grid-scale storage method. Batteries, unlike pumped hydroelectric, are portable; however, electrochemical storage systems have low gravimetric and volumetric energy densities compared with fossil fuels. Short battery lifetimes due to material degradation in recharging and the forecasted global shortage of cobalt and lithium (by 2050) also means that the costs of lithium-ion batteries may simply be too high for global energy storage.[8] The first lithium-ion battery cathode was invented in 1980 by J. B. Goodenough *et al.* (Li_xCoO_2)[9] and in the following forty years of lithium-ion battery research, even the most promising materials (such as the lithium-air battery)[10] do not have a high enough energy density. Chemical energy storage is a solution because it has a greater energy density than the highest performing batteries (both volumetric and gravimetric), its stored energy is released quickly and it can be used both portably or at grid-scale. Renewable chemical energy storage is a like-for-like replacement for fossil fuels and ammonia and hydrogen are both promising candidates.

1.2 Storing energy as hydrogen

Hydrogen is an attractive chemical energy store because it has three times the energy density of fossil fuels by mass, at $142\,\mathrm{MJ\,kg^{-1}}$and is the most abundant element in the universe.[11] [12] It can either be combusted like gasoline, or converted to electricity in a fuel cell. Although hydrogen is the most abundant element in the universe, on Earth, it is almost entirely found in compounds bonded to other elements. The challenge is to develop systems that produce hydrogen, store it safely and store it at grid-scale under realistic operating conditions.

The direct use of hydrogen is, however, both impractical and energetically unfavourable. Currently, hydrogen production at large-scale is either by steam methane reforming or coal gasification, both unmistakably carbon dioxide emitting processes. Most hydrogen production (80–85%) is by steam-methane reforming which is an energetically intensive process as hydrogen forms in the presence of a nickel based catalyst at high temperature

(900–1200 K) and pressure (5–25 bar):[11]

$$\mathrm{CH_4 + H_2O\ (g) \longrightarrow CO + 3\,H_2} \qquad \Delta H^{\ominus} = 210\,\mathrm{kJ\,mol^{-1}} \tag{1.1}$$

$$\mathrm{CO + H_2O\ (g) \longrightarrow CO_2 + H_2} \qquad \Delta H^{\ominus} = -42\,\mathrm{kJ\,mol^{-1}} \tag{1.2}$$

These processes are expensive if the hydrogen is directly used as an energy store given the low cost of fossil fuels. To date, it has therefore generally been more profitable to use hydrogen as a feedstock to manufacture ammonia or methanol. In the near future, electrolytic hydrogen production, where water is split using renewable electricity into hydrogen and oxygen in an electrolysis cell will afford the possibility of a solution.[13] The cost of H_2 production by this means depends almost entirely on the price of electricity. The technology is not currently as competitive as fossil fuel-based hydrogen production, due to the high capital costs and lifespan of the electrolyser membrane from degradation. However, it is a highly efficient method of producing pure hydrogen and process efficiencies are expected to shortly reach 85–90%.[13]

Once produced, hydrogen is difficult to store efficiently because it is a very light gas at room temperature and so has an inherently low volumetric density at atmospheric pressure. Energy density may be improved by either compressing hydrogen gas and storing it at high pressure or liquefying hydrogen by cooling it below 20 K. Both storage mechanisms require a large amount of energy; for example, initial liquefaction consumes around 30% of the stored energy content of hydrogen due to compression and cooling.[14] There are also significant safety concerns in either storing hydrogen at high-pressure or as a liquid that requires a sub-20 K temperature to be maintained. The automotive industry however has opted to use high-pressure (700 bar) storage as an intermediate solution in fuel cell electric vehicles (FCEVs), undeterred by hydrogen production and storage being so energy-intensive.[15] To give an idea of scale, 5 kg of hydrogen at 700 bar requires a 120 L tank (2–3 times the volume of a gasoline tank in a typical car) and this would give a driving range of ∼300 miles. While this may end up being acceptable for vehicles, it is not feasible

for large scale storage and distribution. The direct use of hydrogen at high pressure is not an energy storage solution beyond prototype vehicles, for hydrogen to realistically replace fossil-fuels globally it must be stored efficiently at high volumetric energy densities, and this first requires the development of effective hydrogen storage materials.

The U.S. Department of Energy determined that hydrogen storage systems must meet performance targets of 7.5 wt% gravimetric hydrogen density and 70 kg m^{-3} volumetric hydrogen density to have commercial viability in the light-duty vehicle market.[16] Storing hydrogen in a solid state material could provide the energy density necessary for its practical use. There are two methods by which this could be accomplished, either by physisorption or chemisorption.[17] [18] In physisorption, hydrogen molecules are stored inside porous materials by weak Van der Waals interactions to the interior surface of the pores. The main issue is that due to being a weak interaction, low temperatures ($< 150\,K$) are required for significant physisorption.[19] Carbon nanostructures, zeolites and metal-organic frameworks have all been investigated. However, their gravimetric and volumetric hydrogen densities are poor.[20] [21] [22]

In chemisorption, the hydrogen-hydrogen bond is broken and hydrogen atoms are bonded within the storage material. Materials which store hydrogen by chemisorption can be broadly categorised into reversible metal hydrides and complex hydrides.[17] Metal hydrides can be formed at elevated temperatures between hydrogen and a wide range of transition metals and alloys: this versatility made the compounds a promising proposition. Although many metal hydrides can reversibly store hydrogen at moderate conditions, in general due to the nature of using a transition metal the compounds are heavy (low gravimetric energy density) and often contain expensive rare-earth metals.[23] The development of lightweight metal hydrides remains a challenge. Complex hydrides contain hydrogen bonded to two or more atoms which are not transition metals. The first complex hydride which was shown to have attractive hydrogen storage properties was Ti-doped sodium alanate ($NaAlH_4$) in 1997 which can store 4.2 wt% of hydrogen reversibly at $\sim 200\,°C$.[24] This initial success has been replicated in few complex hydrides since due to insufficient hydrogen densities or poor reversibility, despite substantial research effort into alanates,

amides, ammines and borohydrides.[23] Of these the lithium nitride-imide-amide system (Li–N–H hydrogen storage system) has shown the most promise for reversible solid-state hydrogen storage and has attracted significant attention due to its theoretical 10.4 wt% hydrogen capacity.[25, 26, 27, 28]

The Li–N–H hydrogen storage system was first investigated by Dafert and Miklauz in 1910 with the reported formation of trilithium ammonium (Li_3NH_4) from the uptake of hydrogen in lithium nitride (Li_3N).[29, 30] It was almost a century later however that lithium nitride was highlighted as a solid-state hydrogen storage material by Chen *et al.*, and the products of its reaction with hydrogen were found instead to be a mixture of lithium amide ($LiNH_2$) and two equivalents of lithium hydride (LiH).[25] This process was reported to occur via the following two-step lithium imide-mediated (Li_2NH) mechanism:

$$Li_3N + H_2 \rightleftharpoons Li_2NH + LiH \qquad \Delta_f H^{\ominus} = -148\,\mathrm{kJ\,mol^{-1}} \tag{1.3}$$

$$Li_2NH + H_2 \rightleftharpoons LiNH_2 + LiH \qquad \Delta_f H^{\ominus} = -45\,\mathrm{kJ\,mol^{-1}} \tag{1.4}$$

The combination of equation 1.3 and 1.4 gives a theoretical 10.4 wt % hydrogen capacity and 100 $\mathrm{kg\,m^{-3}}$ volumetric hydrogen density (more dense than liquid hydrogen at 70 $\mathrm{kg\,m^{-3}}$). The lithium imide-nitride transition (backward reaction of eq. 1.3) is very endothermic and so high operating temperatures of above 430 °C are required for reversibility:[25] for this reason and the high gravimetric hydrogen density of eq. 1.4 alone, the lithium amide-imide system has been the focus of the hydrogen storage community. The conversion of lithium amide to lithium imide (reverse reaction) is much less endothermic and therefore hydrogen can be reversibly stored at more moderate conditions of 230 °C and 1–10 bar pressure.[31, 32] Lithium amide-imide has a 6.5 wt % hydrogen storage capacity and a 67.3 $\mathrm{kg\,m^{-3}}$ volumetric hydrogen density.[31]

Lithium amide had been previously overlooked as a hydrogen storage material because it was known to decompose to the imide with release of ammonia above 360 °C (see eq. 1.5).[33] It is only through the addition of lithium hydride in the composite system that

lithium amide can reversibly uptake and release hydrogen.[26] Ichikawa *et al.* revised the mechanism for hydrogen desorption from lithium amide (reverse of eq. 1.4), showing lithium amide to decompose by an ammonia-mediated two-step process:[34]

$$2\,\mathrm{LiNH_2} \rightleftharpoons \mathrm{Li_2NH} + \mathrm{NH_3} \tag{1.5}$$

$$\mathrm{LiH} + \mathrm{NH_3} \rightleftharpoons \mathrm{LiNH_2} + \mathrm{H_2} \tag{1.6}$$

The hydrogen desorption step is ammonia reacting with lithium hydride which reforms the amide (eq. 1.6). This mechanism was supported by Isobe *et al.*'s work but with the addition of the momentary formation of an activated [$\mathrm{LiNH_4}$] complex during hydrogen desorption.[35] Hu and Ruckenstein demonstrated the reaction between LiH + $\mathrm{NH_3}$ to be ultra-fast and this makes experimental studies intractable.[36] The lithium amide-imide system is a promising hydrogen storage candidate due to its excellent hydrogen reversibility and long-term cycling stability demonstrated from 6.8 wt% hydrogen stored over 850 hydriding and dehydriding cycles.[37, 38]

1.3 Computational studies on Li–N–H system for hydrogen storage

The Li–N–H system is an interesting problem for computational study, both to understand its high hydrogen capacity (6.5 wt%) and to determine the reaction mechanism at an atomic scale. The lithium amide formation mechanism (eq. 1.6) within the amide-imide system is of particular interest *in silico* due to its reported ultra-fast reaction[36] which is contrary to the literature from the original authors of the lithium nitride-amide-imide system.[26, 34, 35]

The computational research on lithium amide formation to date has been at the scale of few atoms to small cluster models of lithium hydride. Kar *et al.* investigated the experimentally reported mechanisms using high-level electronic structure calculations of

gas-phase LiH + NH_3 molecules.[39] An energy profile was produced from a series of transition states for the two molecules, and at each point in the reaction the structures were fully geometry optimised. The desorption of hydrogen was calculated to proceed via intermediates with an empirical formula $LiNH_4$, consistent with the conclusions of Isobe *et al.*[35] Firstly, HLi—NH_3 is formed; secondly, a hydrogen in the ammonia molecule moves close enough to the hydride to form H_2 (transition state); thirdly, H_2 pivots around the lithium resulting in the arrangement H_2—$LiNH_2$, and lastly, H_2 is weakly bound to $LiNH_2$ and thus desorbs. The overall reaction is exothermic with $\Delta_f H^{\ominus} = -44\,\mathrm{kJ\,mol^{-1}}$ and H_2 is formed by a H contribution from both molecular species.

A two molecule model is insufficient to comprehensively understand the interactions of ammonia on lithium hydride and hence Yamane *et al.* subsequently published two papers using small clusters of LiH.[40, 41] These clusters are a computationally inexpensive way to approximate a full surface model, and can be viewed as an extremely disordered LiH surface. Yamane's first paper was on the interaction between NH_3 and a Li_2H_2 cluster performed by *ab initio* molecular dynamics (with PBE exchange-correlation functional). Li_2H_2 is the smallest possible cluster and was used to evaluate the reaction dynamics (given that only stationary points had been considered for LiH), before larger clusters could be investigated in the second paper. In the initial configuration, Li_2H_2 was arranged in a square using geometry optimised Li—H bond lengths and the lithium ions were fixed in position, NH_3 was then placed above a lithium ion with the hydrogen facing away from the cluster. The desorption of hydrogen was observed above 700 K with H_2 formed between H^- from LiH and $\overset{\delta\oplus}{H}$ from NH_3. The hydride vacancy consequently created was filled by the resultant $NH_2{}^-$. In the second paper, Li_nH_n clusters (n=1–4) were evaluated from a series of structural optimisations. NH_3 was moved progressively closer to Li_nH_n and at each H—H distance the structure was optimised until a distance where hydrogen desorption occurred. The calculation setup was the same as before with NH_3 above a lithium ion. The same hydrogen formation mechanism was observed for all of the Li_nH_n clusters, where NH_3 and Li_nH_n each contributed a H and $NH_2{}^-$ filled the newly created hydride vacancy; the energies however were dependant on the cluster size. A series of equivalent structural optimisations were performed for NH_3 on a small LiH slab model ($Li_{32}H_{32}$). However,

because H_2 did not dissociate from the surface in these static calculations, the slab model was dismissed in favour of the less expensive cluster models.

1.4 Ammonia: a future energy vector

The Li–N–H system is also of importance in understanding important aspects of the storage of energy as ammonia. Ammonia is an attractive hydrogen carrier and alternative to solid-state hydrogen storage materials for a number of significant reasons: hydrogen can be stored as liquid ammonia at moderate conditions (10 bar at room temperature) and ammonia has a higher gravimetric (17.8 wt%) and volumetric (121 $\mathrm{kg\,m^{-3}}$) hydrogen density than the best performing reversible solid-state storage materials, such as lithium imide-lithium amide (at 6.5 wt% and 67.3 $\mathrm{kg\,m^{-3}}$ respectively).[42] Ammonia is also one of the largest chemical commodities produced globally due to its use as a fertilizer that enables the provision of food for almost half of the world's population.[43] It therefore benefits from the fact that its synthesis and handling are mature technologies at industrial scale. For use as an energy vector, ammonia must either be completely decomposed and used in a H_2 fuel cell, partially decomposed for combustion or used directly in solid oxide fuel cells. The decomposition of ammonia given below is carbon free at point of use:

$$\mathrm{NH_3(g)} \rightleftharpoons \frac{1}{2}\mathrm{N_2} + \frac{3}{2}\mathrm{H_2(g)} \qquad \Delta_\mathrm{f}H^\ominus = 46\,\mathrm{kJ\,mol^{-1}} \tag{1.7}$$

The viability of ammonia as a hydrogen carrier depends on the development of efficient, low-cost decomposition catalysts. Ruthenium-based catalysts are the most active for cracking ammonia, with highest activities observed for ruthenium supported on nanoparticles with a promoter species; however, the expense of these materials makes ruthenium-based catalysts incompatible with large-scale use.[44] [45] [46] [47] Additionally, any catalyst developed must be capable of producing high purity hydrogen, so that the hydrogen can be efficiently converted into energy in a proton exchange membrane (PEM) fuel cell—which are easily poisoned by impurities.[48] Light-metal amides are the most promising alternative to ruthenium-based catalysts for cracking, the first example, sodium amide ($NaNH_2$),

shown by David *et al.*, exhibited similar performance to supported ruthenium catalysts. Importantly, this new class of materials are significantly less expensive than conventional precious metal catalysts.[42] Sodium amide cracks ammonia through its decomposition to sodium metal and subsequent re-formation of the amide, via the following mechanisms:

$$\mathrm{NaNH_2(s)} \longrightarrow \mathrm{Na\,(s)} + \frac{1}{2}\,\mathrm{N_2(g)} + \mathrm{H_2(g)} \tag{1.8}$$

$$\mathrm{Na\,(s)} + \mathrm{NH_3(g)} \longrightarrow \mathrm{NaNH_2(s)} + \frac{1}{2}\,\mathrm{H_2(g)} \tag{1.9}$$

Lithium amide ($LiNH_2$) was subsequently investigated and its thermal decomposition differs to the sodium amide (eq. 1.8) because it decomposes into lithium imide (Li_2NH) rather than lithium metal:

$$2\,\mathrm{LiNH_2(s)} \rightleftharpoons \mathrm{Li_2NH\,(s)} + \mathrm{NH_3(g)} \tag{1.10}$$

Given that ammonia is a decomposition product, lithium amide was not originally anticipated to be an effective ammonia decomposition catalyst. The lithium imide-amide system was however shown to outperform both sodium amide and alumina-supported ruthenium under moderate conditions (450 °C under 60 sccm ammonia), converting 90.7 % of ammonia compared to 54.9 % and 53.7 % respectively.[49] This ammonia-decomposition activity is related to the non-stoichiometry in the lithium imide-amide system. The catalyst is, in fact, closer in stoichiometry to lithium imide than lithium amide. Understanding Li^+ motion within this system is therefore important for its activity.[49] Catalytic decomposition based on light-metal amides is very different to traditional supported transition metal catalysts.[44, 50, 51, 52] The interactions of ammonia on the surface and in the bulk of these materials will also be very different, and invite atomic scale computational modelling.

The lithium imide structure has received significant attention because of its role within the amide-imide system for hydrogen storage.[25, 32, 34, 53] Computational studies have been used in an attempt to understand the mechanism for reversible hydrogen storage. However, despite substantial research efforts, the low-temperature structure of lithium imide has not

been fully resolved.[54, 55, 56, 57] The lithium imide structure is important for ammonia-decompostion catalysis, as it is the basis for understanding the surface and subsequently the cracking of ammonia.

In addition to the development of effective ammonia decomposition catalysts, sustainable ammonia production is critical for ammonia to be used as a realistic energy carrier. The traditional Haber-Bosch process emits between 1.8–2.1 ton of CO_2 per ton of NH_3 produced.[58] This is due to the fossil fuel used to manufacture the hydrogen feedstock (discussed previously) and the harsh reaction conditions of ∼200 bar and 400–450 °C to overcome the reaction kinetics.

$$N_2 + 3\,H_2 \overset{Fe}{\rightleftharpoons} 2\,NH_3 \qquad \Delta_r H^{\ominus} = -92\,\mathrm{kJ\,mol^{-1}} \tag{1.11}$$

Efficient nitrogen fixation is inherently a difficult problem to solve due to the high bond dissociation energy of the N_2 triple bond ($941\,\mathrm{kJ\,mol^{-1}}$) that results in very poor reaction kinetics. Green ammonia has been based on production from N_2 and H_2O:

$$N_2 + 3\,H_2O \longrightarrow 2\,NH_3 + \frac{3}{2}\,O_2 \qquad \Delta_r H^{\ominus} = 766\,\mathrm{kJ\,mol^{-1}} \tag{1.12}$$

There are two main types of catalyst that have been developed for this N_2 reduction, photocatalysis[59] [60] and electrocatalysis.[61] [62] However, they are far from practical application. Efforts to improve these catalysts and develop new approaches to synthesis under milder conditions may help facilitate small scale ammonia-production, including being directly coupled to renewables. Most recently, Chen *et al.* observed ammonia-production from combinations of group I/II metal hydrides and imides (general formulas MH and MNH) with transition metals; this is a significant departure from other catalysts under development.[63] Ammonia production was reported to occur via a two-step mechanism: firstly, N_2 is activated by the transition metal and then reduced by the hydride in MH forming MNH and second, MNH is hydrogenated forming MH + NH_3. LiH and BaH_2 were reported as the most thermodynamically favourable, and consequently their nitriding was

investigated with the addition of 3d transition metal catalysts (Fe, Co, Ni)—achieving operating temperatures below 300 °C at 1 bar. This work represents an entirely new class of ammonia-production catalysts based on metal hydrides and imides with 3d transition metals. As such, the mechanisms within these materials for both N_2 splitting and NH_3 synthesis from imide to ammonia are unknown.

1.5 High-performance computing

In this thesis, the majority of computation was performed on the SCARF cluster in the STFC Scientific Computing Department; its original antecedent was the Harwell Dekatron Computer in the 1950s. Although the calculations today are much more complex, the scientific practice of running calculations continuously, and often at obscure hours or times of the year hasn't changed:

> "[The Harwell Dekatron Computer] could be left unattended for long periods; I think the record was over one Christmas-New Year holiday when it was all by itself, with miles of input data on punched tape to keep it happy for at least ten days, and was still ticking away when we came back."
>
> **J. Howlett, Computational Scientist on the Harwell Dekatron Computer**[64]

1.5.1 *In silico* meaning

In silico is faux Latin for "in silicon". The phrase describes all research performed by computer simulation, as silicon refers to the semiconducting material that computer processors are fabricated from.

1.5.2 High-performance computers

The computer simulations in this thesis were all performed on high-performance computers due to the size and complexity of the models used. A high-performance computer, otherwise known as a supercomputer, is a machine with a very large computational capacity compared to that of a general-purpose computer. The performance is on a scale

of $10^{15} - 10^{17}$ floating-point operations per second (arithmetic performed on floating-point numbers) compared to $\sim 10^{9} - 10^{11}$ on a general-purpose machine.[65]. High-performance is a continually moving target as the supercomputers of today become the general-purpose computer of tomorrow. At the time of writing, Summit at Oak Ridge National Laboratory is the world's fastest computer—capable of computing 1.435×10^{17} floating-point operations per second![65]

Supercomputers, except in scale, resemble any modern computing system as they are all parallel computers. This paradigm involves breaking down a computational problem into discrete parts and distributing the workload across multiple processors in order to simultaneously solve the problem. General-purpose computers have used parallel computation for over a decade. Since the thermal limit of single-core processors was reached, future performance gains have come from multi-core processors—with many cores individually running at slower speeds. High-performance computers contain thousands of multi-core processors which are not highly specialised and are essentially the same as those found in personal computers. A supercomputer is comparable to having thousands of general-purpose computers solving a problem in tandem. The speedup in computation does not scale linearly with the number of processors added and this is mostly because the cost of communication between the processors increases with the processor count (interconnect cost), akin to trying to make sense of a three-way conversation compared to a hundred-way one.

1.5.3 Data mining, programming and open-source software

This thesis opens with a quote by Eric S. Raymond, a software developer renowned in hacker culture[†] for his musings on open-source software and whose software is used everyday by anyone with a smart phone. This opening quote gives an indication of the importance of programming to the research presented, as the output files of the calculations have required extensive data mining, analysis and visualisation—which has amounted to thousands of lines of code. The code developed was predominantly written in Python version 2.7;[66] a programming language selected for its convenience, as a high-level inter-

[†]not the same as malicious hackers

preted language with a comprehensive library of scientific packages.[67, 68, 69, 70, 71, 72, 73] The Bourne-Again SHell command language was also used extensively for the automation of tasks on high-performance computers. All software used in this thesis, including the operating systems is, without exception, open-source.

1.6 Classification of crystal structures by symmetry

Crystalline materials are three-dimensional ordered arrays of repeating atoms or groups of atoms. The smallest repeating unit which represents the full symmetry of the crystal is known as the unit cell and crystals are classified into seven classes that are defined by the relationship between the axial system of their unit cell—from the axial lengths (a, b and c) and interaxial angles (α (between b,c), β (a,c) and γ (a,b)). Lattice points are positions in the unit cell where the structure is repeated by translation, and in the most basic arrangement these points are located at all corners of the unit cell, known as a primitive (or simple) lattice. The seven crystal classes are expanded into fourteen Bravais lattices from the addition of lattice points within the cell (and therefore translational symmetry), and the lattice types are named from the centring of these additional points. Table 1.1 summarises the crystal classes and their Bravais lattices. The crystal structure is assigned to a crystallographic point group, a set of symmetry operations (inversions, rotations and reflections) that when applied to the centre of the unit cell leaves the positions of the atoms unchanged. The Bravais lattices combined with the crystallographic point groups and translational symmetry elements (screw axes and glide planes) lead to 230 unique space groups, that collectively describe all particle arrangements in crystalline solids.

Table 1.1: The seven crystal classes and their fourteen Bravais lattices.

Crystal class	Bravais lattices (lattice centring)	Axial lengths (a, b and c)	Interaxial angles (α, β and γ)
Cubic	primitive body-centred face-centred	$a = b = c$	$\alpha = \beta = \gamma = 90^\circ$
Tetragonal	primitive body-centred	$a = b \neq c$	$\alpha = \beta = \gamma = 90^\circ$
Hexagonal	primitive	$a = b \neq c$	$\alpha = \beta = 90^\circ$, $\gamma = 120^\circ$
Rhombohedral	primitive	$a = b = c$	$\alpha = \beta = \gamma \neq 90^\circ$
Orthorhombic	primitive body-centred face-centred base-centred	$a \neq b \neq c$	$\alpha = \beta = \gamma = 90^\circ$
Monoclinic	primitive base-centred	$a \neq b \neq c$	$\alpha = \beta = 90^\circ$, $\gamma \neq 90^\circ$
Triclinic	primitive	$a \neq b \neq c$	$\alpha \neq \beta \neq \gamma$

1.7 Thesis Outline

The aim of this thesis is to develop an atomic-scale understanding of Li–N–H systems for energy storage applications. Chapter 2 consists of an overview of the computational methods that were used. In Chapter 3, a surface model of lithium hydride was first constructed and a short comparison was made with other alkali-metal hydride surfaces. The interactions of ammonia on the lithium hydride surface were then investigated, and this work was extended to molecules on the surface that are similar structurally to ammonia. Amide and imide groups were embedded in the lithium hydride bulk and surface structures to determine the preferred N—H orientational distributions. In Chapter 4, a detailed analysis of the lithium imide structure was performed between 300–700 K and

lithium defect formation was traced throughout the structure. In Chapter 5, conclusions and suggestions for further work resulting from this thesis are presented.

2

Computational Methods

2.1 What are Computer Models and Simulations?

A computer model is an artificial representation of a real world system. The theory in this chapter was used to build a model, and by definition any model is an approximation, a cartoon of reality. A computer simulation is the physical process of running a computer model, and although these terms are very different they are frequently used interchangeably.

2.2 Density Functional Theory

This chapter briefly discusses the fundamental concepts of Density Functional Theory (DFT), a practical method of approximating the many-body Schrödinger equation that

is widely used in materials modelling. It functions as a brief overview and more complete descriptions can be found in textbooks by Giustino and Sholl and Steckel.[74, 75]. To understand why approximations are made, the difficulties in solving the many-body Schrödinger equation must first be explored.

The Schrödinger equation describes all information about a quantum system and the wavefunction $\psi(\mathbf{r},t)$ is the central quantity. $\psi(\mathbf{r},t)$ describes the position ($\mathbf{r}$) and time (t) of a particle, with $|\psi(\mathbf{r},t)|^2$ the probability of locating a particle at time t. The time-dependent Schrödinger equation is given by:

$$\left[-\frac{\hbar^2}{2m}\bigtriangledown^2 + V(\mathbf{r},t)\right]\psi(\mathbf{r},t) = i\hbar\frac{\partial}{\partial t}\psi(\mathbf{r},t) \tag{2.1}$$

with the left side of the equation equal to the kinetic and potential energy, and the right side the time evolution of the wavefunction. The problem with eq. 2.1 is that it is impossible to solve for anything other than a one-particle system. Dirac commented that:

> "The underlying physical laws necessary for the mathematical theory of a large part of physics and the whole of chemistry are thus completely known, and the difficulty is only that the exact application of these laws leads to equations much too complicated to be soluble." **Dirac, 1929**[76]

The time-independent Schrödinger equation is a simplification originating from the fact that many useful properties of a system (such as energy) do not have a time dependence, and therefore it is not always necessary to solve for t. The energy during a chemical reaction is time dependent; however, the time-independent Schrödinger equation can be used to calculate the energies of a reaction as a series of fixed points along a time evolving trajectory. The equation is as follows:

$$\hat{H}\psi(\mathbf{r}_i,\mathbf{R}_j) = E\psi(\mathbf{r}_i,\mathbf{R}_j) \tag{2.2}$$

where $\hat{H}$ is the Hamiltonian operator, ψ the wavefunction, $\mathbf{r}_i$ the electron positions and $\mathbf{R}_j$ the nuclear positions. The first assumption made to the Schrödinger equation is the

Born-Oppenheimer approximation, that the nuclear and electronic motion can separated due to the difference in mass of the particles, with an electron $\sim 1/1840$ the mass of a proton. The nuclear motion is so slow in comparison to the electrons that the nuclei can be viewed as being effectively stationary. This leads to the decoupling of the wavefunction into:

$$\psi = \psi_{\text{elec}}(\mathbf{r}_i, \mathbf{R}_j)\psi_{\text{nuc}}(\mathbf{R}_j) \tag{2.3}$$

The Hamiltonian is also simplified by the Born-Oppenheimer approximation, as the nuclear terms are constant parameters (i.e. nuclei-nuclei interactions) and the nuclear kinetic energy is zero, expressed in atomic units as:

$$\hat{H} = -\frac{1}{2}\sum_i \nabla_i^2 - \sum_{i,j}\frac{Z_j}{|\mathbf{r}_i - \mathbf{R}_j|} + \frac{1}{2}\sum_{i\neq j} + \frac{1}{|\mathbf{r}_i - \mathbf{r}_j|} + \frac{1}{2}\sum_{i\neq j}\frac{Z_i Z_j}{|\mathbf{R}_i - \mathbf{R}_j|} \tag{2.4}$$

from left-to-right are terms for kinetic energy (T), nuclei-electron interaction energy (V_{ne}), electron-electron interaction energy (V_{ee}) and nuclei-nuclei repulsion (V_{nn}). This simplification is not sufficient as the time-independent Schödinger equation is intractable for many-body systems because the electronic wavefunction needed to satisfy the equation has $3N_e$-dimensions, where N_e is the number of electrons. The solution is Density Functional Theory.

2.2.1 The Hohenberg-Kohn theorems

The two Hohenberg-Kohn theorems are the basis of modern Density Functional Theory and establish that eq. 2.2 can be reformulated in terms of electron density, $n(\mathbf{r})$—thus avoiding the calculation of the all-electron wavefunction. The wavefunction is replaced by electron density as the central quantity.[77]

Theorem I states that the electron density of the ground-state (n_0) uniquely determines the external potential (V_{ext}). It describes N_e electrons moving in a static potential from the nuclear attraction energy in the electronic Hamiltonian.

The theorem is based on an existence proof, that two different external potentials cannot be obtained from the same ground-state electron density. To demonstrate this a case is considered where two different external potentials $V_{ext}^{(1)} \neq V_{ext}^{(2)}$ have the same ground-state electron density. The different external potentials will have unique Hamiltonians ($\hat{H}^{(1)}$ and $\hat{H}^{(2)}$) with corresponding wavefunctions ($\psi^{(1)}$ and $\psi^{(2)}$). The total energy of the ground-state wavefunction $\psi^{(1)}$ can be written in the convenient format:

$$\langle\psi^{(1)}|\hat{H}^{(1)}|\psi^{(1)}\rangle = E^{(1)} \tag{2.5}$$

As $\psi^{(1)}$ is not the ground-state wavefunction of $V_{ext}^{(2)}$, an inequality can be written by substituting $\psi^{(1)}$ into eq. 2.5 but for $E^{(2)}$:

$$\langle\psi^{(1)}|\hat{H}^{(2)}|\psi^{(1)}\rangle > E^{(2)} \tag{2.6}$$

The total energy can be separated into the sum of the external potential, kinetic energy ($\hat{T}$) and Coulomb repulsion ($\hat{W}$), eq. 2.5 and 2.6 are rewritten as:

$$\int d\mathbf{r}\, n_0(\mathbf{r}) V_{ext}^{(1)}(\mathbf{r}) + \langle\psi^{(1)}|\hat{T} + \hat{W}|\psi^{(1)}\rangle = E^{(1)} \tag{2.7}$$

$$\int d\mathbf{r}\, n_0(\mathbf{r}) V_{ext}^{(2)}(\mathbf{r}) + \langle\psi^{(1)}|\hat{T} + \hat{W}|\psi^{(1)}\rangle > E^{(2)} \tag{2.8}$$

Substituting eq. 2.7 and 2.8 to obtain:

$$E^{(1)} - E^{(2)} > \int d\mathbf{r}\, n_0(\mathbf{r})[V_{ext}^{(1)}(\mathbf{r}) - V_{ext}^{(2)}(\mathbf{r})] \tag{2.9}$$

Repeating the previous steps from eq. 2.6 but for $\psi^{(2)}$:

$$E^{(2)} - E^{(1)} > \int d\mathbf{r}\, n_0(\mathbf{r})[V_{ext}^{(2)}(\mathbf{r}) - V_{ext}^{(1)}(\mathbf{r})] \tag{2.10}$$

Summing eq. 2.9 and 2.10 results in the contradiction that $0 > 0$:

$$E^{(1)} - E^{(1)} > E^{(2)} - E^{(2)} \tag{2.11}$$

This completes the first theorem, demonstrating that the same ground-state electron density (n_0) cannot be obtained from two different external potentials, and therefore that n_0 is unique to the external potential. For any N_e electron system the kinetic energy (T) and electron-electron interaction (V_{ee}) contributions to the electronic Hamiltonian (eq. 2.4) are the same. V_{ne} depends on the chemical environment and therefore the external potential V_{ext}. For a given N_e electron system, it is V_{ext} that uniquely determines the Hamiltonian, and thus the ground-state wavefunction and total energy. The theorem demonstrates that n_0 uniquely determines V_{ext}, and therefore by extension all ground-state properties of a system.

Theorem II states that a universal functional ($F_{HK}[n]$) exists for the electronic energy defined in terms of electron density (so independent of the external potential). This results from the reformation of the Schödinger equation with electron density as the central quantity:

$$E_{el}[n] = F_{HK}[n] + \int V_{ext}(\mathbf{r})n(\mathbf{r})\,d\mathbf{r} \tag{2.12}$$

There is however no explicit formula known for the universal function, only that it exists. The true ground-state electron density is the global minimum value of the functional $F_{HK}[n]$.

2.2.2 The Kohn–Sham ansatz

The Hohenberg-Kohn theorems establish that electron density can be used to describe all the ground-state properties of a system. However, the theorems are not instructive as to how to locate the ground-state and the universal functional is unknown. The solution is the Kohn-Sham ansatz (approach).[78] Kohn and Sham recast the many-body problem into a non-interacting particle problem. The electron density is considered to be a fictitious system of non-interacting electrons whose density is identical to the interacting system. This means that the total energy can be separated into an easily accessible contribution, the non-interacting system, and a less accessible contribution, the electron interactions. It is an efficient solution because the non-interacting system contributes the majority of

the total energy, and contributions from the electron interactions are collected in a single functional—while the exact form of the functional remains unknown.

The energy of the non-interacting system is represented by the sum of individual one-electron wavefunctions, obtained from a series of one-electron Schrödinger equations:

$$\hat{H}_{KS}\psi_i = \left[-\frac{1}{2}\bigtriangledown^2 + V_{KS}\right]\psi_i = \epsilon_i\psi_i \tag{2.13}$$

where V_{KS} is the Kohn-Sham potential that the non-interacting system is moving in, and ψ_i are one-electron orbitals (Kohn-Sham orbitals). The individual orbitals can be expressed as functionals of the electron density and the electron density of the non-interacting system is obtained from the sum:

$$n(\mathbf{r}) = \sum_{i=1}^{N_e} |\psi_i(\mathbf{r})|^2 \tag{2.14}$$

The Kohn-Sham potential is given by:

$$V_{KS}(\mathbf{r}) = \int d\mathbf{r}' \frac{n(\mathbf{r}')}{|\mathbf{r} - \mathbf{r}'|} + V_{xc}(\mathbf{r}) + V_{ext}(\mathbf{r}) \tag{2.15}$$

where V_{xc} is the exchange-correlation potential and V_{ext} the external static potential. $V_{KS}(\mathbf{r})$ depends on the electron density. This means that the non-interacting system has to be solved self-consistently, i.e. an initial estimate must be made for the electron density and the ground-state electron density is sought by iterative minimisation of the Kohn-Sham energy, until the density input and output are the same. This is known as the Self-Consistent Field (SCF) method and is performed at the beginning of all DFT calculations. A schematic of the process is given below:

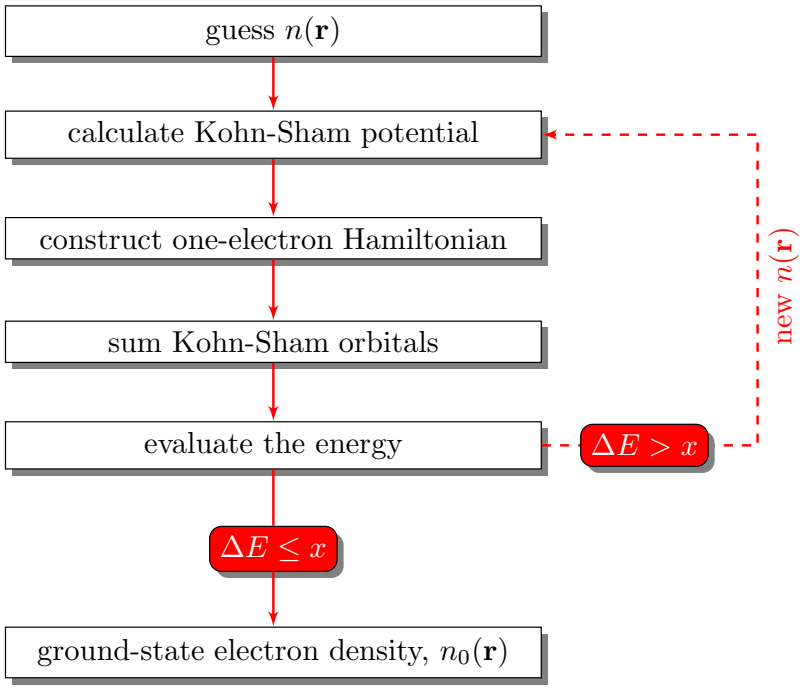

Figure 2.1: Self-Consistent Field method to obtain the ground-state electron density from the Kohn-Sham equations (eqs. 2.13–2.15). ΔE is the energy difference between cycles and x is an energy convergence criteria.

The total energy of the system is expressed as functionals of the electron density and separated into terms for the non-interacting and interacting system, given by:

$$E[n(\mathbf{r})] = T_{KS}[n(\mathbf{r})] + \int d(\mathbf{r}) V_{ext}(\mathbf{r}) + \frac{1}{2} \int d\mathbf{r}\, d\mathbf{r}' \frac{n(\mathbf{r}) n(\mathbf{r}')}{|\mathbf{r} - \mathbf{r}'|} + E_{xc}[n(\mathbf{r})] \tag{2.16}$$

where the four terms are, the kinetic energy for the non-interacting system, the interaction energy with the external potential, the classical electrostatic energy and the exchange-correlation energy. $T_{KS}[n(\mathbf{r})]$ is an approximation of the kinetic energy because electron-electron correlation is not handled in the non-interacting system. The interaction energy with the external potential (electron-nuclei) and classical electrostatic energy are simple Coulombic interactions that are readily solved. The exchange-correlation energy contains all the corrections to the system of non-interacting electrons due to the electron interactions; the explicit formula for E_{xc} is unknown. The Kohn-Sham ansatz is an ef-

ficient method of calculating the ground-state energy of a system because most of the total energy (more than 90%) is calculated exactly from the non-interacting system. It is, however, the remaining 10% that is most interesting. Kohn's substantial contribution to the field of computational quantum mechanics, from both the Hohenberg-Kohn theorems and Kohn-Sham ansatz, was recognised by the award of the Nobel Prize in Chemistry in 1998.

2.2.3 Exchange-correlation functionals

$$E_{xc}[n(\mathbf{r})] = (T[n(\mathbf{r})] - T_{KS}[n(\mathbf{r})]) \; + \; (E_{ee}[n(\mathbf{r})] - E_J[n(\mathbf{r})]) \tag{2.17}$$

The exchange-correlation functional handles all of the many-body interactions arising from the Kohn-Sham ansatz, i.e. the less accessible contributions to the total energy. In eq. 2.17, $T[n(\mathbf{r})]$ is the kinetic energy and $E_{ee}[n]$ the electron-electron interactions, $T_{KS}[n(\mathbf{r})]$ and $E_J[n(\mathbf{r})]$ are the respective corrections from using a non-interacting system. If this functional was known, the exact ground-state energy could be calculated for any many-body problem. However, it is likely that the solution will be far too complicated to be computationally useful—though quantum computing may address this complexity. For the present, approximations must be made to the exchange-correlation functional.

The pursuit of the exchange-correlation functional is the last piece in Hohenberg and Kohn's universal functional. Its significance has led physicists to aptly compare it to the biblical narrative of Jacob's ladder: a mythical ladder which connected Earth to Heaven (Figure 2.2).[79] With the universal functional at the top, each rung represents a better description of exchange-correlation, and therefore a step closer to solving the exact ground-state of the many-body problem. However, in reality, improvements in accuracy have come at the cost of increased specificity, with exchange-correlation functionals becoming highly parameterized and therefore having fewer use cases—a far from universal solution!

Figure 2.2: Ascending Jacob's ladder (Genesis 28:10–19).[80]

The simplest exchange-correlation functional is the Local Density Approximation (LDA) which models the energy from a homogeneous electron gas with the same electron density. The exchange-correlation energy of a homogenous electron gas depends only on its electron density (n(**r**)) and is accurately computed from Quantum Monte Carlo methods.[81] This simple approximation produces good results and is especially effective for systems with no large variations in electron densities. It is, however, well-known to overbind atoms. The generalized gradient approximation (GGA) is an improvement upon LDA that includes the gradient of the electron density in addition to its value at a given point:[82]

$$V_{XC}(\mathbf{r}) = f(\mathbf{r}, n(\mathbf{r}), \bigtriangledown n(\mathbf{r})) \tag{2.18}$$

This improves the accuracy and can be used to study molecular systems. There are many GGA functionals and the **P**erdew-**B**urke-**E**rnzerhof (PBE) functional is one of most popular. It was chosen for the simulations in this thesis because it is known to work well for studies of molecules on surfaces.[83, 84]

2.2.4 Bloch's theorem: periodic boundary conditions

In crystalline solids, atoms are periodic, and therefore can be arranged in regular, repeating patterns. Bloch's theorem makes use of this regular arrangement to simplify the

wavefunction, as only the electrons within one repeating periodic unit are considered, rather than a system with an infinite number of electrons. As the nuclei are periodic so is the nuclei potential that acts on the electrons, such that $V(\mathbf{r}) = V(\mathbf{r} + \mathbf{L})$ where $\mathbf{L}$ is a lattice vector. The electron density must therefore also be periodic, $n(\mathbf{r}) = n(\mathbf{r} + \mathbf{L})$. The wavefunction in Bloch's theorem is given by:

$$\psi_{\mathbf{k}}(\mathbf{r}) = u_{\mathbf{k}}(\mathbf{r})\, e^{i\mathbf{k}.\mathbf{r}} \tag{2.19}$$

This separates the wavefunction into the product of a periodic cell part ($u_{\mathbf{k}}(\mathbf{r}) = u_{\mathbf{k}}(\mathbf{r}+\mathbf{L})$ and wavelike part ($e^{i\mathbf{k}.\mathbf{r}}$). The cell part can be expanded in terms of a discrete plane waves basis set whose wave vectors are the reciprocal lattice vectors ($\mathbf{G}$) of the crystal (written as the sum of the plane waves). The reciprocal lattice vectors are the components of the Fourier sum which reproduce the perodicity of the crystal structure.

There are an infinite number of electrons in a periodic crystal which, in turn, requires an infinite number of $\mathbf{k}$-points for their description. This issue is reduced in the periodic cell to a finite number of electrons but with an infinite number of $\mathbf{k}$-points. However, when $\mathbf{k}$-points are sufficiently close together the wavefunctions are for all practical purposes identical, and therefore a discrete grid of $\mathbf{k}$-points can be used to approximate this space. Bloch's theorem also works for aperiodic systems (such as surfaces) provided that superficial periodicity is imposed to the system through the use of a supercell and that self-interactions are addressed.

2.2.5 Basis sets

In Bloch's theorem, the expansion of the wavefunction in terms of a discrete plane waves basis set is an approximation to an infinite basis set. The plane waves do not equally contribute to the wavefunction, as those with smaller kinetic energies (small $\mathbf{G}$) describe lower frequency components of the wavefunction, and these more greatly contribute to the construction of molecular orbitals than high frequency oscillations. This allows a cut-off energy to be used to truncate the plane wave basis set—this is determined from convergence testing. Bloch's theorem works for basis sets other than just plane waves, and as such, the

VandeVondele *et al.* mixed atom-centred Gaussian functions and plane waves approach was used for efficient molecular dynamics simulations.[85]

2.2.6 The Pseudopotential Approximation

Even with Bloch's theorem and a truncated basis set, the wavefunction is still expensive to calculate. It is well-known that electrons do not equally contribute to the chemical properties of a system and this is used to approximate the potential. The electrons closest to the nuclei do not significantly effect the chemical interactions of a system because they are tightly bound to the nucleus due to experiencing the largest Coulombic attraction. This core region is also more expensive to model, as the potential which describes the electrons has a higher frequency (due to the Coulombic attraction). Pseudopotentials reduce the number of plane waves needed to construct the wavefunction by not accurately modelling the core region, instead they simply reproduce the screening effect of the core-electrons to the nucleus, and thus a smaller cut-off energy is required for convergence. Ultrasoft pseudopotentials which relax the norm-conservation rule in order to use softer (smoother) pseudo wavefunctions to represent the core region were selected for the CASTEP calculations.[86]

2.2.7 Geometry optimisation

Geometry optimisation is the procedure to locate the lowest energy configuration of atoms in an system, which is generally the structure that is found in nature. The energy of the system is minimised by changing the spatial positions of atoms until the forces acting on them are zero. The forces in density functional theory are calculated from the gradient of the total energy functional, given by:

$$\mathbf{F}_i = -\frac{\partial E[n_0]}{\partial \mathbf{r}_i} \tag{2.20}$$

The energies for all the possible spatial arrangements of atoms in a system can be constructed into a multidimensional energy landscape. A minimisation algorithm is required to efficiently explore this landscape to minimise the energy with respect to the spatial

arrangement. Sampling the entirety of configuration space is incomputable and therefore the lowest energy configuration found will always be a local minimum—the initial atomic coordinates determine the point on the energy landscape from where the minimum is sought.

The simplest approach is the steepest descents algorithm. This method finds the minimum energy along a search direction and uses the gradient at that point as the direction of the next search. It is inefficient because the new search direction only uses information from one previous step, and therefore can undo prior minimisations. The minimisation pathway "zig-zags" across the energy landscape due to the orthogonal search directions, and in addition to being an non-optimal route, is slow to converge because a higher number of iterations are required closer to the minima (where the gradient is smaller). The conjugate gradients method improves on the steepest descents algorithm by seeking new directions that are orthogonal to all previous search directions, and therefore successive search directions cannot undo prior minimisation. There are different implementations of the conjugate gradients method; one of the most popular for geometry optimisations in materials modelling is the BFGS (Broyden-Fletcher-Goldfarb-Shanno) algorithm which constructs a Hessian matrix to store all of the search directions.[87]

2.3 Molecular dynamics

The motion of particles were simulated by *ab initio* molecular dynamics in this thesis. The physical movements of the atoms are described classically by Newton's second law of motion and interatomic forces are calculated from first principles using density functional theory. Statistical mechanics is used to connect the microscopic systems being investigated, a model containing a few hundred atoms, to macroscopic properties through the analysis of ensembles of individual computational steps.

2.3.1 The ensemble concept

A statistical ensemble is a collection of distinct microscopic states that together share the same macroscopic properties. Each microscopic state is a complete set of atomic positions ($\mathbf{r}$) and momenta ($\mathbf{p}$) of the system at one point in time. All of the possible microscopic states that can be occupied are known collectively as the phase space ($\mathbf{\Gamma}$). The macroscopic observables are calculated from the ensemble averages of the microscopic states, and therefore the precise details of any one microscopic state does not effect the overall macroscopic properties. Many macroscopic properties are time-independent, such as temperature and pressure, and this allows an ensemble average to be calculated for any given instant in time.

The canonical and isothermal-isobaric ensembles (Figure 2.3) were used in this thesis to model atomic systems with different macroscopic constraints. The canonical ensemble (shorthand N,V,T) describes a system with a rigid boundary that exists within a heat bath. It contains a fixed number of atoms (N), volume (V) and temperature (T). The rigid boundary permits the exchange of energy as heat but not the exchange of matter with the surroundings. The isothermal-isobaric ensemble (shorthand N,P,T) describes a system with a flexible boundary within a heat bath. The flexible boundary equalises the pressure of the system with the surroundings but cannot exchange matter, and so the system contains a fixed number of atoms (N), pressure (P) and temperature (T).

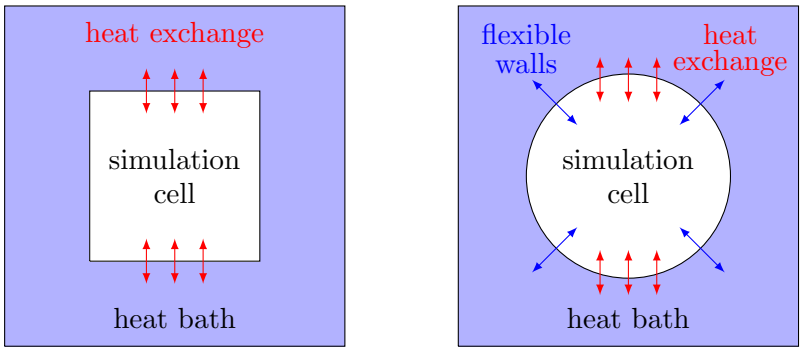

Figure 2.3: Schematic of (a) canonical and (b) isothermal-isobaric ensembles.

2.3.2 Newton's laws of motion

The motion of atoms can be described by classical Newtonian equations of motion integrated with respect to time. Newton's second law of motion for an individual atom is given by:

$$\mathbf{F}_i = m_i \ddot{\mathbf{r}}_i \tag{2.21}$$

where m_i is the mass, $\mathbf{r}_i$ the atomic position and $\mathbf{F}_i$ the force that acts on atom i. As the energy is conserved, the forces are obtained from the gradient of the potential energy surface, via:

$$\mathbf{F}_i = -\frac{\partial V}{\partial \mathbf{r}_i} \tag{2.22}$$

The total energy E is given by the sum of the potential energy (V) and kinetic energy (T):

$$E = V(\mathbf{r}_i) + T(\dot{\mathbf{r}}_i) \tag{2.23}$$

Lagrangian formulation of classical mechanics can be used to solve the Newtonian equations of motion. Central to this formulation is the Lagrangian, defined as the difference between the kinetic and potential energies:

$$L = T(\dot{\mathbf{r}}_i) - V(\mathbf{r}_i) \tag{2.24}$$

with kinetic energy equal to:

$$T(\dot{\mathbf{r}}_1, ..., \dot{\mathbf{r}}_N) = \frac{1}{2} \sum_{i=1}^{N} m_i \dot{\mathbf{r}}_i^2 \tag{2.25}$$

The Euler-Lagrange equation is an expression of the classical equations of motions in terms of the Lagrangian. It provides a framework for solving the equations of motion and is more flexible because it can be used for any set of coordinates:

$$\frac{d}{dt}\left(\frac{\partial L}{\partial \dot{\mathbf{r}}_i}\right) - \frac{\partial L}{\partial \mathbf{r}_i} = 0 \tag{2.26}$$

2.3.3 The velocity-Verlet algorithm

The equations of motion cannot be solved algebraically due to the complexity of the function for the potential energy surface, and therefore must be solved numerically. To solve numerically the equations of motion and thus calculate the trajectory of a system, an integration algorithm is required to discretize time into a series of steps of length Δt. This was performed using the velocity-Verlet algorithm, a variant of the Verlet scheme.

The Verlet integration algorithm is based on a Taylor series expansion of atomic positions about time, with a new position of a particle expressed as:[88]

$$\mathbf{r}_i(t + \Delta t) \simeq \mathbf{r}_i(t) + \Delta t\ \dot{\mathbf{r}}_i(t) + \frac{1}{2}\Delta t^2\ \ddot{\mathbf{r}}_i(t) + ... \tag{2.27}$$

The series is truncated to 2^{nd} order Δt terms and Newton's second law of motion (eq. 2.21) can be substituted into eq. 2.27:

$$\mathbf{r}_i(t + \Delta t) \simeq \mathbf{r}_i(t) + \Delta t\ \mathbf{v}_i(t) + \frac{\Delta t^2}{2m_i}\ \mathbf{F}_i(t) \tag{2.28}$$

The reverse time step is given by:

$$\mathbf{r}_i(t - \Delta t) \simeq \mathbf{r}_i(t) - \Delta t\ \mathbf{v}_i(t) + \frac{\Delta t^2}{2m_i}\ \mathbf{F}_i(t) \tag{2.29}$$

The Verlet algorithm is obtained from the addition of eq. 2.28 and 2.29:

$$\mathbf{r}_i(t + \Delta t) = 2\mathbf{r}_i(t) - \mathbf{r}_i(t - \Delta t) + \frac{\Delta t^2}{m_i}\ \mathbf{F}_i(t) \tag{2.30}$$

A trajectory can be computed using the Verlet algorithm from just the atomic positions and accelerations at time t=0. The Verlet algorithm has two advantages over simple

forward integration, being time-reversible and conserving the total energy of the system. Velocities are not explicitly handled in eq. 2.30 and so must be recovered using a further calculation, such as the Stömer-Verlet equation. To recover the velocity at time t_n requires the atomic positions at the next timestep $t_{(n+1)}$ to have been calculated: the velocity is approximated from the difference in the atomic positions and this has a large associated error.

The velocity-Verlet algorithm is a variant of the Verlet scheme that takes the form:[89]

$$\mathbf{r}_i(t) = \mathbf{r}_i(t + \Delta t) - \Delta t\, \mathbf{v}_i(t + \Delta t) + \frac{\Delta t^2}{2m_i}\, \mathbf{F}_i(t + \Delta t) \tag{2.31}$$

$$\mathbf{v}_i(t + \Delta t) = \mathbf{v}_i(t) + \frac{\Delta t}{2m_i}[\mathbf{F}_i(t) + \mathbf{F}_i(t + \Delta t)] \tag{2.32}$$

The algorithm starts from the forward timestep $(t + \Delta t)$ and computes $\mathbf{r}_i(t)$. Eq. 2.32 is obtained by substituting $\mathbf{r}_i(t + \Delta t)$ in eq. 2.31 for eq. 2.28. The velocity-Verlet algorithm is a more precise method to calculate the trajectory as it simultaneously handles atomic positions, velocities and accelerations.

2.3.4 Simulation of hydrogen by classical molecular dynamics

Hydrogen nuclei are light because they consist of a single proton, and therefore the nuclei can be treated either classically or quantum mechanically. Quantum (Path Integral) Molecular Dynamics accounts for non-Newtonian behaviour of nuclei by the addition of quantum mechanics from Feynmans path integrals.[90] Although this quantum treatment more accurately models hydrogen, the nuclear quantum effects that it accounts for mostly occur at low temperature—due to a larger difference in energy between quantum states. Nuclear quantum effects were unlikely to have been observed from the simulations in this thesis, given the higher temperatures and short picosecond timescales. A Newtonian approximation for hydrogen was therefore deemed most appropriate and this methodology has been used extensively for the computational study of water.[91] Conversely, simpler classical potentials were not used because they do not accurately model hydrogen bonding, being a key bonding interaction in the systems studied.

2.4 Materials modelling codes

The calculations in this thesis were performed using the **CA**mbridge **S**erial **T**otal **E**nergy **P**ackage (CASTEP)[92] and CP2K codes[93]—which implement the methods described in this Chapter.

3

Interactions of ammonia with a lithium hydride surface

3.1 Introduction

The interaction between lithium hydride and ammonia impacts our understanding of the mechanisms for hydrogen storage and ammonia synthesis in the Li–N–H system. In the Li–N–H system for hydrogen storage, LiH + NH_3 is the hydrogen desorption step; the overall mechanism is as follows:

$$2\,\mathrm{LiNH_2} \rightleftharpoons \mathrm{Li_2NH} + \mathrm{NH_3} \tag{3.1}$$

$$\mathrm{LiH} + \mathrm{NH_3} \rightleftharpoons \mathrm{LiNH_2} + \mathrm{H_2} \tag{3.2}$$

Although this phenomenon is a surface interaction, there are no existing surface studies. To date, the formation of lithium amide has been examined computationally by simple $\mathrm{Li}_n\mathrm{H}_n$ (n=1–4) cluster models.[40, 41] In ammonia synthesis, lithium hydride has been reported to produce ammonia via lithium amide-imide formation in the bulk of the material; however, there is little-known about either this interaction or the nature of amide-imide in the bulk structure.[63] Computational modelling could provide important insights into developing an atomic-scale understanding of these underlying mechanisms. The lithium hydride surface is a simple structure that also provides an insight into the interaction of ammonia on other surfaces, particularly the lithium imide-amide decomposition catalyst. The computational approach in this Chapter for the investigation of ammonia on a lithium hydride surface provides the foundations for future investigations of more complicated Li–N–H systems.

The lithium hydride surface is difficult to investigate experimentally because it is air-sensitve and spontaneously forms a hydroxide layer at the surface:

$$\mathrm{LiH} + \frac{1}{2}\,\mathrm{O_2} \xrightarrow{25\,^\circ\mathrm{C}} \mathrm{LiOH} \qquad \Delta G^\ominus = 394\,\mathrm{kJ\,mol^{-1}} \tag{3.3}$$

In silico methods are therefore valuable in providing an atomistic insight into ammonia-surface interactions. Lithium hydride adopts a simple cubic rock-salt structure which can be viewed as two interpenetrating face-centred cubic sublattices of oppositely charged ions. The two sublattices are offset by $(1/2, 1/2, 1/2)$ and therefore each ion is coordinated by six oppositely charged ions in an octahedral arrangement, shown in Figure 3.1.

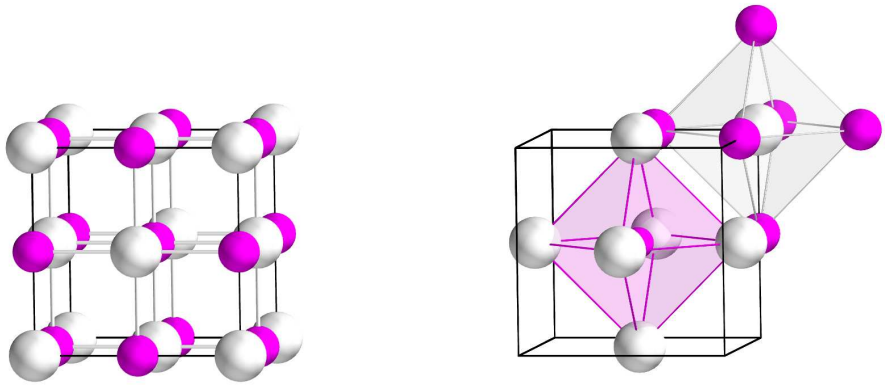

(a) Rock-salt structure

(b) Octahedral coordination environments

Figure 3.1: Rock-salt structure with the octahedral coordination environments highlighted in (b). Lithium is shown in magenta and hydrogen in white.

3.2 (100) surface of lithium hydride

3.2.1 Modelling details

A surface model consists of two regions, an exterior surface that is exposed to the vacuum and an interior bulk shielded from the vacuum. The bulk region of the material is simulated first because it is used to construct a slab of material from which the surface can be reconstructed. The structure of bulk lithium hydride was first solved from X-ray scattering almost a hundred years ago,[94] and therefore the purpose of the simulation was solely to derive an athermal (0 K) lattice constant. CASTEP was used to build the surface model of lithium hydride from Density Functional Theory using the Perdew-Burke-Ernzerhof functional. A single lithium hydride unit cell was used to calculate the athermal lattice constant. The lattice constant at first was taken to be 4.08 Å from literature values that had been collected experimentally at room temperature (sourced from the ICSD).[95] Calculation parameters were determined from a series of single-point energy calculations: the energy converged to better than 2 meV and a stress tolerance of 1×10^{-4} GPa using a $30 \times 30 \times 30$ regular k-point grid and a 900 eV cut-off energy for the ultrasoft pseudopo-

tentials, shown below.[96] These specific tight convergence criteria were selected because they would enable a large range of calculation types to be performed at a high level of accuracy (single-point energy, geometry optimisation, elastic constants calculations etc.) as the scope of the calculations hadn't been decided. The unit cell was geometry optimised with these parameters by the BFGS algorithm as implemented in CASTEP,[87] and as expected, the lattice constant compressed at 0 K, to 4.008 Å.

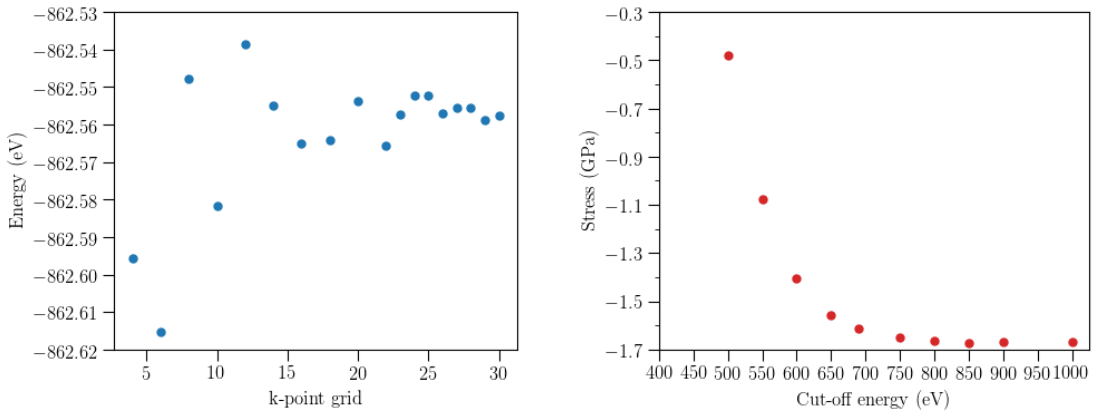

(a) Regular k-point grids.

(b) Cut-off energy for ultrasoft pseudopotentials (elements Li and H).

Figure 3.2: Convergence tests for bulk lithium hydride performed on a single unit cell in CASTEP.

3.2.2 Construction of the surface slab model

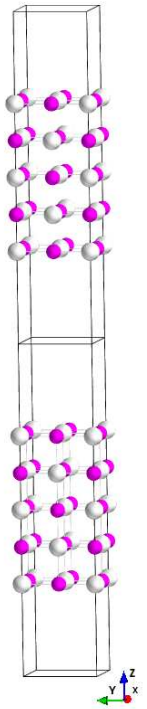

Figure 3.3: Slab model for 3-layers of lithium hydride. The supercell is repeated once in the z-direction.

Once the athermal lattice constant had been attained lithium hydride slab models could be constructed to model the surface. A slab model consists of a slice of material that is placed inside a simulation cell with a vacuum normal to the surface (by convention in the z-direction). This is referred to as a supercell structure. The supercell is periodic in all three-dimensions; however, the surface itself is only periodic in two-dimensions, and therefore while the slice of material is infinite in the x and y-directions, the z-direction contains a vacuum which introduces the possibility of self-interaction between the slabs. Figure 3.3 shows a supercell repeated in the z-direction. The supercell contains two surfaces because the slab is exposed to the vacuum from either side in the z-direction.

An efficient slab model should contain the minimum number of layers (thinnest slab) that reproduces the surface properties of a material, and a comprehensive review of slab creation can be found in Sun and Ceder.[97] Before the creation of a series of slabs to determine the minimum slab thickness, several calculation parameters had first to be determined. The (100) surface of the rock-salt structure is known to have the lowest surface energy using Tasker's classification of ionic crystal surfaces, and therefore it was selected for lithium hydride as the most likely simple surface for ammonia to react on.[98]

The vacuum must be large enough to prevent the slab from interacting erroneously with its periodic image. Convergence tests for vacuum thickness were performed on a $1 \times 1 \times 3$ unit cell slab and this slab thickness was chosen for the tests because it had been previously used to accurately model the (100) surface of rock-salt structured metal oxides:[99] vacuum convergence is shown in Figure 3.4. A vacuum thickness of 12 Å was used for all the slab models as it is more than sufficient to prevent interactions between either sides of the slab. The surface area (xy plane) was selected so that it would sufficiently separate one ammonia on the surface from its periodic image, determined from an evaluation of the change in energy due to self-interaction, and consequently an xy plane of 3×3 unit cells was used. A second set of k-point convergence tests were performed for lithium hydride because of the presence of a vacuum. This test was performed on a 3×3×3 unit cell slab-model with a 12 Å vacuum, one k-point was used in the z-direction to ensure that the vacuum was not being oversampled and a 5×5×1 k-point grid was used for all thicknesses of slab. The original plane wave cut-off energy of 900 eV achieved an extreme level of accuracy that was unnecessary for this type of calculation and therefore a more modest 750 eV cut-off was used in the slab models, which was sufficient to obtain a stress tolerance of 1.86×10^{-2} GPa (from Figure 3.2 (b)).

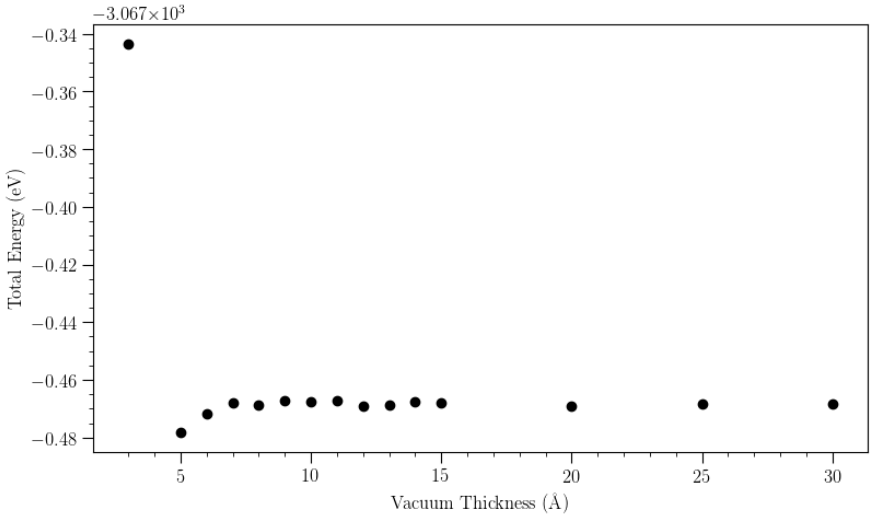

Figure 3.4: Vacuum thickness convergence from the total energy of a clean $1 \times 1 \times 3$ unit cell slab of lithium hydride.

Rumpling in the (100) surface of rock-salt structured ionic crystals is a well known phenomenon where the two ionic species are displaced in opposite directions.[100, 101, 102] The relative positions of the ions in the rumpled surface depends on their size. This surface ion arrangement was recovered by the lithium hydride slab models, with the lithium ions displaced towards the interior of the slab and the hydride ions towards the vacuum. Surface rumpling is explained by simple coordination geometry: in the rock-salt structure each ion is held in an octahedral coordination and surface creation lowers the coordination number of the surface ions such that they rearrange into a square pyramidal structure. Lithium is the central atom in the pyramid and so it moves towards the interior of the slab to sit below the plane of the four neighbouring hydride ions which form the square base.

Slab models were created with between 3 and 19 atom layers separated by 12 Å of vacuum, and the clean slabs were geometry optimised. The slab width was varied to determine the minimum number of layers needed to model the surface, measured by both the recovery of the bulk region and the convergence of the surface arrangements between models. The central layer in each slab was fixed in position to prevent the slabs from drifting (in the z-direction) inside the simulation cells.

The surface relaxations were measured from the vertical displacement between the anions and cations within each layer of the slab (z-direction only), as movement in the x-direction and y-direction were negligible due to the nature of the supercell approach. The bulk region was therefore defined by layers where both ions lie on the same plane, i.e. zero vertical displacement. Slab models were evaluated from their ion displacement per layer in Figure 3.5, where the dashed lines refer to the surface and bulk displacements.

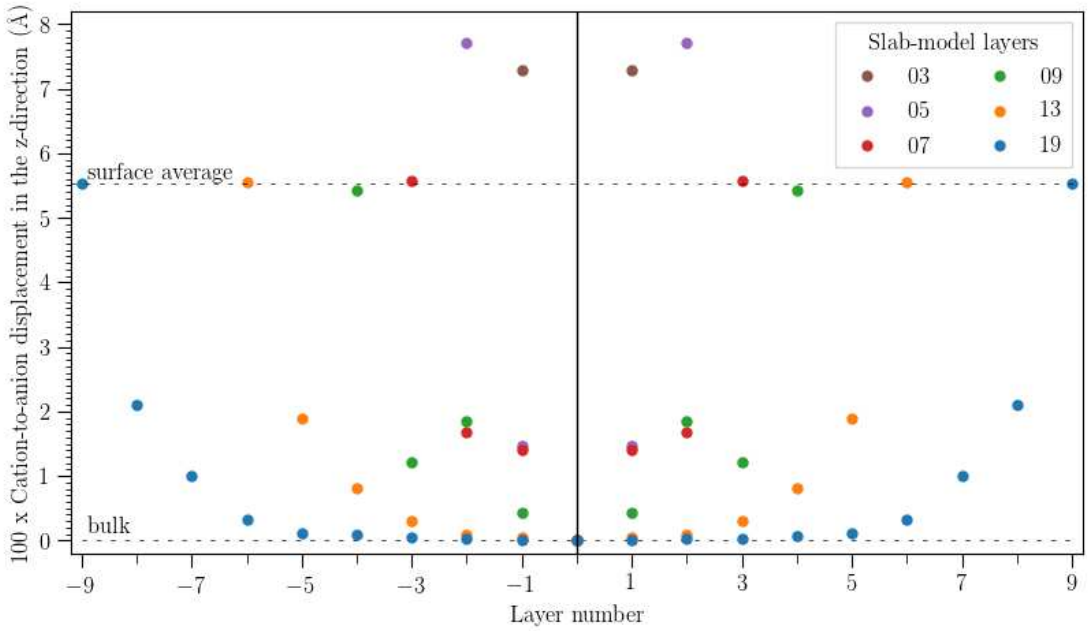

Figure 3.5: Slab thickness convergence from the average ion displacement per layer for a series of slab models. The layer number refers to its z-position within the slab relative to the fixed central layer at zero, and therefore the sign implies the direction. A mirror plane is plotted at x=0 as layer reconstruction either side of the central layer is identical.

The slabs are exposed to the vacuum from both sides in the z-direction which results in the reconstruction of two identical surfaces, and therefore all layers either side of the central layer are mirror image reconstructions. Thus layers of opposite number are identical. As expected, atoms displaced most at the surface and this displacement decreased the farther the layers were from the vacuum in each slab (with the exception of 9 atom layers). Thin slab calculations led to larger surface ion displacements because, without a substantial bulk region anchoring the surface, it could more easily expand into the vacuum. Relatively few layers were required to converge the surface, with the same surface structure achieved by 7 atom layers (0.0557 Å anion-to-cation displacement) as 19 atom layers (0.0552 Å). However, the thinner slab was unable to reproduce the bulk region. Bulk behaviour was not recovered until 13 atom layers in the slab model, and this would have been used as the structural model had it not been able to be simplified further.

It is inefficient to compute two identical surfaces because it is not only the surface but half of the layers in the slab that are symmetrically equivalent. The solution is to impose asymmetry onto the slab through anchoring the positions of the atoms in one of the surfaces, and balancing with a dipole correction—therefore preventing two surfaces from reconstructing.[103] This approximation cannot be assessed without having first determined the surface structure from slab models with unconstrained surfaces, as in Figure 3.5 (hereafter referred to as "symmetric slabs"). The two model types are illustrated below for a fictitious slab of lithium hydride; the surface reconstructions are consistent with the converged slab models. Asymmetric slabs significantly reduce the computational costs because of the smaller number of atoms, shown by (c) having 40% fewer atoms than (b). The vacuum thickness does not change between models and so the supercell is also smaller for the asymmetric slab.

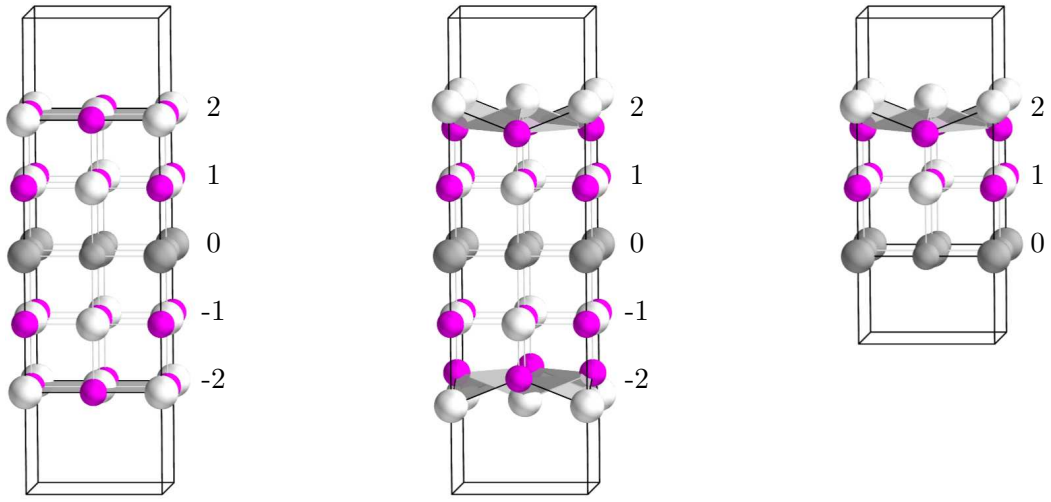

(a) symmetric (unoptimised) (b) symmetric (c) asymmetric

Figure 3.6: Equivalent symmetric and asymmetric slab models for a fictitious $1 \times 1 \times 2$ unit cell symmetric slab of lithium hydride: (a) is the clean symmetric slab, (b) the relaxed symmetric slab and (c) the relaxed asymmetric slab equivalent to (b). Lithium ions are shown in magenta, hydride in white and the greyed out ions are fixed in position. The layer number refers to its z-position within the slab relative to the fixed central layer at zero.

The 13 atom layers in the symmetric slab were reduced to 7 atom layers in the asymmetric slab model. A clean slab of 3×3×3 unit cells (7-layers) with a fixed bottom surface was geometry optimised. At first only the surface layer was fixed; however, this resulted in an unusual rearrangement of the layer above the fixed surface. Even though the surface is fixed, the interior layers still experience the presence of the vacuum from both sides of the slab and this caused the rearrangement. The solution was additionally to fix the penultimate layer as the effect of the vacuum diminishes the further a layer is from the surface. Figure 3.7 compares the 13-layer symmetric slab to the equivalent 7-layer asymmetric slab with 2-layers fixed. The asymmetric model reproduces well the symmetric slab with a 1.39×10^{-3} Å difference in the surface reconstructions. The largest discrepancy between the models was found in layer 2, with a 2.62×10^{-3} Å difference that was due to the layer experiencing the vacuum beneath. This confirms that the 7-layer asymmetric slab with 2-layers fixed is a very good approximation to the symmetric slab models.

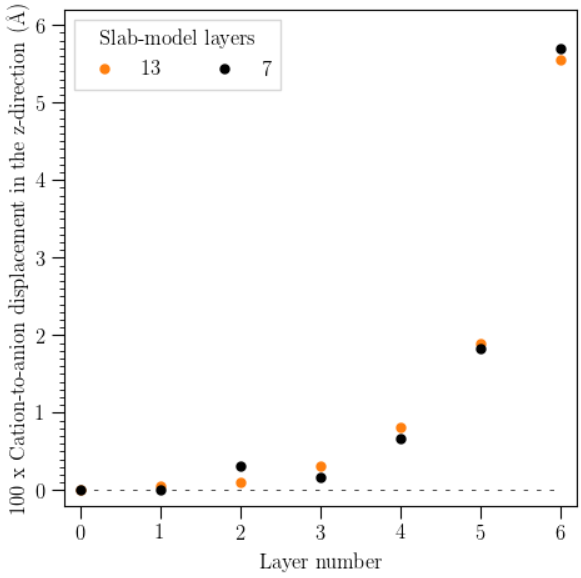

Figure 3.7: Comparison of the 13-layer symmetric slab and 7-layer asymmetric slab with 2-layers fixed from the average ion displacement per layer. Symmetry equivalent layers are not shown for the 13-layer symmetric slab. For these, see Figure 3.5.

The optimised surface structure was analysed by the vertical displacement (z-direction only) of the anions and cations separately in Figure 3.8. Structural changes were mostly localized to the top two layers (layers 5 and 6); the largest rearrangement was the rumpling of the surface, followed by the next layer down that moved upward to compensate for the surface relaxation. The response to the surface reconstruction diminishes the further the layers are from the vacuum, with a decrease in displacement from layers 5 to 3. The larger displacement in layer 2 than layer 3 is a consequence of layer 2 experiencing the vacuum beneath the fixed layers.

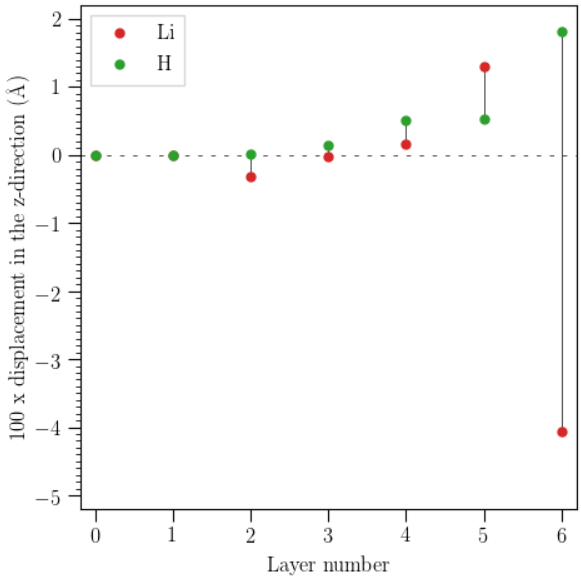

Figure 3.8: Average ion displacement per layer in the asymmetric 7-layer slab with 2-layers fixed, separated into lithium and hydride ions.

Having established a slab model for lithium hydride, the surface reconstruction was quantified as a percentage relaxation from the bulk positions. This was determined using equation 3.4 from Skorodumova *et al.* study of (100) surface rumpling in alkaline-earth metal oxides:[99]

$$\mathrm{d_{rump}}(\%) = \frac{\mathrm{d_{anion}} - \mathrm{d_{cation}}}{\mathrm{d_{bulk}}} \times 100 \tag{3.4}$$

where d_{bulk} is the separation between the bulk layers (i.e. half the lattice constant) and d_{anion} / d_{cation} are the vertical distances from the respective surface ion to the plane of the atoms in the bulk. The hydride displaced toward the vacuum and therefore $d_{anion} > d_{cation}$, so the rumpling in lithium hydride is classified as positive at +2.84%.

3.3 (100) surfaces of non-lithium alkali metal hydrides

(100) surface rumpling was investigated for other rock-salt structured alkali metal hydrides. Sodium, potassium, rubidium and caesium hydride surfaces were reconstructed to determine the effect of ion size on surface rumpling. The 7-layer asymmetric slab used for lithium hydride was also used as the slab model for the other alkali metal hydrides. The calculations were performed with a cut-off energy of 750 eV as the stress on the cells all converged to at least 5.0×10^{-3} GPa and the same $5 \times 5 \times 1$ k-point grid. Convergence tests for the cut-off energies are given in Figure 3.9 (for lithium hydride see Figure 3.2). The lattice constants for the initial slabs of material were obtained from geometry optimizations of the unit cells (as before for LiH).

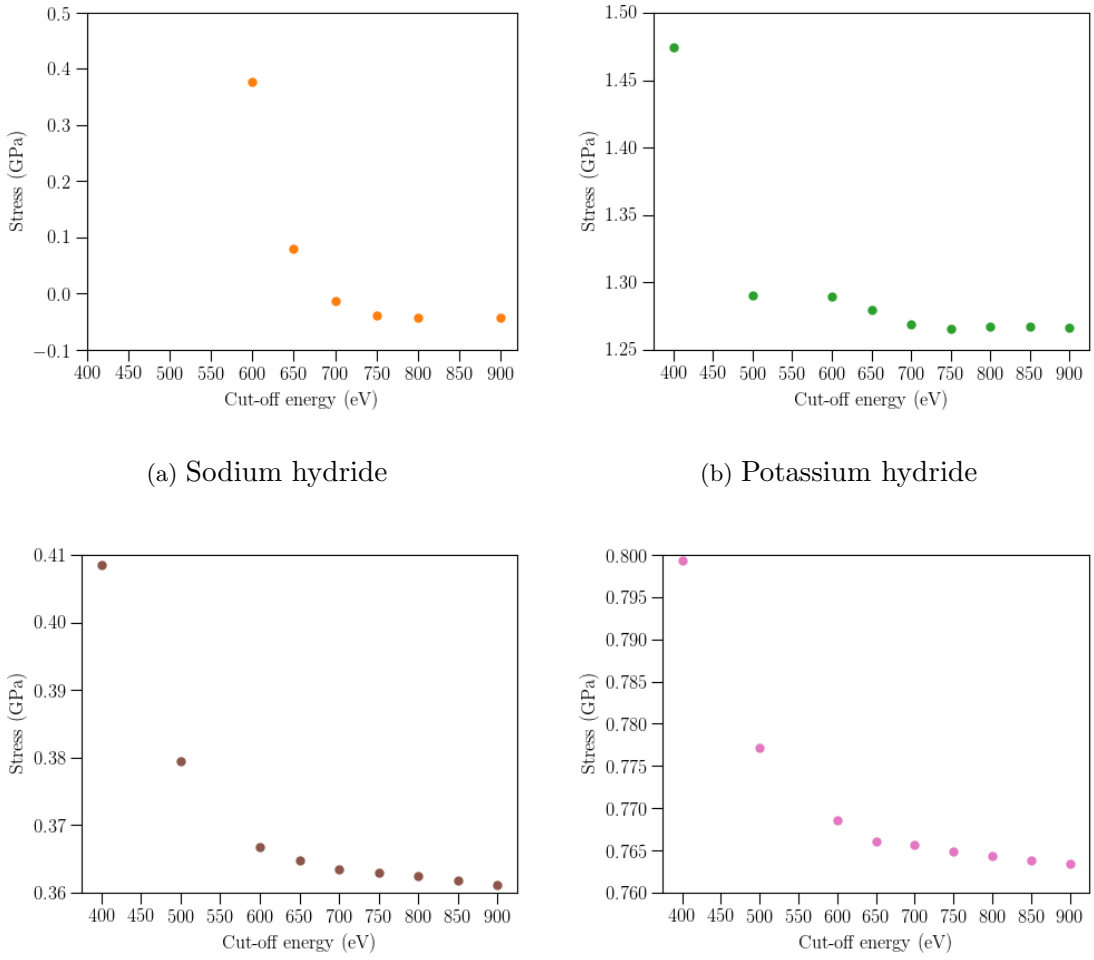

(a) Sodium hydride

(b) Potassium hydride

(c) Rubidium hydride

(d) Caesium hydride

Figure 3.9: Cut-off energy convergence tests for ultrasoft pseudopotentials of non-lithium alkali metal hydrides.

The slabs were geometry optimised and surface rumpling in the rock-salt structures was quantified as a percentage rumpling from the bulk configuration (eq. 3.4). In Figure 3.10, percentage rumpling is plotted against standard ionic radii of the metal in the hydrides.[104] (100) surface rumpling in rock-salt structured alkaline-earth metal oxides by Skorodumova *et al.* are also plotted on the figure for comparison. Skorodumova's calculations were very similar, being performed with a 7 atom layer slab model that was geometry optimised in DFT using a Perdew-Wang (GGA) exchange-correlation functional.

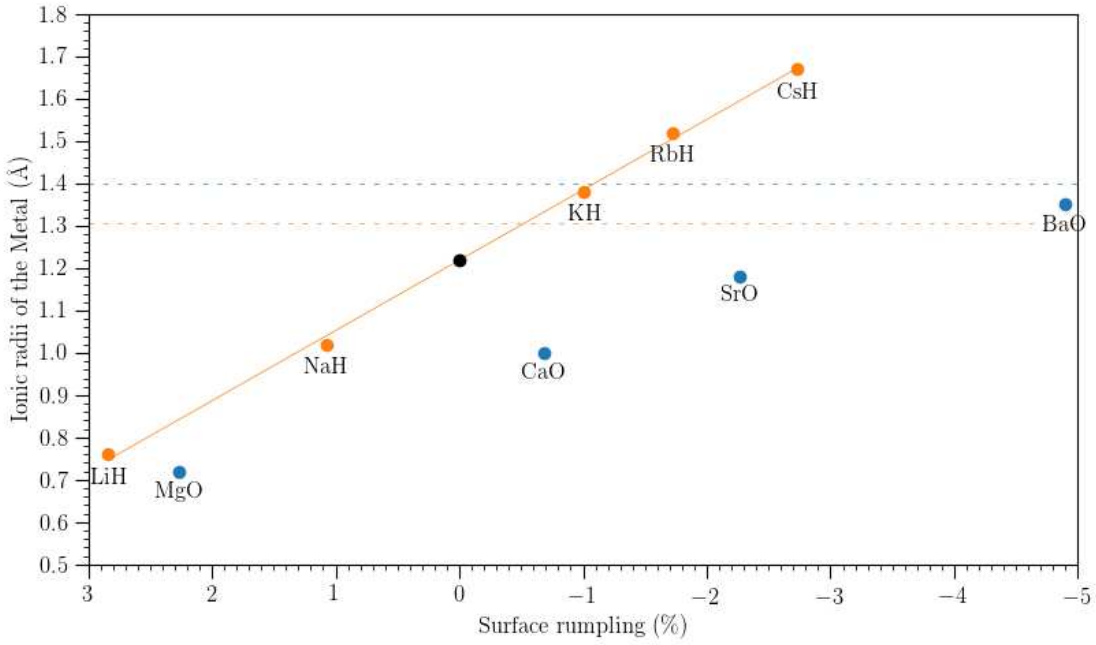

Figure 3.10: (100) surface rumpling in alkali metal hydrides and alkaline-earth metal oxides plotted as a percentage from the bulk positions against the ionic radii of the metals. Surface rumpling for alkaline-earth metal oxides were taken from Ref. 99 and the ionic radii (with a coordination number of VI) from Ref. 104. The black point is the theoretical metal ion size where rumpling would not be observed and the dashed lines correspond to the radii of the hydride (average) in orange and oxygen in blue.

The general trend in Figure 3.10 is that as the metal cation increases in size the direction of surface rumpling shifts from positive, where the cations move toward the interior of the slab, to negative, where the cations move toward the vacuum. The anions move oppositely. This rumpling direction in the metal hydrides is due to the relative size of the ions. It is the smaller of the two surface ions which moves toward the interior of the slab. The hydride radii differ depending on the metal and the average radius is plotted on Figure 3.10. A linear regression line has been fitted to the metal hydride surface rumpling to obtain the y-intercept (marked on figure) as it corresponds to the theoretical alkali-metal radius where the surface does not reconstruct, at 1.22 Å. Although the same trend in rumpling is observed for the metal oxides, the change in direction is not attributed to

the relative size of the ions because oxygen is larger than all of the alkaline-earth metals (dashed blue line in figure). If it was solely a size effect the surface rumpling would be positive for all the metal oxides.

The contribution of the two ion species to the surface rumpling is given in Figure 3.11. The smaller of the two ions in each metal hydride is more mobile and displaces a bigger distance in the z-direction on the surface. The largest ions, caesium and rubidium, do not significantly move from their initial configurations and therefore rumpling is achieved primarily by the movement of the hydride ions.

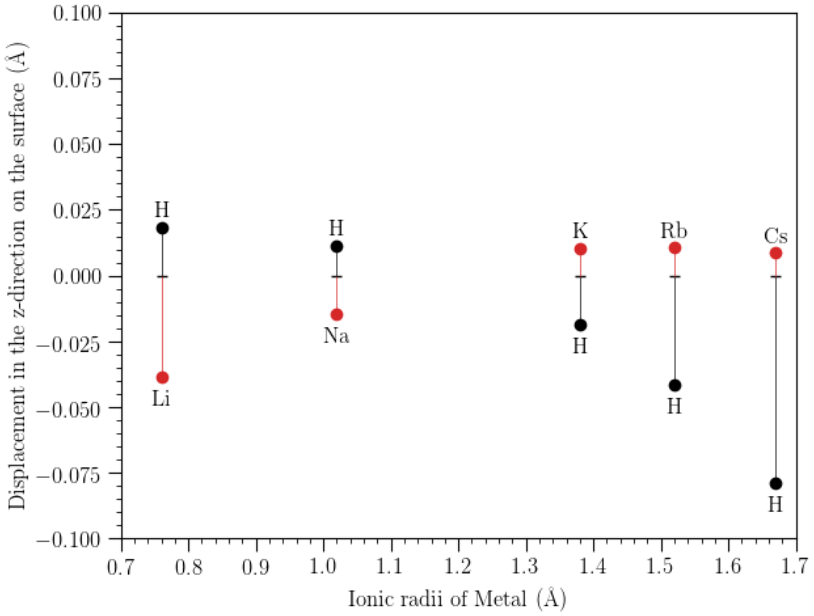

Figure 3.11: Contribution of the metal and hydride ions to surface rumpling in the alkali metal hydrides.

3.4 Interactions of molecules with lithium hydride surfaces

3.4.1 Modelling details

Once the surface structure of lithium hydride has been calculated (Section 3.2.2), the next stage is to simulate the interactions of ammonia on the surface. To investigate the time evolution of this system, Born-Oppenheimer Molecular Dynamics simulations

were performed using CP2K.[93] The theoretical foundations for these calculations were described in Chapter 2. The CP2K package was used because its implementation of MD is superior in performance than CASTEP; due to its aptly named "Quickstep" code, a mixed Gaussian and plane waves approach, which leverages a dual basis set to represent the orbitals, reducing the overall computational costs.[85]

The cut-off energy for the orbitals was converged to within a tolerance of 1 meV, with a 320 Ry cut-off energy (1 Ry = 13.6 eV) using the double-zeta Gaussian basis set (see Figure 3.12). The time step (Δt) was used to integrate the equations of motion to approximate the position of the atoms at $t+\Delta t$ and therefore in order to correctly capture the dynamics of the system, Δt must be smaller then the highest frequency vibration—the motion of the ammonia. A time step of 0.5 fs was used.[40]

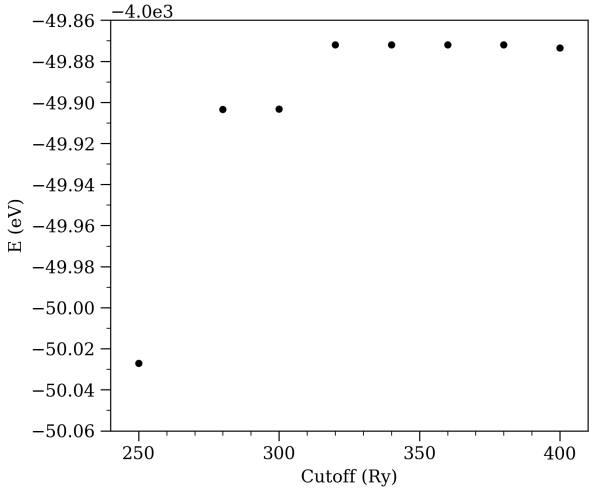

Figure 3.12: Cut-off energy convergence tests for ammonia on lithium hydride performed using a unit cell of lithium amide (same elements and the known end point of this interaction) in CP2K.

The 7-layer asymmetric slab with 2-layers fixed calculated in CASTEP was used as the benchmark to compare with the CP2K reconstruction. The *xy* plane of this 3×3×3 unit cell slab (7-layers) was insufficient to examine the interactions of multiple ammonia molecules because their periodic images are too close; this is not the case with a single

ammonia molecule. For reference, two ammonia molecules are shown on a 3×3 unit cell sub-section of the surface used in Figure 3.26 (b). To prevent periodic image interactions an *xy* plane of 5×5 unit cells was selected as this allows the same slab model to be reused for larger numbers of ammonia molecules in the future. *Ab initio* molecular dynamics simulations are significantly more expensive to compute than geometry optimisations because forces are calculated at every time step, and therefore it was desirable to simplify the surface model further. The approximation made was to use a 5-layer slab in the knowledge that the vacuum beneath the 2 fixed layers would have a larger effect on the innermost layer, and was justified by the surface reconstruction having previously been shown to be localized to the top two layers. Figure 3.13 (a) shows the layer-wise ion displacements of an asymmetric 5-layer slab with 2-layers fixed that was geometry optimised in CP2K (using the mixed Gaussian and plane waves approach) and the 7-layer slab calculated in CASTEP is replotted in (b) from Figure 3.8.

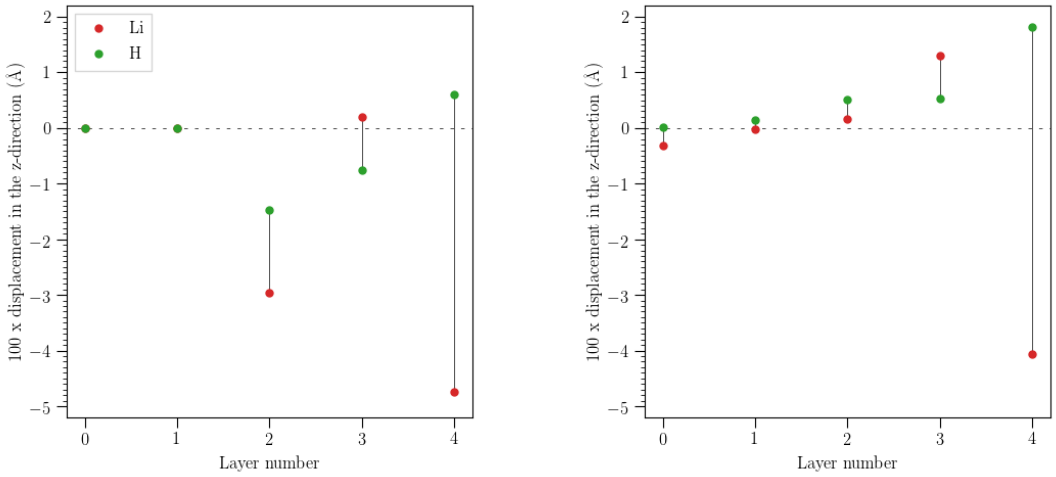

(a) Asymmetric 5-layer slab with 2-layers fixed, calculated in CP2K.

(b) Asymmetric 7-layer slab with 2-layers fixed (mobile 5-layers shown), calculated in CASTEP.

Figure 3.13: Average ion displacement per layer for CP2K and CASTEP models.

In the 5-layer slab model, the three mobile layers displace further towards the slab interior than in the 7-layer slab, because these layers are more significantly affected by the vacuum.

However, most importantly, the distance between the anions and cations within the top two layers are equivalent in both models. In the 5-layer slab, the ions displace by 0.0534 Å in the surface layer and 0.0096 Å in the second layer (layer 3 in figure), compared with 0.0568 Å and 0.0078 Å in the 7-layer slab model. The main difference between these models is the displacement of the innermost layer (layer 2 in figure). The 5-layer slab model with 2-layers fixed well approximates the two upper layers which are the most important for surface interactions; the innermost layer was disregarded in this model.

The surface model for lithium hydride was calculated by geometry optimisations. This is a zero temperature method and therefore the optimised 0 K lattice constant cannot be directly used at higher temperatures, especially in canonical ensemble molecular dynamics simulations where the volume is conserved. The effect of temperature on the lithium hydride lattice constant has been measured empirically up to 300 K by Smith and Leider.[105] This empirical data was fitted to a Debye model in order to derive thermal expansion coefficients that were used to adjust the calculated 0 K lattice constant. The Debye model is based on assumptions that; the crystal is both harmonic and isotropic, elastic waves in the crystal are non-dispersive and that the phonon frequency is correctly approximated by a truncated frequency determined from the number of degrees of freedom. Lattice parameters are accurately modelled by this method at low-temperatures; however, these assumptions break down at intermediate temperatures. The Debye term is given below, taken from Ref. 106:

$$\begin{aligned}\frac{(a-a(T=0))}{T} &= \frac{3}{(\Theta_D/T)^3}\int_0^{\Theta_D/T}\frac{\xi^3}{e^{\xi}-1}d\xi \\ &= \left[\frac{\pi^4}{5(\Theta_D/T)^3} - \sum_{n=1}^{\infty}\left(3+\frac{9}{(n\Theta_D/T)}+\frac{18}{(n\Theta_D/T)^2}+\frac{18}{(n\Theta_D/T)^3}\right)\frac{e^{(n\Theta_D/T)}}{n}\right]\end{aligned} \tag{3.5}$$

Smith and Leider had plotted the lattice constants against temperature. However, due to the age of the paper and a lack of suitable tick marks, these values could not be straightforwardly read off the plot. Image analysis was performed by overlaying a fine-mesh grid to extract the lattice constants for fitting. This is shown in Figure 3.14 along

with the original plot. The calculated 0 K lattice constant at 4.008 Å was adjusted by 0.012 Å from the fitted experimental data to 4.020 Å at 300 K. The MD simulations of molecules on the surface of lithium hydride were all performed at 300 K. This empirical procedure was most appropriate due to the small lattice expansion between 0–300 K, as such changes are observable from high quality diffraction data but difficult to accurately replicate by computation.

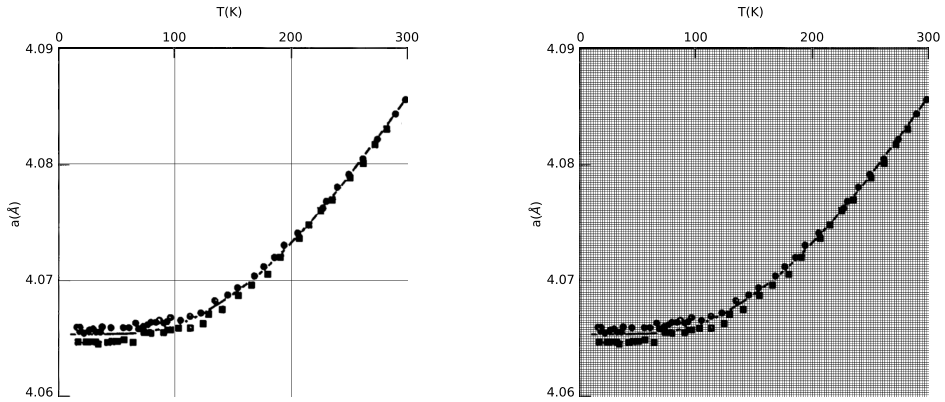

(a) Original image.

(b) Fine-mesh grid overlaid the original image.

Figure 3.14: Lithium hydride lattice constant against temperature from Smith and Leider.

3.4.2 Differing orientations of ammonia on the surface

The ammonia molecule has a distorted tetrahedral geometry because the central nitrogen atom is bonded to three hydrogen atoms and has a single lone pair. Valence Shell Electron Pair Repulsion Theory explains that the repulsion of the lone pair compresses the H–N–H bond angles from an ideal tetrahedron (109.5°) to 107.8°. The distorted tetrahedron loosely resembles the shape of a shuttlecock, where the nitrogen is the base and the hydrogen are the feathers. This analogy is used throughout the Chapter to describe the orientation of ammonia relative to the surface as being either “shuttlecock up” or “shuttlecock down”, illustrated below:

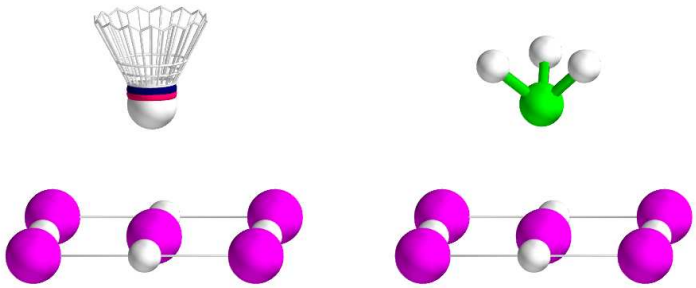

(a) Shuttlecock-up orientation

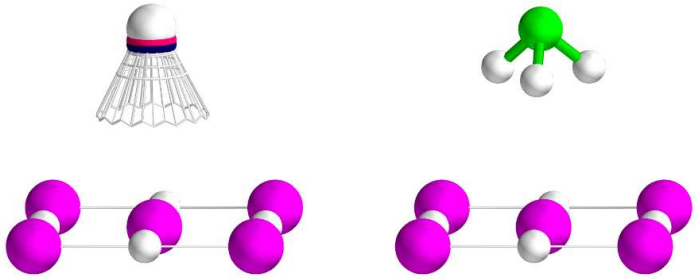

(b) Shuttlecock-down orientation

Figure 3.15: Illustration of ammonia and a shuttlecock above a lithium ion on the surface of lithium hydride.

3.4.3 Ammonia on the surface ($0 < t/ps < 2.5$ and $20 < t/ps < 30$)

The ammonia molecules were initially positioned 3 Å above the relaxed lithium hydride (100) surface in the shuttlecock-up orientation and between the two different surface ion species. This configuration was chosen to prevent the simulation being biased from starting at an energy minimum. From consideration of basic electrostatics, it is clear that the Li—N interaction is dominant and therefore energies for ammonia in the two orientations were calculated at different heights above a lithium ion on the surface in Figure 3.16. The minimum energies represent configurations to avoid at the beginning of the simulations; these heights above the surface are 2.2 Å for shuttlecock-up ammonia and 2.9 Å for shuttlecock down. At 3 Å above the surface in the shuttlecock-up orientation, the starting

configuration for ammonia was sufficiently distant from lithium hydride to avoid biasing the interaction.

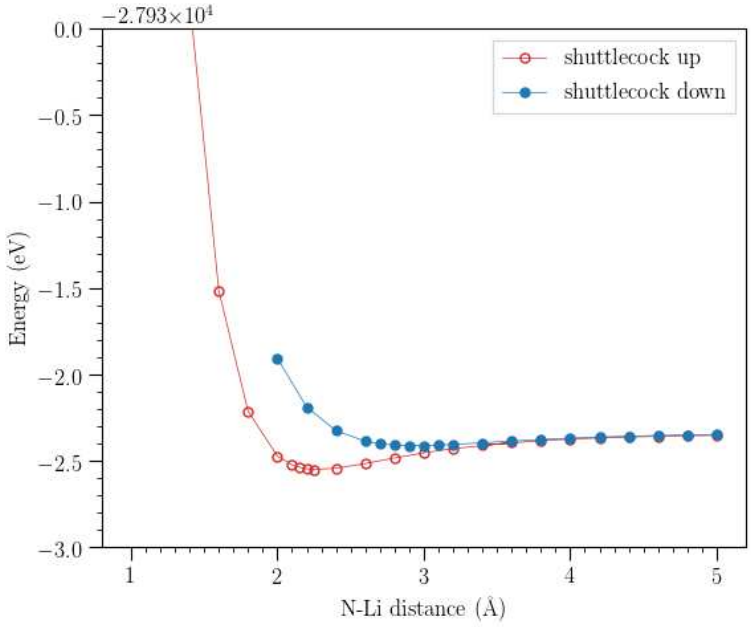

Figure 3.16: Energy differences of ammonia at different heights above a lithium ion on the surface of lithium hydride.

Two scenarios were examined on the surface of lithium hydride: a lone ammonia and the interaction of two ammonia molecules on the surface. The initial configuration for two ammonia molecules was the same as that for one (3 Å above the surface in shuttlecock-up orientations) and the molecules were positioned in close proximity to cause an initial interaction. The trajectories from the two simulations are analysed at a fine level of detail because the features described were common to all of the ammonia simulations performed (Appendix C.2), with the trajectories shown representative of the complete runs. Specific runs were chosen for analysis that highlighted a common surface interaction, and where possible, runs with the longest continuous example of an interaction were used.

The simulations were separated into two parts: first, the molecular movements across the surface and secondly, their landing and attachment to the surface. These stages occur once for the single ammonia but reoccur for two ammonia because the intermolecular

interactions were able to detach an ammonia that had previously landed. At equilibrium, ammonia is attached to the surface via a Li—N ion-dipole bond. This happens early on in the simulation and therefore non-equilibrium events must be included to evaluate the movement of the ammonia across the surface. The system was close to equilibration during these non-equilibrium events because the simulations were well conditioned (see Sections 3.2.2 and 3.4.1): thermal equilibration was achieved at 300 K by 0.5 ps and hysteresis of the thermostat meant the initial movements across the surface were at lower temperatures (see temperature in Appendix A.1).

The first 2.5 ps of the simulation with two ammonia on lithium hydride is plotted in Figure 3.17. At the beginning of the simulation, the two molecules repelled each other which resulted in one molecule moving across the surface and the other rotating above the surface. The time instance shown in the figure captures the moment that a lithium ion beneath the traversing ammonia moved above the surface plane as it bonded temporarily to ammonia; the ammonia consequently landed on the adjacent (to the left) lithium ion. The second ammonia turned shuttlecock down to the surface during rotation which caused repulsion, and the molecule bounced off the surface several times before it eventually stopped once the molecule was orientated shuttlecock up on a lithium ion.

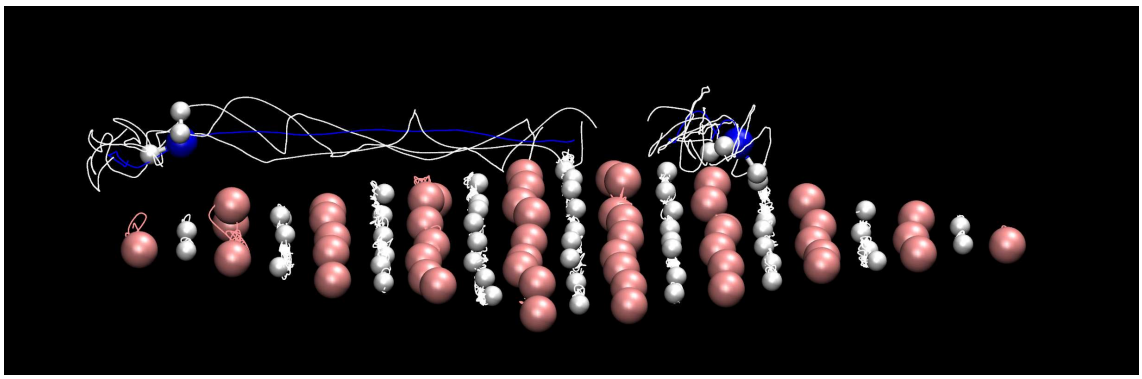

Figure 3.17: Trajectories of two ammonia on the lithium hydride surface at 300 K between 0–2.5 ps. Lithium ions are shown in magenta, hydrogen in white and nitrogen in blue.

The traversing ammonia passes over the surface along the lithium ions along the 110 direction. This is shown more clearly from a separate plot of the traversing ammonia in

Figure 3.18. The nitrogen atom in ammonia moves along the lithium surface ions and at any one time two of the three hydrogen atoms point towards hydride ions that surround the lithium, due to electrostatic attraction. These two hydrogen atoms alternate as ammonia rotates throughout travel. This electrostatic interaction between a positively charged hydrogen in the ammonia molecule and hydride ions ($\overset{\delta\oplus}{\mathrm{H}}$ and H^-) stabilizes the straight-line trajectory of ammonia along the lithium and is possible because of the tetrahedral geometry.

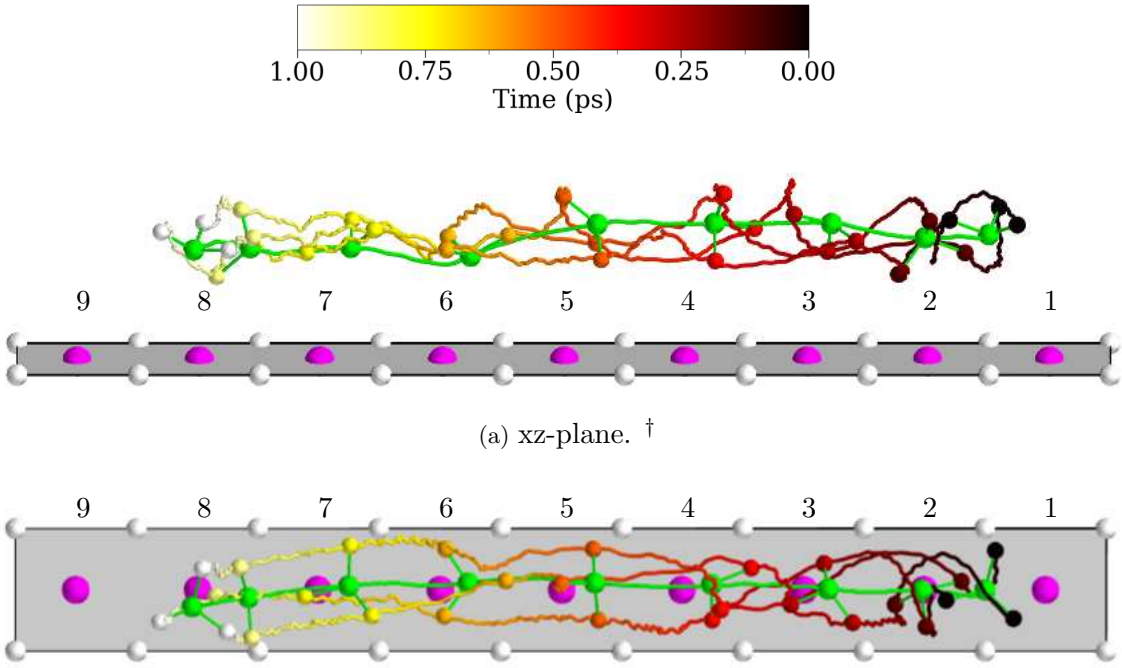

(a) xz-plane. †

(b) xy-plane (above the surface). †

Figure 3.18: Trajectory of ammonia along the (100) surface of lithium hydride taken from the two ammonia simulation between 0–1 ps. A sub-section of the overall surface is shown with the surface structure at 0 ps. Ammonia is plotted on the trajectory every 125 fs. Lithium ions are shown in magenta, hydride in white, nitrogen in green and the hydrogen are coloured by time. † The lithium numbers are for later reference in Figures 3.19–3.21

The first 2.5 ps of the simulation captures the movement of an ammonia molecule across the surface (0–0.99 ps) and its initial landing (0.99–2.5 ps). These events are examined in

Figures 3.19–3.21 with a vertical line used to mark their division. Figure 3.19 contains the distance from the central nitrogen atom in ammonia to the lithium ions numbered in Figure 3.18. The distance between ammonia and lithium ions (2) to (7) decreases sequentially as ammonia travels towards the ions and then increases again once it had passed over. It is not until lithium (6) that ammonia is close enough to bond to the surface with a minimum Li—N distance of 1.82 Å, the previous minimum was 2.79 Å above lithium (5) (see Figure 3.18 (a)). Ammonia does not land despite being in the shuttlecock-up orientation, which is later determined as the favourable landing orientation. The failure to land on lithium (6) was because of the substantial kinetic energy of the ammonia and its closeness to the surface; the ideal Li—N bond distance for the shuttlecock-up orientation was determined to be 2.2 Å (see Figure 3.16). There is a damped oscillation of the Li—N bond in the period between ammonia landing on lithium (8) at 0.99 ps to 1.35 ps, as ammonia stabilises on top of the lithium ion (lithium (8) in Figure 3.19). The average Li—N bond length after this initial oscillation was 2.177 Å (1.35–2.5 ps) which is in agreement with the single point energy calculations from Figure 3.16. The thermal motion of ammonia across the surface (after 0.99 ps) is transferred to the oscillations in the Li—N distance from lithium (5) to (7) (also lithium (1) to (4) but not shown on the y-axis range). Their oscillation periods are the same but the amplitudes increase the further the lithium ion are from the ammonia, due to a reduction in the angle between the surface plane and ammonia.

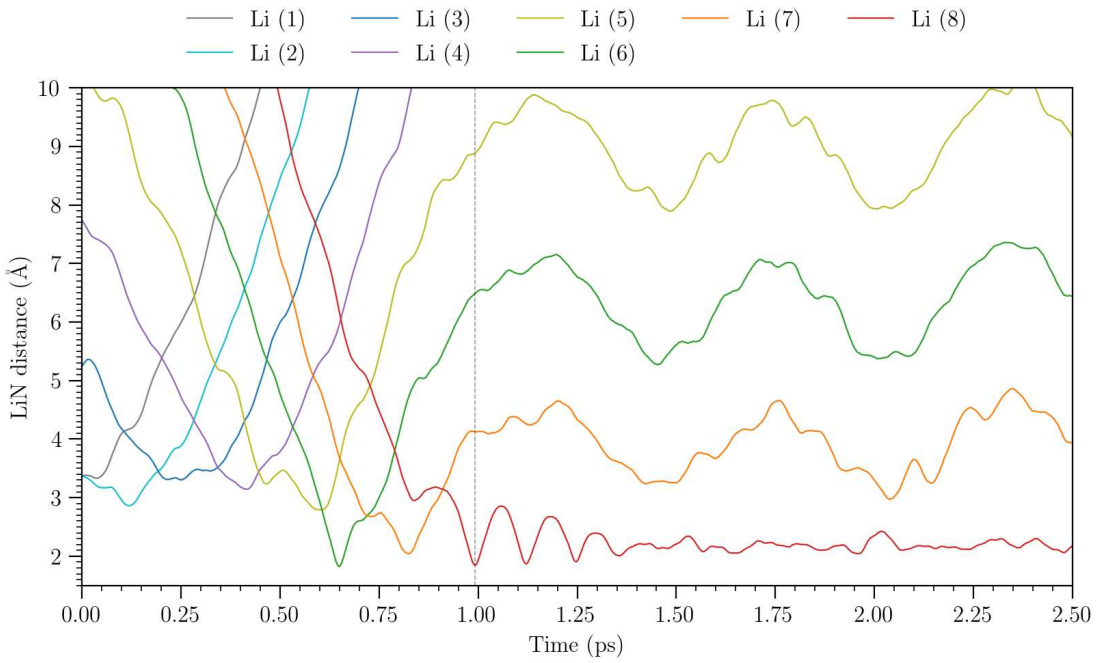

Figure 3.19: Lithium-to-nitrogen distance between ammonia and the lithium surface ions it moves across during the first 2.5 ps of the run.

To ascertain how the lithium ions on the surface responded to the traversing ammonia, their z-positions within the supercell were plotted as the dominant axial component of the surface motion, in Figure 3.20. Lithiums (1) to (5) are greyed out on the figure due to ammonia being too far above these surface ions to land. Between 0.48–0.65 ps ammonia descends onto the surface due to the structure orientating shuttlecock up, as the nitrogen is positioned below the hydrogen: at the same time lithium (6) moves above the surface plane towards the ammonia. Lithium (6) and lithium (7) both temporarily bonded to the traversing ammonia by moving vertically towards it (peaks are labelled). Immediately after landing, the z-positions of the nitrogen in ammonia and lithium (8) are out of phase, and this corresponds exactly to the damped oscillation in Figure 3.19 (0.99 ps to 1.35 ps). Once ammonia has settled on the surface, the two atoms move together in phase (1.35–2.5 ps).

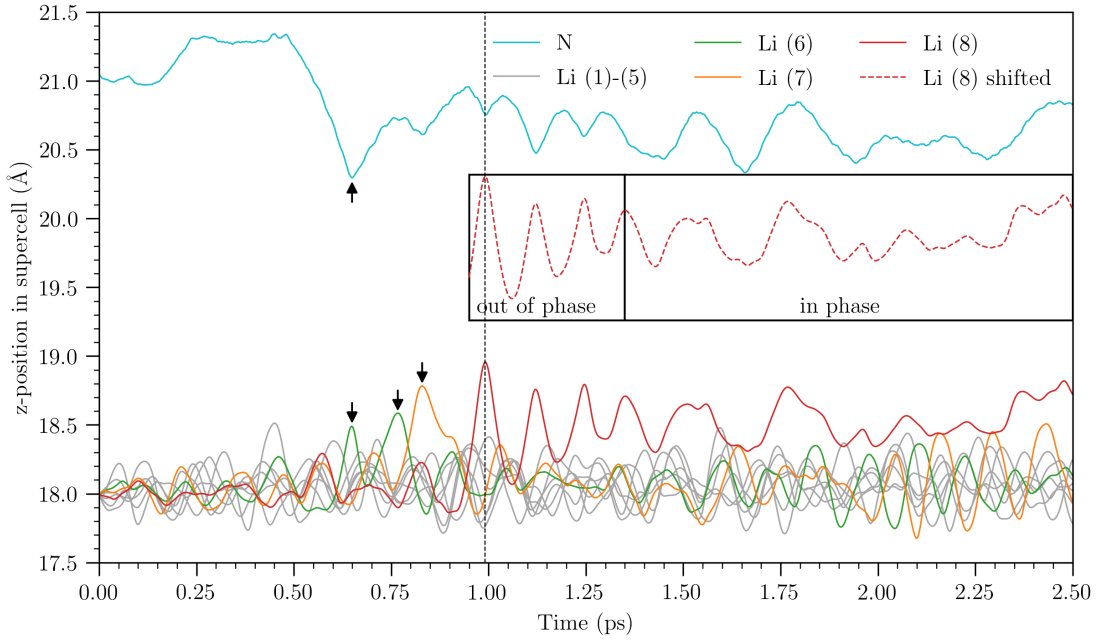

Figure 3.20: Vertical position in the supercell of nitrogen in ammonia and the lithium surface ions its moves across during the first 2.5 ps of the run.

The speed and cumulative distance of ammonia as it moved across the surface are presented in Figure 3.21. Time steps for the minimum Li—N distance to each surface Li^+ ion (2–8) have been marked on the Figure. The initial intermolecular repulsion accelerated the ammonia molecule and it was not until the molecule descended onto the surface (beginning at 0.48 ps) that the electrostatic attraction to the surface ions could dominate the interaction. Ammonia slowed substantially from its interaction with lithium (6) and (7), to the point where it landed when it approached lithium (8). The short time frame between lithium (5) and (6) minima was due to an orientation change to shuttlecock up, and as a result, the minimum distance to lithium (5) was long at 2.79 Å.

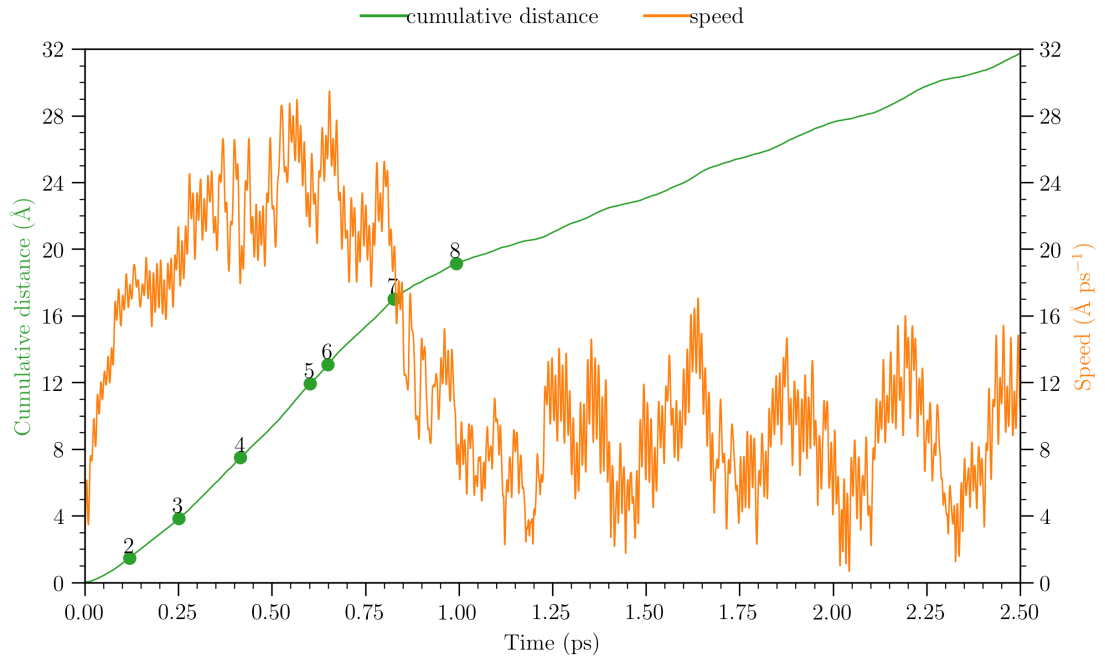

Figure 3.21: Speed and cumulative distance travelled by ammonia moving across the lithium hydride surface during the first 2.5 ps of the run. The time steps that correspond to the minimum Li—N distances as ammonia moves across the lithium ions on the surface are numbered with reference to Figure 3.18.

In the second part of the simulation, ammonia lands on the surface. Ammonia as a polar molecule attaches to the surface by forming a Li—N bond, from electrostatic attraction between the negative charge on nitrogen and positive charge of the lithium cation. This restores the octahedral coordination of the lithium ion which had been lost in the creation of the (100) surface. Landing occurs in the shuttlecock-up orientation with the nitrogen toward the surface and hydrogen toward the vacuum. This allows Li—N bond formation unimpeded by the hydrogen in ammonia (see Figure 3.15 (a)). The lithium ion shifts above the plane of the surface to bond to ammonia.

Once landed, the orbit of ammonia above a lithium is related to its distorted tetrahedron shape and it remains shuttlecock up to the surface. It cannot rotate shuttlecock down without significant energetic penalty because this would require breaking the Li—N bond. Figure 3.22 contains a 10 ps trajectory of ammonia bonded to the surface (after

landing). This was taken from the single ammonia calculation because the interaction was uninterrupted without the presence of another ammonia on the surface.

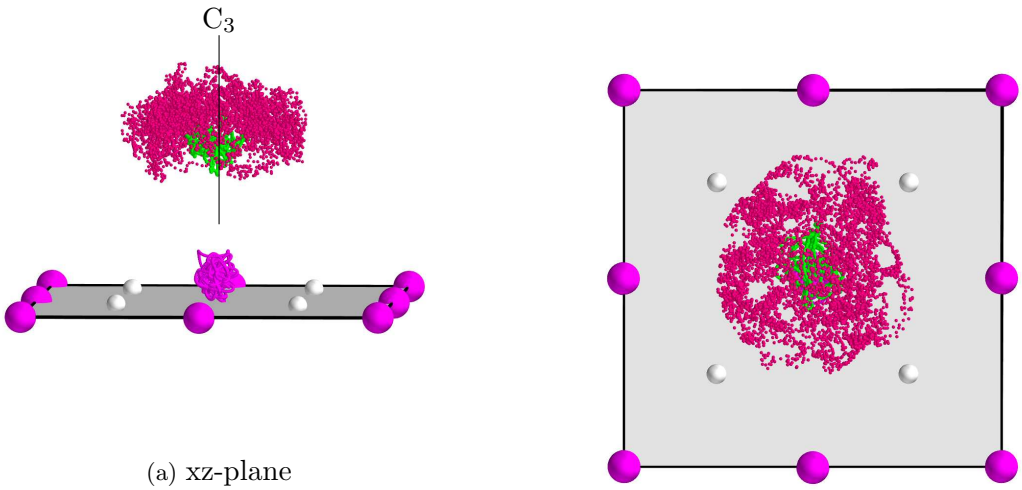

(a) xz-plane

(b) xy-plane

Figure 3.22: Ammonia landed on lithium hydride at 300 K between 20–30 ps. The trajectory is plotted for ammonia and the lithium ion its landed on every five time steps; average positions are used for the remaining surface atoms. Lithium are shown in magenta, hydride in white, the nitrogen trajectory in green and hydrogen trajectory in red-pink.

There are two rotations to consider for ammonia once landed, the hydrogen around the nitrogen and the tilt of the tetrahedron from the "ideal" shuttlecock-up orientation. The hydrogen atoms in ammonia rotate freely around the C_3 axis of the molecule when it is isolated on the surface (axis shown in Figure 3.22 (a)). This is not the case when a second ammonia is nearby; this is discussed later in Section 3.4.4. Ammonia bonded shuttlecock-up on the surface tilts from the vertical as it orbits around lithium. If tilted significantly, this could lead to the detachment of ammonia; however, during such instances the tetrahedral geometry results in bonding arrangements with the surface which restricts its freedom of movement and reduces the likelihood of detachment. The next closest surface ions after the lithium which bonds to ammonia are four hydrides; it is these which stabilise ammonia on the surface. The hydrogen atoms in ammonia, when the structure

is tilted off the vertical, come in closer proximity to these surface hydrides and can form temporary dihydrogen bonds that stabilise the arrangement—the tetrahedral geometry means that two hydrogen atoms can simultaneously interact with two hydrides. While the Li—N bond is the dominant interaction, these weak dihydrogen bonds effectively trap the tetrahedral structure on top of the lithium. This is shown in the Figure 3.23. The formation of three bonds (Li—N, 2 × dihydrogen) to the surface stabilises ammonia when 1 dihydrogen bond breaks the 2 remaining bonds restrict ammonia's motion, causing it to tilt back onto the surface and the 3rd hydrogen forms a new dihydrogen bond. The consequence of the tetrahedral structure is an "orbiting" motion around lithium.

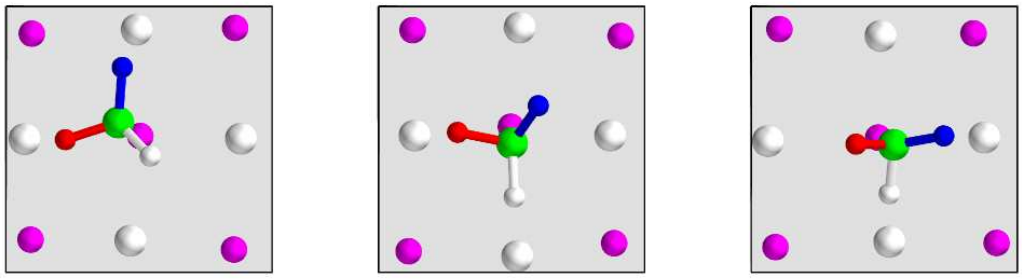

Figure 3.23: Ammonia orbiting around a lithium ion via the formation of two dihydrogen bonds. Lithium are shown in magenta, hydride in white, nitrogen in green and N—H bonds in red, white and blue respectively.

3.4.4 A second ammonia on the surface ($10 < t/ps < 35$)

The descriptions of ammonia on the surface, until now, were common to both simulations. The inclusion of a second ammonia introduced the possibility of intermolecular interactions and resulted in the propagation of the ammonia molecules as a dimer along the surface. Hydrogen bonds can form between the hydrogen of one ammonia and the nitrogen of another, because they are polar molecules with partial positive charges on the hydrogen and a partial negative charge on the nitrogen. In preliminary testing, the larger the number of ammonia molecules on the surface the more difficult it became to decouple their motifs,

and to that end, intermolecular interactions were analysed from two ammonia on the surface. The trajectories described represent some of the possible surface interactions for multiple ammonia on lithium hydride—these interactions were also observed from 9 NH_3 on the surface (Appendix C.2), however, the trajectories were limited due to the additional competition between molecules.

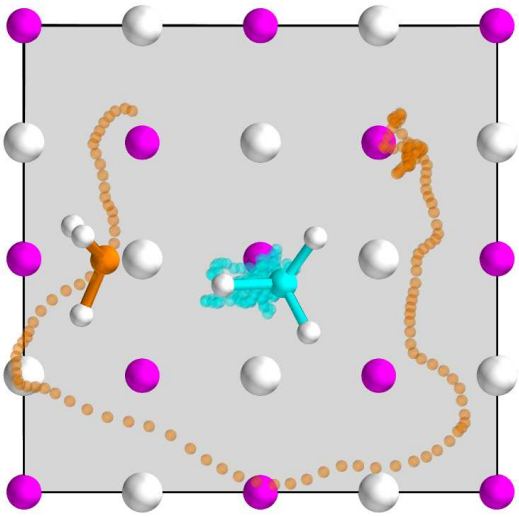

Figure 3.24: Trajectories for two ammonia that form intermolecular hydrogen bonds to one another on the surface of lithium hydride at 300 K, between 17.5–21 ps. The nitrogen atoms from the different ammonia are shown separately in blue and orange so that they can be easily traced, lithium ions are shown in magenta and hydrogen in white.

Figure 3.24 gives an overview of the interactions between two ammonia molecules on the surface of lithium hydride. These differ from previous observations as ammonia no longer move in straight-lines across the surface. The first ammonia is bound to a lithium ion shuttlecock up and the second ammonia orbits the first on its side, via a hydrogen bond; both are a consequence of the distorted tetrahedral geometry of ammonia. The nitrogen atom in the orbiting ammonia faces towards the hydrogen of the landed ammonia. This hydrogen-bonding positions the two molecules too close to the surface to both land, as it would require the two molecules to reside on nearest-neighbour lithium ions that are

2.8 Å apart. The ammonia must instead exchange configurations on the surface; when one ammonia lands the other is released. This mechanism propagates the two ammonia along the lithium hydride surface; however, it is not an efficient method of travel as ammonia moves a total straight-line distance of 4.46 Å in 25 ps.

This interaction between two ammonia is best captured from their orientations with respect to one other, and specifically the elevation angles. Figure 3.25 defines the orientations of the molecules on the surface from their elevation and azimuth angles (vertical and horizontal angular distances); an elevation of 0° refers to the shuttlecock-up orientation and 180° to shuttlecock down. The description of a hydrogen bond on the surface as between one ammonia landed shuttlecock up and another orbiting the first on its side, translates in elevation angles to the simultaneous observation of an ammonia at $< 30°$and 90°. This is the main feature of Figure 3.25 (b), with ammonia in one of the two orientations and exchanges between the orientations occurring throughout the simulation—when one ammonia lands the other is released. The elevation angle of the landed ammonia at $< 30°$ is tilted from the "ideal" shuttlecock-up orientation to facilitate the hydrogen bond formation to the second ammonia. The few exceptions to the ammonia molecules being in this configuration (i.e. instances where both ammonia are in landed orientations) have been highlighted in boxes on the plot: 21.5–22.5 ps correspond to both molecules detaching from the lithium ions and 26.5–28.5 ps to the molecules being sufficiently separated to allow this configuration.

The azimuthal angles for ammonia hydrogen-bonding together on the surface are not restricted to two angles, as in elevation, and instead ammonia can rotate through 360°. The speed of rotation however depends on ammonia's configuration (whether landed or orbiting), as the orbiting ammonia has to travel a circumference around the landed ammonia to rotate in azimuth; rotation, therefore, is comparatively slow. A complete rotation in azimuth for an orbiting ammonia is highlighted in Figure 3.25 (c) and took 3.8 ps starting from 30°, during this time the landed ammonia fully rotated fifteen times. The orbiting ammonia does not have to fully rotate around the landed ammonia and therefore there are instances where ammonia orbits back and forth over a narrower azimuth range, these

rotations are still slow so the configurations are distinguishable—examples are highlighted in Figure 3.25 (d).

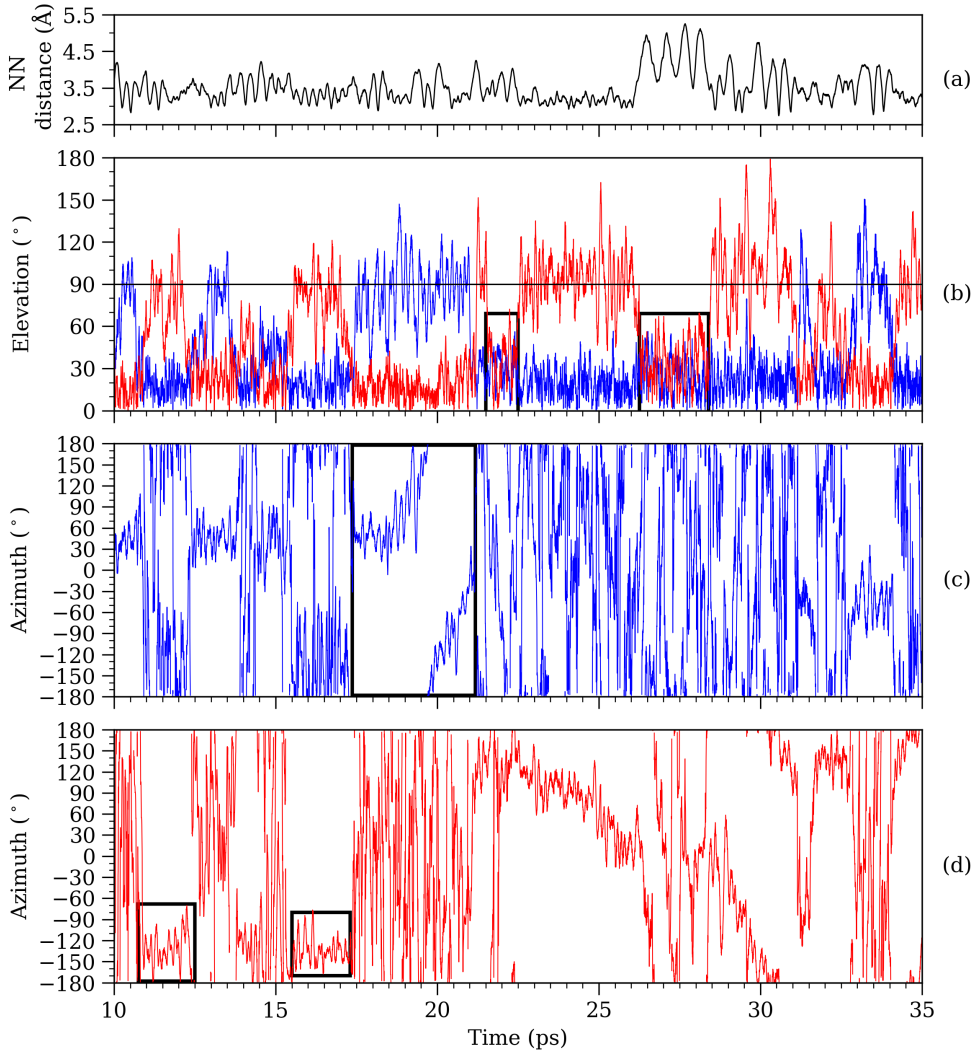

Figure 3.25: Orientations and intermolecular distances for two ammonia interacting on the surface of lithium hydride at 300 K over 25 ps. Azimuth and elevation angles are coloured to correspond to the respective ammonia, in either red and blue.

The formation of a hydrogen bond between ammonia restricts the rotation of the molecule that is bond shuttlecock up to a lithium ion on the surface. Figure 3.26 (a, b, c) demonstrates this restricted rotation from separate coloured distributions of the three hydrogen atoms in the landed ammonia. The hydrogens cannot freely rotate around the triangular face of the tetrahedron (along the C_3 axis) because of the presence of the orbiting ammo-

nia. Hydrogen atoms in the orbiting ammonia are not separately coloured because there is no ordering to their distributions. For comparison, a lone ammonia on the surface in Figure 3.22 is replotted in (d). Over the equivalent time frame, this isolated ammonia on the surface freely rotates.

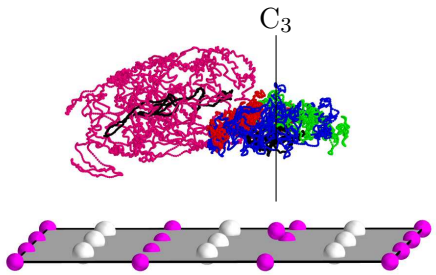

(a) xz-plane

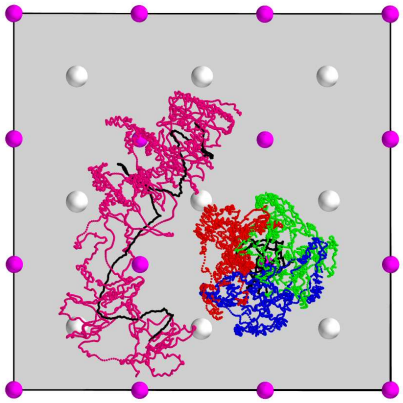

(b) xy-plane

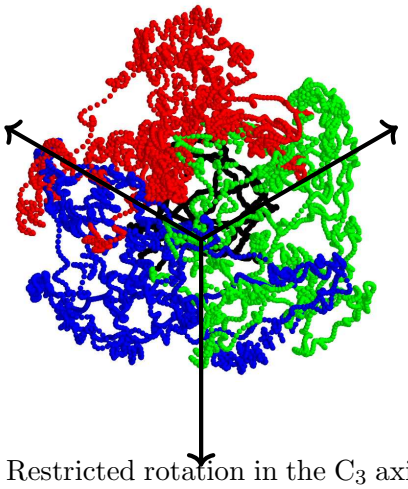

(c) Restricted rotation in the C_3 axis. Arrows overlaid 120° apart.

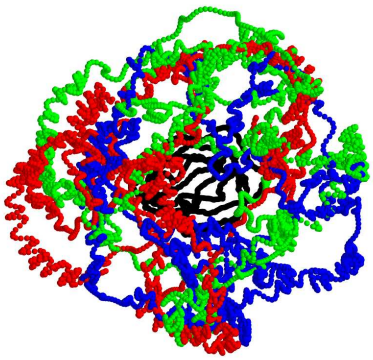

(d) Unrestricted rotation in the C_3 axis.

Figure 3.26: Hydrogen rotation in ammonia landed on lithium hydride, with (a, b, c) and without (d) a hydrogen bond to a second ammonia molecule. The trajectories of ammonia in (a, b, c) were taken between 23–26 ps and (d) from an arbitrary 3 ps from Figure 3.22. Lithium ions are shown in magenta and hydride in white. The nitrogen trajectories are shown in black, three hydrogen from the orbiting ammonia in red-pink and three hydrogen from the landed ammonia in red, green and blue respectively.

The interactions observed for ammonia on the lithium hydride surface are in agreement with the previously reported molecular and cluster models: that ammonia bonds to lithium hydride by the formation of Li—N with hydrogen orientated so the bond is unhindered. [39, 40, 41] Although the formation of lithium amide did not occur on the surface, the co-ordination of ammonia was consistent with the gas phase simulations as ammonia bonded shuttlecock up on a lithium ion, where the Li—N bond was the dominant interaction, and temporary dihydrogen bonds formed to the hydrides. This shuttlecock-up arrangement represents the minimum energy configuration for ammonia before its transition state in the formation of lithium amide, and facilitates the approach of the hydrogen in the reaction. The slab model used is a more realistic representation of the surface than small LiH clusters and ammonia's interactions have been shown to be the result of simple geometric and electrostatics arguments.

3.4.5 Other molecules related to ammonia

The original intention of the surface model was solely to investigate the interactions of ammonia as part of the Li–N–H system. The importance of molecular shape to these interactions however became apparent early in the simulations and therefore the surface study was extended to include molecules with geometries closely related to ammonia.

Ammonia has a distorted tetrahedral geometry because the central nitrogen atom is bonded to three hydrogen and contains one lone pair of electrons, this is explained from VSEPR theory by the stronger repulsion of the lone pair than hydrogen compressing the H–N–H bond angles to 107.8°. Methane and water molecules were chosen for comparison with ammonia because they are also related to a regular tetrahedron (and contain hydrogen bonds). This structural relationship is highlighted in Figure 3.27. Starting with a distorted tetrahedron (three bonds and one lone pair), the lone pair can be substituted for a bonded atom or vice versa. Methane has a regular tetrahedral geometry as the four hydrogen atoms around the central carbon equally repel one another, resulting in H–C–H bond angles of 109.5°. Water has a bent shape as the oxygen contains two hydrogen and two lone pair of electrons, with a H–O–H angle of 104.5°—the angle compression is as

explained previously for ammonia.

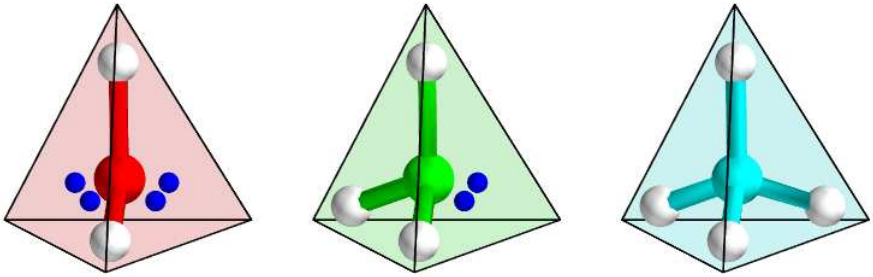

(a) (b) (c)

Figure 3.27: Structure of (a) H_2O (b) NH_3 and (c) CH_4, with their relationship to a regular tetrahedron highlighted. Electron lone pairs are shown in blue, hydrogen in white, oxygen in red, nitrogen in green and carbon in cyan.

The effect of fluorine substitutions in ammonia were investigated as a means of further examining the distorted tetrahedral structure on the surface of lithium hydride. The three possible fluorinations for ammonia were all simulated on the surface of lithium hydride for completeness: monofluoroamine (NFH_2), difluoroamine (NF_2H) and trifluoroamine (NF_3). These are model systems used to study structural properties on the surface, and as such there is little-known experimentally about either NFH_2 or NF_2H—presumably because selective fluorination of ammonia would be difficult to achieve experimentally and the structures would likely dissociate.

Given the paucity of information about monofluoroamine and difluoroamine, the geometry optimised structures of the three fluoroamines were first assessed. Geometry optimisations were performed in CP2K independent from the surface and the optimised structural parameters are tabulated in Table 3.1. First, fluorine is larger than hydrogen with a radius of 0.57(3) Å compared to 0.31(5) Å, and therefore the nitrogen-fluorine bond is longer (for reference, nitrogen has a radius of 0.71(1) Å).[†] Secondly, both H–N–F and F–N–F bond angles compressed with increased fluorine substitutions in the structure. This compression is explained by a change in the electron distribution within the structures, as fluorine is more electronegative than nitrogen which means the dipole moment of N—F is inverted,

[†]covalent atomic radii taken from an aggregate data set of crystallographic measurements in Ref. 107

i.e. $\overset{\delta\oplus}{\mathrm{N}}$—$\overset{\delta\ominus}{\mathrm{F}}$ compared to $\overset{\delta\ominus}{\mathrm{N}}$—$\overset{\delta\oplus}{\mathrm{H}}$. In NF_3, as the electron density in the bonds is further from the N than in NH_3, then the N—F bonds can contract further from the lone pair thus reducing the angle. In the mixed fluoroamines, the partial positive charge on $\overset{\delta\oplus}{\mathrm{H}}$ is attracted to the partial negative charge on $\overset{\delta\ominus}{\mathrm{F}}$. This $\overset{\delta\oplus}{\mathrm{H}}$- - -$\overset{\delta\ominus}{\mathrm{F}}$ interaction therefore compresses the H–N–F bond angle and as a consequence the F–N–F bond angle in difluoroamine is larger.

Table 3.1: Structural parameters of fluoroamines optimised in CP2K at 0 K.

	bond length (Å)		angle (°)		
	N—H	N—F	H–N–H	H–N–F	F–N–F
monofluoroamine	1.04	1.46	103.4	100.6	-
difluoroamine	1.05	1.42	-	99.0	103.5
trifluoroamine	-	1.40	-	-	101.9

The cut-off energy determined for Li–N–H systems (Figure 3.12) cannot be used for molecules containing carbon, oxygen and fluorine. Convergence tests were performed for the pseudopotentials using the same double-zeta Gaussian basis set shown in Figure 3.28. Carbon and oxygen were converged to better than 1 meV using the same cut-off energy as Li–N–H, at 320 Ry, in agreement with previously published work from the group.[108] Fluorine converged to 2 meV with a higher cut-off energy of 500 Ry.

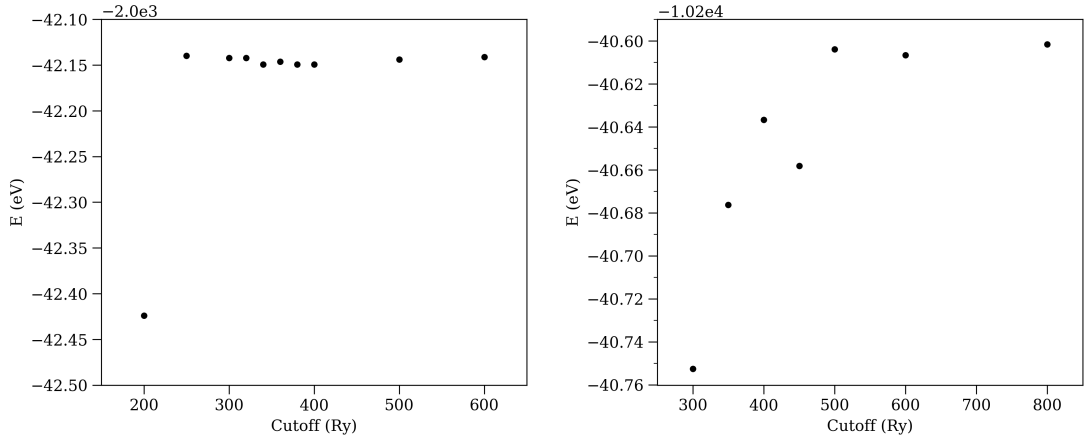

(a) C and O

(b) F

Figure 3.28: Goedecker-Teter-Hutter pseudopotential convergence for water, methane and fluoroamines.

3.4.6 Water ($20 < t/ps < 30$) and methane ($0 < t/ps < 10$) on the surface

The distorted tetrahedral shape of ammonia has been shown to be fundamental to how it interacts on the surface of lithium hydride. The straight-line movement of ammonia across the surface, its shuttlecock-up orientation in landing and subsequent trapping of ammonia on the surface are all consequences of its geometry. Methane and water both behave very differently to ammonia on the surface of lithium hydride, despite all being structurally related to a regular tetrahedron.

Methane has a regular tetrahedral geometry, with four hydrogen atoms around a central carbon atom, and it is non-polar because of the symmetry of the structure. During the simulation of methane on lithium hydride, the molecules were repeatedly repelled from the surface into the vacuum and therefore the calculation was stopped after 10 ps. Methane is not attracted to lithium hydride since it is non-polar and does not contain a lone pair of electrons necessary to interact.

Water has a bent geometry due to having two hydrogens and two lone pairs of electrons. The electrons are unevenly distributed in water and therefore it is polar, containing a

partial negative charge on oxygen and partial positive charge on hydrogen. This polarity makes it more comparable to ammonia than methane. The simulation of water on the lithium hydride surface cannot be conveniently divided into the movement across the surface and its landing because landings are short-lived. There are two electrostatic interactions for water on the surface of lithium hydride that correspond to the opposite charges in the molecule, analogous to ammonia, lithium-oxygen bonds and dihydrogen bonds (hydrogen to hydride). The motion of water on lithium hydride is unstructured when compared with ammonia, as it tumbles over the surface because of the additional freedom to rotate due to the absence of a third hydrogen atom. Water forms two points of contact with the surface via a Li—O bond and dihydrogen bond, when one of these two bonds break the molecule is free to move. The bent structure is less bulky than a distorted tetrahedron and therefore the hydrogen do not obstruct the ability of oxygen to bond to a lithium ion on the surface: water can either land with the hydrogen facing towards the surface or the vacuum. This is not possible for ammonia because the triangular face of hydrogen prevents the nitrogen from approaching the lithium ion when in the shuttlecock-down orientation, and hence ammonia lands exclusively shuttlecock up.

Once landed above an oxygen, temporary dihydrogen bonds are formed between water and the surface in a similar manner to ammonia. However, the more free rotation of the molecule means that water on top of a lithium ion can roll over on the surface to propagate along, and this is facilitated by the formation of a dihydrogen bond. This is shown in Figure 3.29. The hydrogen bonds to a hydride which anchors water to the surface while the oxygen atom rolls over onto an adjacent lithium ion. Water moves along lithium ions on the surface due to the rotation of the molecule. The Li—O bond is the dominant surface interaction for water. However, due to the continuous rotation of the molecule, this competes with the temporary formation of dihydrogen bonds. This differs from ammonia where the distorted tetrahedron geometry means the dihydrogen bonds stabilise the landing configuration and effectively trap ammonia shuttlecock up on the surface. The motion of water on lithium hydride was due to enhanced molecular rotations caused by the absence of a third hydrogen atoms, and this structural change destroyed the orderly motion observed in ammonia from the distorted tetrahedron structure.

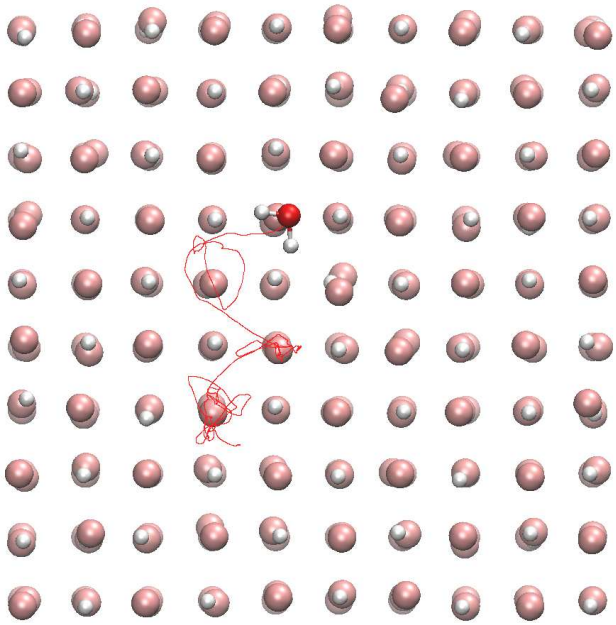

Figure 3.29: Trajectory for water on the surface of lithium hydride at 300 K over 10 ps. The lithium are shown in pink, hydrogen in white and oxygen in red.

3.4.7 Monofluoroamine ($10 < t/ps < 20$), difluoroamine ($10 < t/ps < 20$) and trifluoroamine ($0 < t/ps < 3.66$) on the surface

The substitution of hydrogen for more electronegative fluorine changes the polarity of the molecules, and the distribution of these partial charges significantly effects how a distorted tetrahedron can move along the surface of lithium hydride. Trifluoroamine is conceptually the easiest to understand, as fluorine is more electronegative than nitrogen so the dipole moment of the distorted tetrahedron is inverted compared to ammonia (with a partial positive charge on nitrogen and partial negative charges on the fluorines). It could therefore be hypothesized that trifluoroamine would preference the shuttlecock-down orientation in landing, as the opposite orientation to ammonia would achieve the same direction for the partial charges approaching the surface. Fluorination in addition to changing molecular polarities increases the reactivity of the molecule, and as a result, trifluoroamine dissociates almost immediately on the surface. Once trifluoroamine comes close to lithium hydride, a nitrogen-fluorine bond breaks, fluorine embeds between two

lithium ions and a hydrogen is later expelled, this reaction means that neither the motion on the surface or its landing can be determined.

The tetrahedral structure of monofluoroamine is lopsided towards the N—F bond. Both physically, due to the larger atomic radius of fluorine to hydrogen and in its electron distribution, as fluorine is most electronegative so the direction of the dipole moment is towards fluorine rather than nitrogen. The triangular base of the tetrahedron is irregular rather equilateral as the N—F bond is longer than N—H, and therefore fluorine is below the plane of the two hydrogen atoms. The motion of monofluoroamine on lithium hydride is dominated by the interaction of the fluorine which drags the rest of the molecule along. Fluorine can interact unhindered by the remainder of the molecule because of the lopsided shape of monofluoroamine with a longer N—F bond. It is the electrostatic attraction between fluorine and the lithium ions that moves the molecule forward, as the fluorine moves between adjacent lithium on the surface. This is shown in Figure 3.30. Molecular rotations lead to the temporary formation of dihydrogen bonds. However, these are readily broken due to fluorine propagating the molecule along the surface. Monofluoroamine lands on lithium hydride in the shuttlecock-up orientation with nitrogen to the surface. This is comparable to ammonia and is further evidence that the landing configuration is linked to the general tetrahedron shape as an unimpeded approach. The shuttlecock-up orientation is however unbalanced on top of a lithium ion due to the fluorine atom, with repulsion between the fluorine and surrounding hydrides—such that landed monofluoroamine will reorientate so that the N—F bond is vertical to the surface plane. Once landed, monofluoroamine quickly formed ammonia because the nitrogen is electron-deficient so easily bonds to a hydride, and fluorine repulsion in the shuttlecock-up orientation placed the nitrogen in closer proximity to the surface. The fluorine embedded in the surface at the hydride vacancy. The entire interaction of monofluoroamine with lithium hydride is dominated by fluorine.

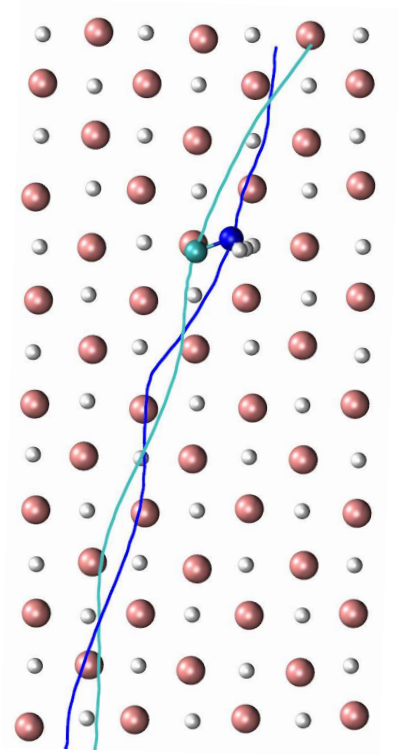

Figure 3.30: Trajectory for monofluoroamine on the surface of lithium hydride at 300 K. The lithium are shown in pink, hydrogen in white, nitrogen in blue and fluorine in teal.

The substitution of a second hydrogen for fluorine in difluoroamine means that the structure is bulkier. The one-sidedness of the motion experienced in monofluoroamine was also removed. The base of the tetrahedron with two fluorines is more electronegative and the presence of a second electron-withdrawing group increases the partial positive charge on the central nitrogen. It is a combination of the electron distribution and steric effects that lead to difluoroamine movements being dissimilar to the other distorted tetrahedra, viz. monofluoroamine and ammonia.

The movement of difluoroamine and its landing on lithium hydride occur exclusively via dihydrogen bonding to the surface, with the sole hydrogen pointing towards the hydride ions and the two fluorines parallel to the surface, shown in Figure 3.31. Dihydrogen bonding is the main surface interaction (rather than Li—N bonding) because the opposite charges of $\overset{\delta\ominus}{\text{F}}$ and $\overset{\delta\oplus}{\text{H}}$ in the molecule mean that any shuttlecock up/down configuration will result in

some repulsive interaction with the surface. Fluorine substitution in difluoroamine has altered the stable electronic configuration to the point where the shuttlecock-up orientation is no longer favoured.

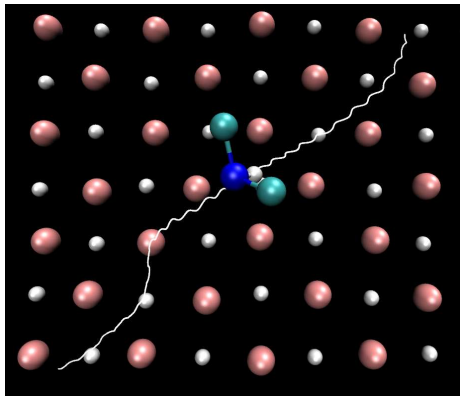

Figure 3.31: Difluoroamine in its preferential configuration on the surface of lithium hydride at 300 K. The lithium are shown in pink, hydrogen in white, nitrogen in blue and fluorine in teal.

3.5 Amide/imide embedded in lithium hydride ($10 < t/ps < 30$)

The experimentally established products for the reaction between ammonia and lithium hydride are hydrogen and lithium amide (see previous eq. 1.6). The predicted mechanism is that molecular hydrogen is formed from a hydrogen dissociated from ammonia and a surface hydride, and that the resultant amide (NH_2^-, from ammonia) fills the newly created hydride vacancy on the surface. Hydrogen formation between ammonia and the lithium hydride surface was not observed on the timescales of the calculations performed in Section 3.4.3 and therefore a hydride on the surface was substituted for an amide initially to evaluate the endpoint of the reaction. This work was extended to an examination of both amide and imide substitution in the bulk structure of lithium hydride, in light of the recent experimental paper by Chen *et al.* where ammonia was produced using lithium hydride + transition-metal composites: ammonia formation was proposed via amide-imide in bulk lithium hydride.[63] An amide and imide group when in the context of lithium amide-imide (rather than organic functional groups), refers to an ammonia with either

one or two hydrogen atoms removed:

$$\underset{\text{(ammonia)}}{NH_3} \xrightarrow{-H^+} \underset{\text{(amide)}}{NH_2^-} \xrightarrow{-H^+} \underset{\text{(imide)}}{NH^{2-}}$$

A hydride can be substituted for either an amide or imide group in lithium hydride, with imide substitution a second hydride has to be removed in order to charge balance the structure.

David and Makepeace's "golf-ball" models of neutron scattering density for lithium imide-lithium amide variable stoichiometry materials[109] inspired the technique used to analyse lithium hydride amide-imide defects *in silico*. The golf-ball model is named from the resemblance that a set of evenly spaced atoms spherically distributed around a central fixed atom has to the dimples found on an actual ball, and was used to sample the orientations of the defects.

To construct a golf-ball of hydrogen positions around a fixed nitrogen atom, Deserno's algorithm was used to generate regularly spaced coordinates that covered an entire sphere.[110] There are many similar algorithms that could have been used to achieve these distributions. The surface of a sphere was well sampled from the equal distribution of 400 points and so used for the hydrogen in the imide calculations. Sampling amide defects is more complex and was accomplished from two separate spheres of equally distributed points; one for each of the two hydrogen atoms. The first hydrogen was obtained from the 400 equidistributed points used for the imide, to ensure that the entire sphere was sampled, and the second from a sphere of 5000 equidistributed points. The second hydrogen atom was randomly selected from the subset of the 5000 points that had the correct amide bond angle of 102°. This resulted in 400 individual imide and amide calculations used to sample the defect orientations.

The respective defects were each embedded in 2×2×2 supercell of lithium hydride, sufficient to isolate the defect from its periodic image over 8 Å away. Additionally, for imide substitutions, the hydride vacancy necessary to balance the charge was positioned as far

away as possible from the imide group. The lattice constant was taken from the geometry optimised lithium hydride without a defect (4.008 Å). A volume expansion due to the exchange of a hydride ion for a larger defect was not included in the model because such a correction would only be valid for the lowest energy orientation, which is intrinsically very small. Single point energy calculations were performed for each orientation in CASTEP using the convergence criteria determined earlier in Section 3.2.2. The spatial arrangement of atoms were not relaxed so that the high energy bond orientations could be sampled and favoured defect orientations were identified from the forces compute on the hydrogen atoms.

The two sets of 400 single point energy calculations are represented by spherical distributions of force from the N—H orientations, shown in Table 3.2. There are 800 N—H orientations for amide given there are two hydrogen per calculation. N—H orientational distributions were the same for the imide and amide defects. The presence of a second hydrogen in amide did not affect the force experienced by the first hydrogen. These distributions are explained by simple electrostatics; the hydrogen in the defect has a partial positive charge because it is bonded to electronegative nitrogen and so disfavours orientations close to positively charged lithium ions. Both ions in the rock-salt structure are held in an octahedral coordination, and thus there are lithium ions located in the ⟨100⟩ and ⟨111⟩ directions from the defect, and hydride ions in the ⟨110⟩ directions (see the ion arrangement around a hydride in Figure 3.1 from Section 3.1). The ⟨100⟩ directions are disfavoured N—H bond orientations due to electrostatic repulsion between particles of the same charge ($\overset{\delta\oplus}{\mathrm{H}}$ and Li^+ ions) and therefore forces on the hydrogen atoms are highest.

⟨110⟩ and ⟨111⟩ directions are favoured because repulsions due to lithium ions along the ⟨100⟩ directions are minimised. The ⟨111⟩ directions are the preferred N—H bond orientations as the furthest positions from the ⟨100⟩ lithium ions. The hydride ions along the ⟨110⟩ directions and lithium ions along the ⟨111⟩ directions are too far from N—H to interact; for this reason forces on the hydrogen are lower along the ⟨111⟩ rather than ⟨110⟩. If the ions were closer to the defect then the ⟨110⟩ directions would be favoured instead, due to electrostatic attraction to the hydrides. A cubic cage structure is formed

by connecting the preferred N—H bond orientations as this avoids the ⟨100⟩ lithium ions, and represents a pathway for defect movement within lithium hydride. In Table 3.2 (c), a cubic cage is plotted from ⅓ of the imide bond orientations (132 of 400) with the lowest force on the hydrogen atoms.

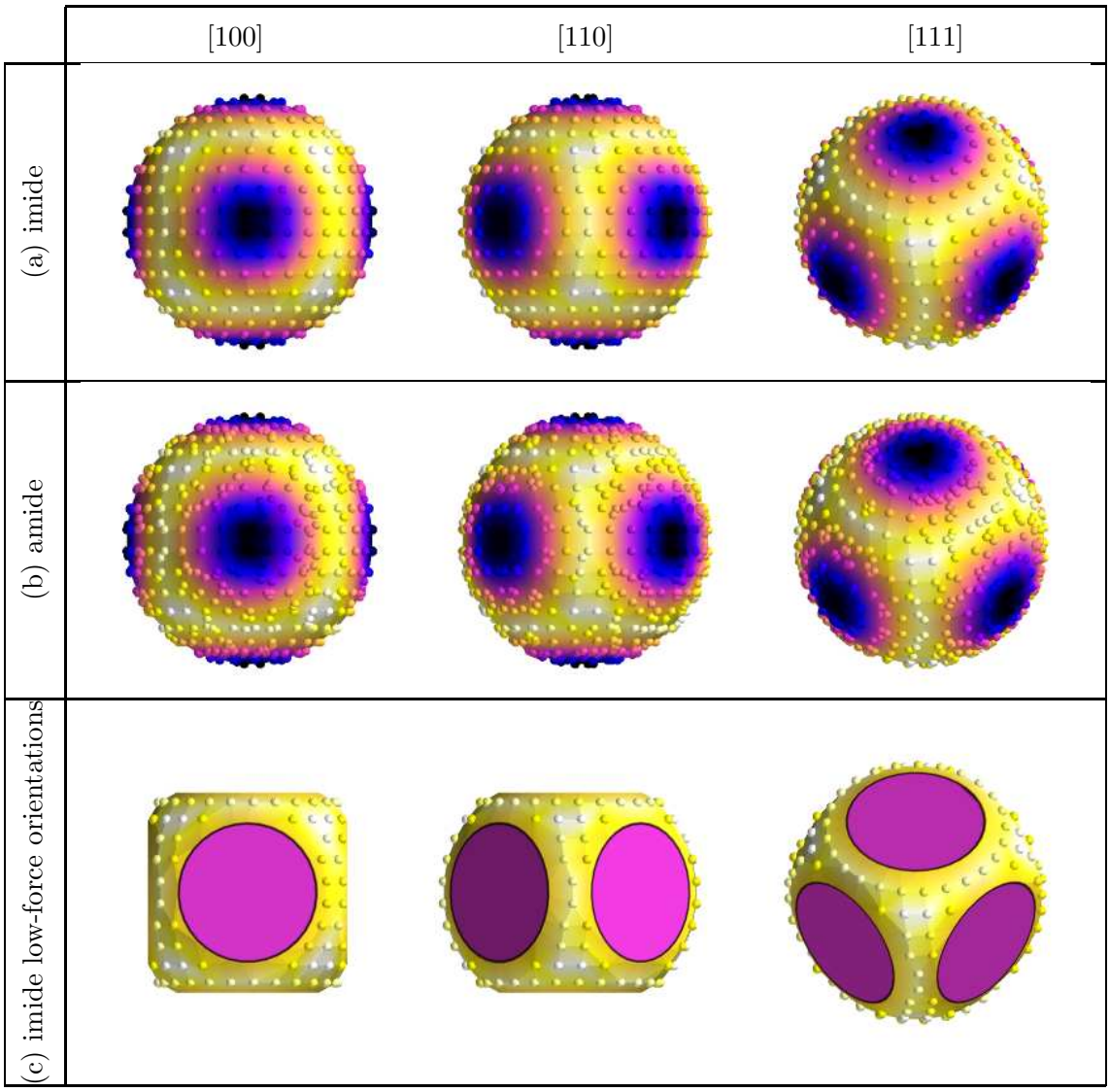

Table 3.2: Force map of N—H bond orientations in (a) imide and (b) amide defects within lithium hydride. N—H orientations with the ⅓ lowest force on the hydrogen atoms from (a) are plotted in (c), magenta circles are plotted on each face of the cube to block out the interior of the structure for clarity. The orientational distributions used to sample the defects are observable from points on the sphere. [100], [110] and [111] crystallographic directions for the defects are shown.

Having established the preferred bond orientations for one N—H, the force maps were used to generate favoured amide orientations containing two N—H separated by 102°. Amide orientations were created by randomly generating a hydrogen position on the surface of a sphere, a circle 102° from N—H was drawn and a second hydrogen position was randomly selected from a point along that circle—alternative to the previously used method. 100,000 random amide orientations were generated. Forces acting on the generated hydrogen positions were estimated by interpolating the calculated values from the three imide hydrogen in Table 3.2 (a) that were closest to the new hydrogen position: the total force on amide was approximated as the sum of the two hydrogen positions. Of the 100,000 randomly generated amide orientations, those with the 5% lowest and 5% highest predicted total force are plotted in Figure 3.32. The cubic cage structure in Table 3.2 (c) was recovered from the low force plot in Figure 3.32 (a), and therefore both of the N—H bonds in the amide defect can be located preferentially along the cage. In the high force plot, the hydrogens are distributed all around the sphere except for the ⟨111⟩ directions; the two hydrogen cannot both be located along disfavoured ⟨100⟩ directions because these are 90° apart and amide is ∼102°.

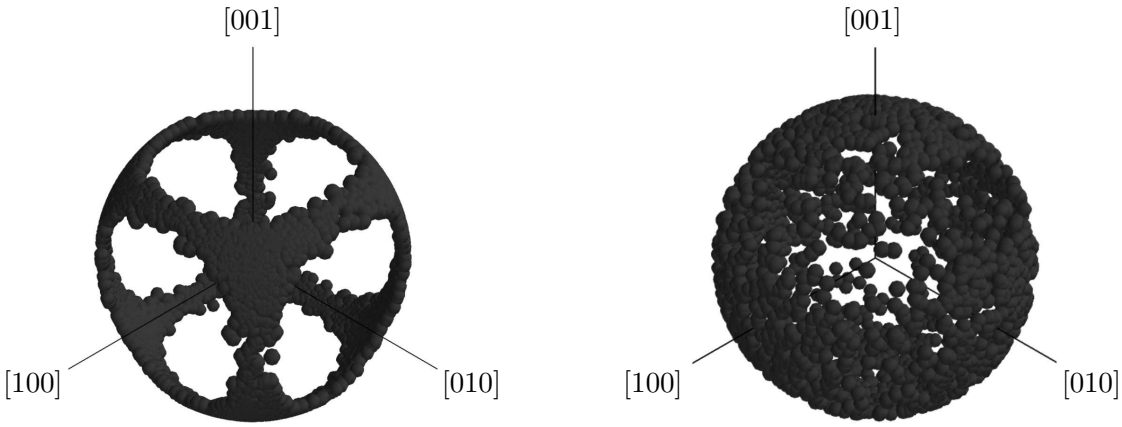

Figure 3.32: N—H bond orientations in theoretical (a) low force and (b) high force arrangements of amide defects within lithium hydride. 5000 amide orientations (so 10000 hydrogen) are shown in both (a) and (b). The orientational distributions are viewed down the [111] direction and an axis is included of the [100], [010], and [001] directions.

Molecular dynamics simulations were performed on an amide defect substituted into lithium hydride both at the surface and a layer beneath the surface, 20 ps of data was collected for both calculations. The lithium hydride slab model used for ammonia on the surface was selected for these simulations because the exchange of a hydride ion for an amide was the assumed endpoint of the original simulation (for modelling details see Section 3.4.1). Three-dimensional spherical histograms were used to represent the distributions of the N—H bond orientations in Table 3.3. In the surface calculation (a), the amide hydrogen were distributed at the four corners which correspond to the locations of the four hydride ions, as these orientations are stabilised by electrostatic interactions. Higher counts were observed at two of the four orientations due to the energetic penalty in changing orientation between the opposite corners—as the hydrogen move across lithium for this transition to occur. As the hydrides surrounding the defect are equivalent, evenly distributed counts would be expected over a longer sampling period. Amide embedded a layer down from the surface (b) exhibited the same cubic cage N—H orientational distribution that was predicted from the static single point energy calculations. The hydrogen are shown from the histogram in Table 3.3 (b) to mostly be distributed at $\langle 111 \rangle$ directions followed secondly by $\langle 110 \rangle$, in agreement with the forces on the hydrogen in Table 3.2. The amide defect mostly sampled 2 of the 8 $\langle 111 \rangle$ directions and this was attributed to the energetic penalty from changing the orientation between the corners of the cage. Evenly distributed counts for the amide embedded a layer beneath the surface would not be expected because the surface layer in the dynamic calculation can expand into the vacuum to accommodate the defect—and therefore those $\langle 111 \rangle$ directions are favoured. This combined computational approach, using forces from static calculations and histogram counts from dynamic calculations, confirms that the cubic cage structure is the preferred pathway for amide-imide defect movement within lithium hydride.

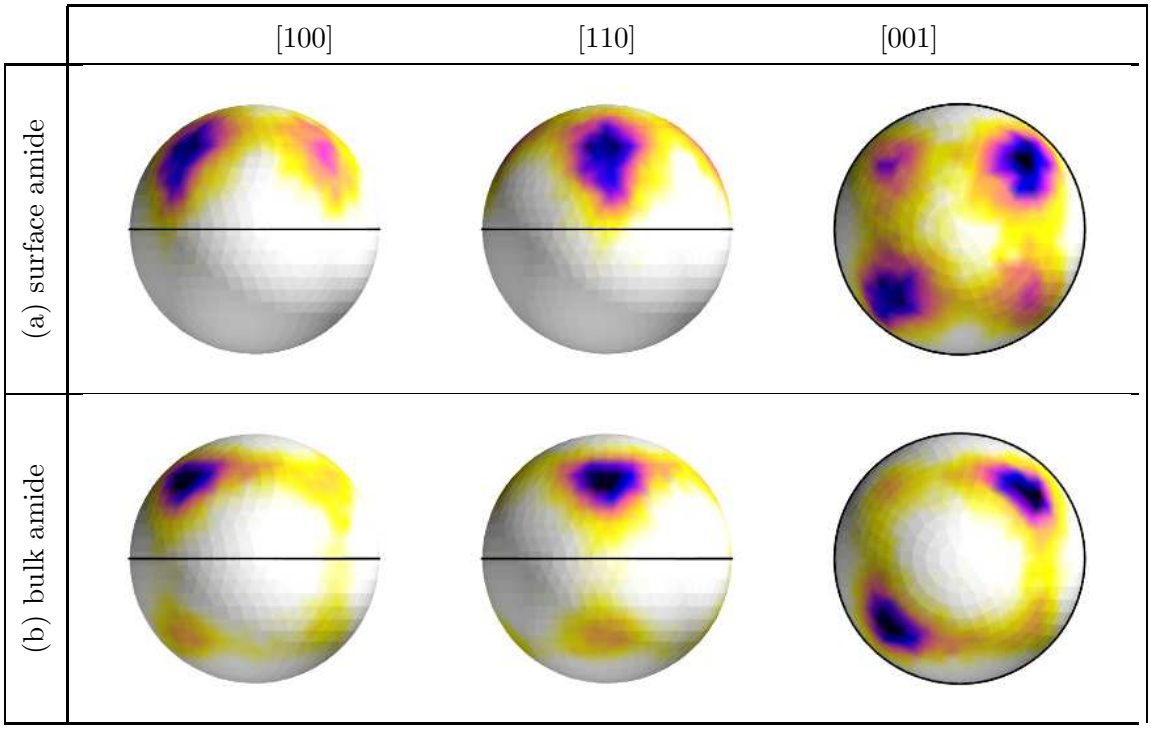

Table 3.3: Spherical histograms for the N—H bond orientations of amide embedded (a) on the surface and (b) in the bulk of lithium hydride at 300 K. The equator in (a) is used to represent the approximate surface. 1000 histogram bins.

3.6 Conclusions

In this Chapter, the interactions of ammonia on lithium hydride were investigated from a surface slab model which is a more accurate representation of LiH than the previous published molecular or cluster models.[39, 40, 41] The well-known phenomenon of surface rumpling of the (100) rock-salt surface was observed in LiH, and this defining physical property was used to evaluate the surface reconstructions. This led to a short investigation of alkali-metal hydrides where the size of the metal relative to the hydride was observed to affect the direction of the rumpling: a transition from positive to negative rumpling was found descending group I and the largest metals did not move significantly.

The molecular trajectories analysed on the surface of lithium hydride were representative of the calculations as a whole: for ammonia, these interactions were observed from repeated

runs, and for molecules structurally related to ammonia, from a combination of one and two molecules on the surface of lithium hydride. A complete list of all the calculations performed as part of this thesis is tabulated in Appendix C. The interaction of NH_3 on the LiH surface was shown to be closely related to its distorted tetrahedral shape from simple electrostatics arguments, in both the straight-line, dihydrogen bonded movement of ammonia across Li^+ ions on the surface and its stable shuttlecock-up configuration. It is this tetrahedral structure that stabilises the shuttlecock-up arrangement by the formation of three points of contact to the surface. The addition of a second ammonia molecule introduced intermolecular hydrogen bonding that resulted in the two molecules propagating as a dimer along the surface. The conclusions that the ammonia was trapped on the surface by its tetrahedral shape and interacted via the formation of temporary dihydrogen bonds can be applied to future computational studies of Li–N–H systems—as these interactions were consistent with the existing literature based on LiH molecules and clusters, where ammonia bonded shuttlecock-up.[39, 40, 41] The study was extended to molecules on the surface with tetrahedral geometries closely related to ammonia. Methane, as a non-polar molecule without a lone pair of electrons, was repelled from lithium hydride. Water which has a polarity comparable to ammonia was not stabilised on the surface, due to the absence of a third hydrogen atom. The bent geometry of water instead forms two points of contact with the surface and is able to freely rotate, and consequently water bonds only temporarily. Fluorine substitutions in ammonia were used to alter the electronic distributions within the distorted tetrahedral structures and this increased the reactivity. Trifluoroamine was so reactive that it immediately dissociated upon contact with the surface. The tetrahedral structure of monofluoroamine was lopsided towards the N—F bond, both physically and electronically with its dipole moment towards the fluorine atom. The surface interaction of monofluoroamine was dominated by the electrostatic attraction of the fluorine to lithium ions, as steric hinderence restricted the formation of dihydrodgen bonds. The shuttlecock-up orientation was observed temporarily because it positioned the fluorine close enough to react on the surface; this resulted in the formation of ammonia that proceeded to orbit shuttlecock-up and a fluorine atom which was substituted into the newly created hydride vacancy. In difluoroamine, the fluorines altered the stable

electronic configuration to the extent that dihydrogen bonding was the main surface interaction, and the shuttlecock-up landing configuration was repulsive as a consequence of the opposite charges of $\overset{\delta\ominus}{\mathrm{F}}$ and $\overset{\delta\oplus}{\mathrm{H}}$. Amide and imide substitutions were investigated in LiH using golf-ball models of forces and molecular dynamics. From both techniques, a cubic cage structure was formed from the favoured N—H bond orientations as the hydrogens avoided the lithium ions along the $\langle 111 \rangle$ directions.

4

Detailed computational analysis of the crystal structure of lithium imide

4.1 Introduction

There are two known phases of lithium imide that are related to each other by an order-disorder phase transition at 356 K. This transition was first identified by Forman from differential thermal analysis in 1971 and was attributed to the disordering of the NH^{2-} ions by analogy with known structures.[111] The lithium imide structure has been subject to much debate in the literature, with a resurgence of interest in the first decade of the 21st century due to its potential application as a hydrogen storage material.[25, 32, 34, 53]

The high-temperature phase ($\geq$ 356K) adopts a disordered undistorted antifluorite crystal structure with space group symmetry $Fm\bar{3}m$. This structure was solved experimentally by

neutron and X-ray diffraction,[54, 55] and analysed computationally by *ab initio* molecular dynamics simulations.[112] Imide groups (NH^{2-}) are organised in a face-centred cubic arrangement with $2\,Li^+$ along each of the body diagonals in the unit cell, at 1/4 and 3/4 the length of the diagonal, shown in Figure 4.1(a). This arrangement leads to Li^+ adopting a tetrahedral coordination and NH^{2-} in an undistorted cube coordination. The two different coordination environments have been highlighted in Figure 4.1(a, b): ions outside of the unit cell are included so that both environments can be viewed simultaneously. There are eight nitrogen tetrahedra located at the corners of the unit cell, these edge-share and together form an unoccupied octahedral site at the centre of the unit cell. This octahedral site is shown in (c) with the vertices of the octahedron connected. The hydrogen sites around nitrogen were assigned in earlier experimental work by Noritake *et al.* to the $48\,h$ positions and by Ohoyama *et al.* to the $16\,e$ positions with ¼ hydrogen site occupancy (which changes the space group to $F\bar{4}3m$).[113, 114] The disordered hydrogen were subsequently best fit to the $192\,l$ sites in the $Fm\bar{3}m$ phase, shown in (d).[54, 112]

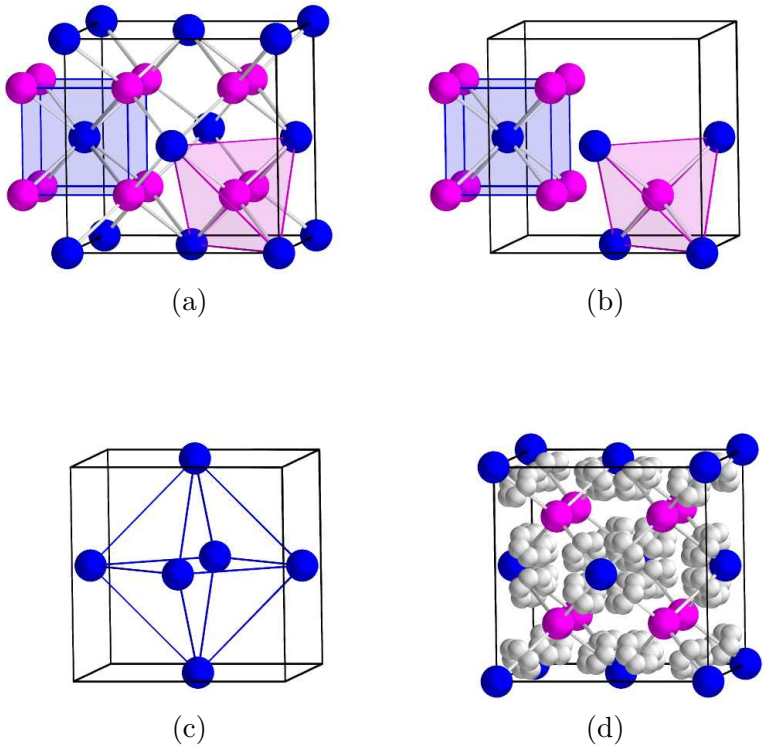

Figure 4.1: Li_2NH high-temperature $Fm\bar{3}m$ structure. Lithium are shown in magenta, nitrogen in blue and hydrogen in white. (a) Unit cell with ion coordination highlighted, (b) ion coordination, (c) vacant octahedral site with vertices connected and (d) disordered hydrogen.

At temperatures below 356 K the underlying face-centered cubic arrangement of NH^{2-} found in the high-temperature phase remains, and therefore the structural considerations relate to changes in the Li^+ positions and ordering of the N—H bond orientations. A number of models have been proposed for the low-temperature phase. The earliest structural work was Balogh's diffraction data between 100–300 K which were best fitted to the $Fd\bar{3}m$ space group.[54] The $Fd\bar{3}m$ space group can be viewed as a superstructure of $Fm\bar{3}m$ (with a $2 \times 2 \times 2$ supercell) where one in eight Li^+ ions are displaced into partially occupied interstitial octahedral sites (i.e. Li^+ occupying the vacancy in Figure 4.1(c)). In the absence of a lithium ion, the imide groups around the unoccupied Li^+ site re-orientate towards the vacancy along the $\langle 111 \rangle$ directions. Subsequently a number of computational studies have debated the fully ordered structural model of this low-temperature phase.[55, 56, 57]

All show N—H ordering around vacant Li^+ sites and octahedral Li^+ interstitials. The differences are about how these features are arranged in the structure.

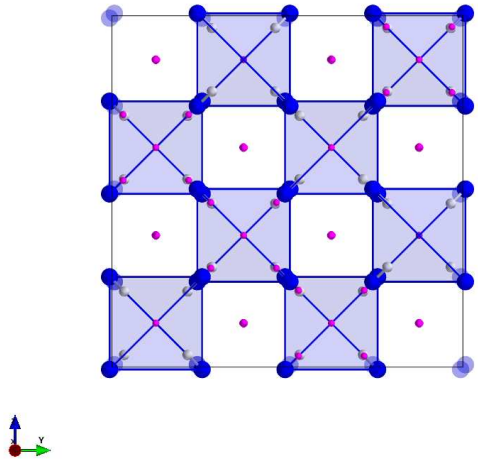

(a)

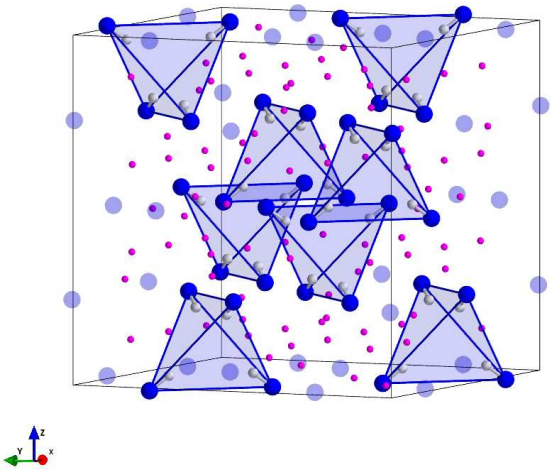

(b)

Figure 4.2: Li_2NH low-temperature $Fd\bar{3}m$ structure with the vacant tetrahedra highlighted. Lithium are shown in magenta, nitrogen in blue and hydrogen in white.

Table 4.1: Li_2NH reported space groups and unit cell parameters. † Calculated phases.

Space group	a, b, c (Å)	Coordinate transformation matrix from $Fm\bar{3}m$	Shift of origin from $Fm\bar{3}m$	Ref.
$Fm\bar{3}m$	5.0918(1)	$\begin{pmatrix} 1 & 0 & 0 \\ 0 & 1 & 0 \\ 0 & 0 & 1 \end{pmatrix}$	$\begin{pmatrix} 0 & 0 & 0 \end{pmatrix}$	54
$F\bar{4}3m$	5.0769(1)	$\begin{pmatrix} 1 & 0 & 0 \\ 0 & 1 & 0 \\ 0 & 0 & 1 \end{pmatrix}$	$\begin{pmatrix} 0 & 0 & 0 \end{pmatrix}$	114
$Fd\bar{3}m$	10.12971(7)	$\begin{pmatrix} 2 & 0 & 0 \\ 0 & 2 & 0 \\ 0 & 0 & 2 \end{pmatrix}$	$\begin{pmatrix} 0 & 0 & 0 \end{pmatrix}$	54
$Ima2$ †	7.133, 10.087, 7.133	$\begin{pmatrix} 1 & 0 & 1 \\ 0 & 2 & 0 \\ 1 & 0 & -1 \end{pmatrix}$	$\begin{pmatrix} 1/4 & 0 & 1/4 \end{pmatrix}$	55
$Imm2$ †	3.588, 5.0742, 3.588	$\begin{pmatrix} 1/2 & 0 & 1/2 \\ 0 & 1 & 0 \\ 1/2 & 0 & -1/2 \end{pmatrix}$	$\begin{pmatrix} 1/4 & 0 & 1/4 \end{pmatrix}$	54

4.2 Chapter Overview

In this chapter, the structure and dynamics of bulk lithium imide were investigated between 300–700 K. The simulation cell was heated from 300 K to 700 K in 100 K steps, with structures evaluated at each temperature. This sequence was followed by a simulated rapid cooling from 700 K to 300 K in 5 K steps per 0.1 ps. At the beginning of the simulation an ordered low-temperature phase was observed which was followed by an order-disorder phase transition around 500 K during heating. Figure 4.3 illustrates this phase transition from the perspective of lithium orientations around the nitrogen—the lithium distribution is illustrated from two directions to give a clear indication of the computed lithium den-

sity around the complete orientation sphere. The subsequent rapid cooling of the 700 K structure back to 300 K resulted in a different low-temperature phase being recovered.

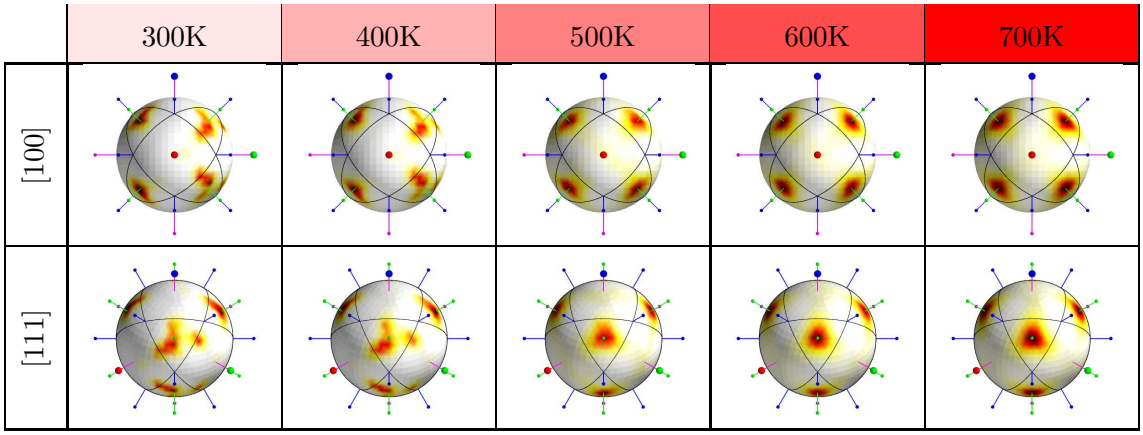

Figure 4.3: Summary of the lithium orientation distribution around nitrogen on heating from 300 K to 700 K. Crystal axes $+a$, $+b$ and $+c$ are represented by (1,0,0) in red, (0,1,0) in green and (0,0,1) in blue respectively. Graph labels are fully described in Figure 4.14.

4.3 Modelling details

The lithium imide structure was investigated by *ab initio* molecular dynamics of a 128 atom supercell constructed from $2 \times 2 \times 2$ $Fm\bar{3}m$ unit cells. A $2 \times 2 \times 2$ supercell was selected as the minimum cell size required to reconstruct the low-temperature phase, and the high-temperature phase was used as the initial structure to avoid biasing the simulation towards any one lower symmetry space group which may have resulted in the atoms becoming trapped in their ordered initial configuration. The lattice parameter was taken to be 5.09 Å from the experimental structure in Table 4.1—the precise value is however less important for NPT given that the simulation cell changes during computation. The structure contains 64 edge-sharing $Li(NH)_4$ tetrahedra, where clusters of 8 tetrahedra form an empty octahedral site. These octahedra are face-sharing with the tetrahedra and therefore 4 octahedra surround each tetrahedron. The 64 lithium ions each start inside a tetrahedron and the octahedra are unoccupied. The $Fm\bar{3}m$ structure has been described in terms of partially occupied 192 l hydrogen sites around each nitrogen. This is a convenient but fictitious assignment and therefore hydrogen were initially randomly assigned to one

of these sites at each nitrogen. The high symmetry was immediately lost at 300 K. The [100] projection of the initial structure is illustrated in Figure 4.4; the numbering scheme used to identify polyhedra in the Chapter is shown along the a and c axes. Together with the b axis, a unique three number index is obtained (a, b, c). Tetrahedra are located at triplets containing all odd numbers (shown from the lithium starting positions in the figure) and octahedra are at even number triplets. The indexes run from 0–7 and conforms to periodicity of the simulation cell. The connectivity of all the polyhedra are tabulated in Appendices B.1 and B.2. On heating to 700 K the underlying face-centred arrangement of nitrogen remains topologically unchanged which enables the index triplets to be used to trace lithium motion through the structure.

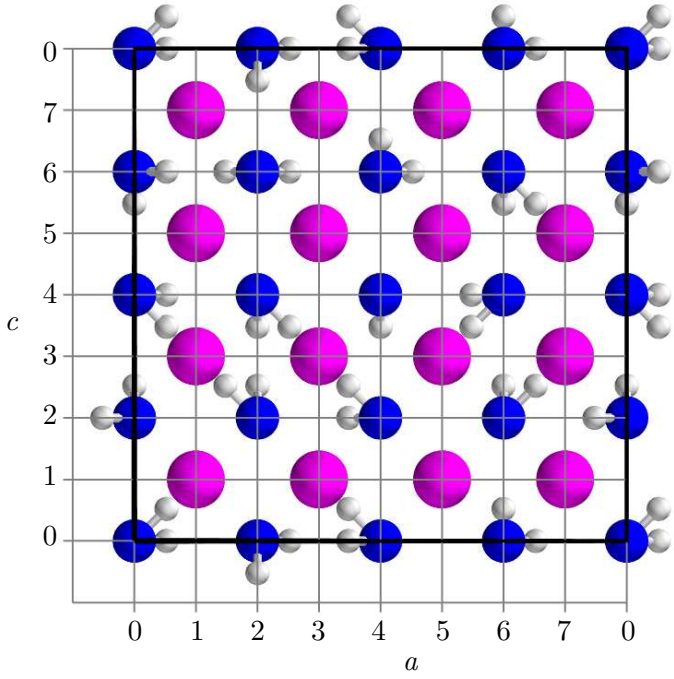

Figure 4.4: [100] projection of the initial lithium imide configuration used in the simulation. The simulation cell boundaries are shaded and a grid for indexing the polyhedra is overlaid along the a and c axes. Lithium are in magenta, nitrogen in blue and hydrogen in white.

The theoretical foundations for these calculations are described in Chapter 2. Lithium imide was modelled by *ab initio* molecular dynamics as implemented in the CP2K pack-

age.[93] The QUICKSTEP method in CP2K was utilised and, a Gaussian and plane wave approach that leverages a dual basis set was implemented to reduce the overall computational costs.[85] The calculation parameters previously determined for Li–N–H systems in Section 3.4.1 were used for Li_2NH, with a plane wave cut-off energy of 320 Ry and double-zeta Gaussian basis set.

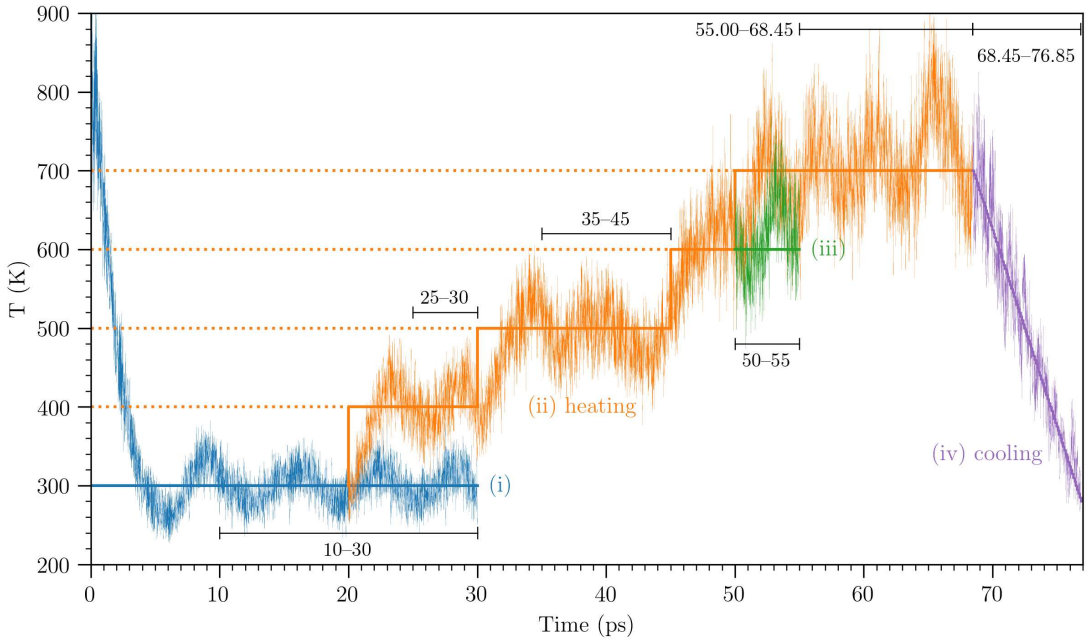

Figure 4.5: Computationally evaluated temperature of Li_2NH heated from 300–700 K and subsequently cooled to 300 K. Colours correspond to different sections in the simulation: (i) initial equilibration and 300 K, (ii) heating from 300–700 K, (iii) supplementary 600 K and (iv) cooling rapidly from 700–300 K. The thermostat target temperature is shown throughout and coloured according to the section. Production runs (data collection) with their corresponding times are given by black lines with vertical bars at either end.

The temperature profile throughout the simulation is shown in Figure 4.5; this serves a dual purpose by both describing the temperature oscillations and also establishing a record of the overall data collection process. The simulation temperatures are given along with the thermostat target temperature. The structure was heated from 300 K to 700 K in 100 K steps, with data collection at each temperature and then rapidly cooled to 300 K

in 5 K steps per 0.1 ps, which is equivalent to a 100 K change in a mere 2 ps. At the beginning of the simulation, (i) a temperature excursion is observed that corresponds to the system being unequilibrated, and this excursion has been enhanced by starting the structure in the high-temperature phase. The temperature is however under control from ∼3 ps. Temperature oscillations in the thermostat are reasonable for the equilibrated system, given that the simulation cell is small containing 128 atoms.

The figure includes branches at 20 ps and 50 ps which correspond to additional runs that were collected after the initial heating (ii). The simulations were restarted at those points using calculation checkpoints from the initial run. Production runs at each temperature are shown by lines with vertical bars at either end, the 300 K data set (i) includes the initial run (10 ps–20 ps) and the supplementary timesteps (20 ps–30 ps) collected afterwards. Time frames outside of these runs correspond to equilibration periods. Given that the starting low-temperature structure was based on a supercell of the cubic high-temperature lattice, a longer initial equilibration period of 10 ps was used to account for rearrangement of the initial structure. Shorter equilibration periods of 5 ps were subsequently used with each 100 K increase, which enabled enough time for the system to re-equilibrate to the new temperature and allow for any significant structural changes. Equilibration at 600 K and 700 K were ran consecutively between 45–55 ps because a production run at 600 K was not originally planned, however this temperature was retrospectively collected (iii).

The cooling period (iv) was treated as a single production run because the initial structure was well equilibrated and the 5 K temperature drops were too small to merit individual equilibration. Fewer timesteps were collected in cooling compared to heating because the purpose of this calculation run was to recover the 300 K phase, rather than to evaluate disordered structures (period between 700–500 K)

4.4 Low-temperature Frenkel defect formation

In order to properly evaluate the low-temperature phase, the effect that the initial temperature excursion had on the structure was first assessed. The initial high temperature

meant that all atoms had significant thermal motion and the lithium in particular had sufficient energy to migrate through the structure at the beginning of the 300 K run (0–1.8 ps). Migration promptly stopped once the temperature was under control and did not significantly reoccur until 500 K. The nitrogen polyhedra in Li_2NH can accommodate only one lithium due to their small internal volume and the repulsion between two same-charge ions. Therefore lithium migration between polyhedra must be accompanied by a knock-on / cascade effect from correlated lithium movements. Lithium ions can only migrate between tetrahedron and octahedron. During the initial temperature excursion, a single lithium ion moved to occupy an octahedral site resulting in a vacant tetrahedron elsewhere in the structure. Lithium hopping, therefore, results in a Frenkel defect with Li^+ moving to an interstitial site. This defect formed initially at high-temperature became trapped at the beginning of the simulation run.

All lithium ion migrations during the cooling at the start of the 300 K run are recorded using their polyhedron locations within the structure, as shown in Figure 4.6. A migration is recognized when lithium either moves tetrahedron-to-tetrahedron (via an octahedron) or remains for at least 1 ps inside an octahedron. These criteria are used to avoid logging cases where a lithium occupying a tetrahedron temporarily enters a face-sharing octahedron and then returns to its tetrahedron. This vibration across the tetrahedral/octahedral face frequently occurs and does not represent a genuine migration through the structure. Almost all migration occurs before 1.8 ps and therefore are at high-temperature (1.8 ps corresponds to 515.75 K in the temperature decline). All lithiums begin and end in tetrahedra with the exception of the single defect.

In Figure 4.6, the red, pink and grey series are examples where lithium ions have moved through the structure and returned to their starting tetrahedron. The green and orange series result in the exchange of lithium, as the lithium that starts in T755 ends in T757, and vice versa. Blue, brown and purple series are connected with the lithium in T355 moving to T357, T357 to T555, and T555 to T355. The occupied octahedron trapped in the low-temperature structure was originally formed at 1.13 ps (618.5 K), when lithium moved from T571 to O688 in the cyan series. This created a tetrahedral vacancy (T571)

which was subsequently reoccupied at 1.53 ps (585.1 K) by the lithium that started in T371—from the yellow series. This resulted in the Frenkel defect pair T371 and O688.

A break in the x-axis has been inserted because no migrations were observed from 1.79 ps until 11.01 ps (315.8 K) during the production run. Lithium migration restarted with lithium from the yellow series moving T571 to O662. Whilst O662 was occupied, lithium moved from T551 to O648 (black series) and O688 to T571 (cyan series). Lithium in the cyan series had therefore returned to its initial tetrahedron. The return pathway for the O648 defect was cut off by lithium in the yellow series moving from O662 to T551. The last lithium migration at 300 K occurred at 11.48 ps with the yellow series. There were no migrations in the final 18 ps of the production run. These coloured series are combined into two chains of correlated lithium motion: the cyan, yellow and black series that formed the defect are connected and all other coloured series except the grey are connected (the grey series is an isolated movement). In summary, the original defect, formed at high temperature in a single occupied octahedron, was relocated in the structure at low temperature (average 300 K); the tetrahedral vacancy (T371) that formed as part of the defect was not reoccupied.

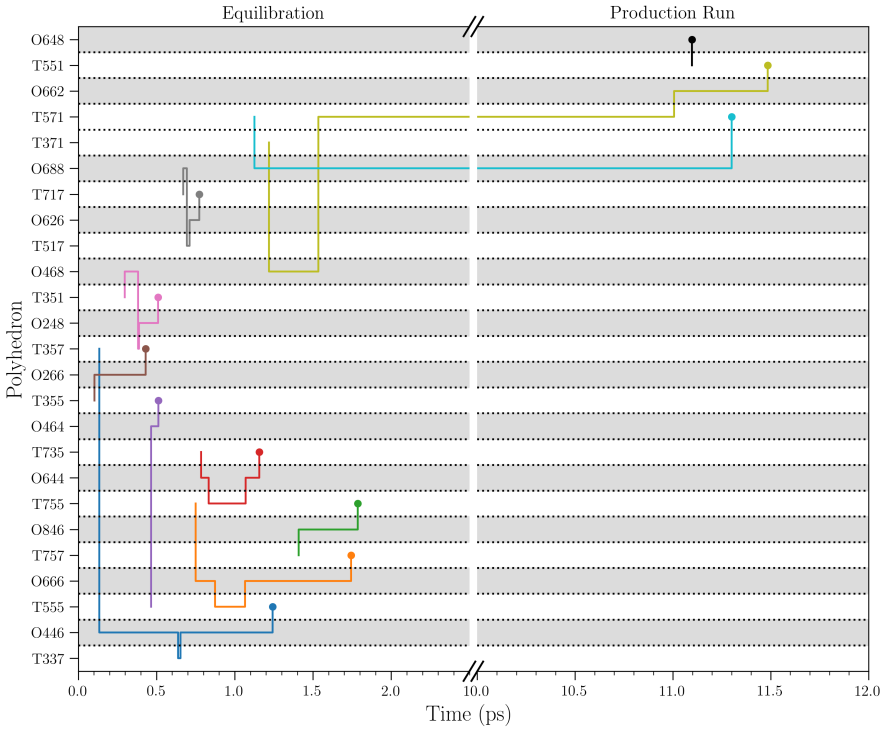

Figure 4.6: Lithium migration in Li_2NH at 300 K; the time frame encompasses both the equilibration and production run. Coloured lines refer to different lithium ions with their final location marked by a point. Polyhedra are assigned either T or O followed by a unique three number index for their location within Li_2NH. Grey regions correspond to octahedra and white regions tetrahedra.

Lithium ions from Figure 4.6 that were involved in the defect formation have their trajectories plotted in Figure 4.7 to illustrate the defect formation pathway through the structure. The lithium, its trajectory and the starting tetrahedron are all coloured the same as the series in the Figure 4.6. This figure is separated into lithium ion migrations (a) before and (b) after the system had reached a state of equilibration. A third set of trajectories, (c), shows lithium ions in the last picosecond of the production run together with their initial tetrahedron, to illustrate how far the lithium had moved. An imide group was periodically adjusted in Figure 4.7 (a) along the b-axis in order to fully construct the octahedron. The previous descriptions of the cyan, yellow and black chains in the schematic are the same for the trajectories.

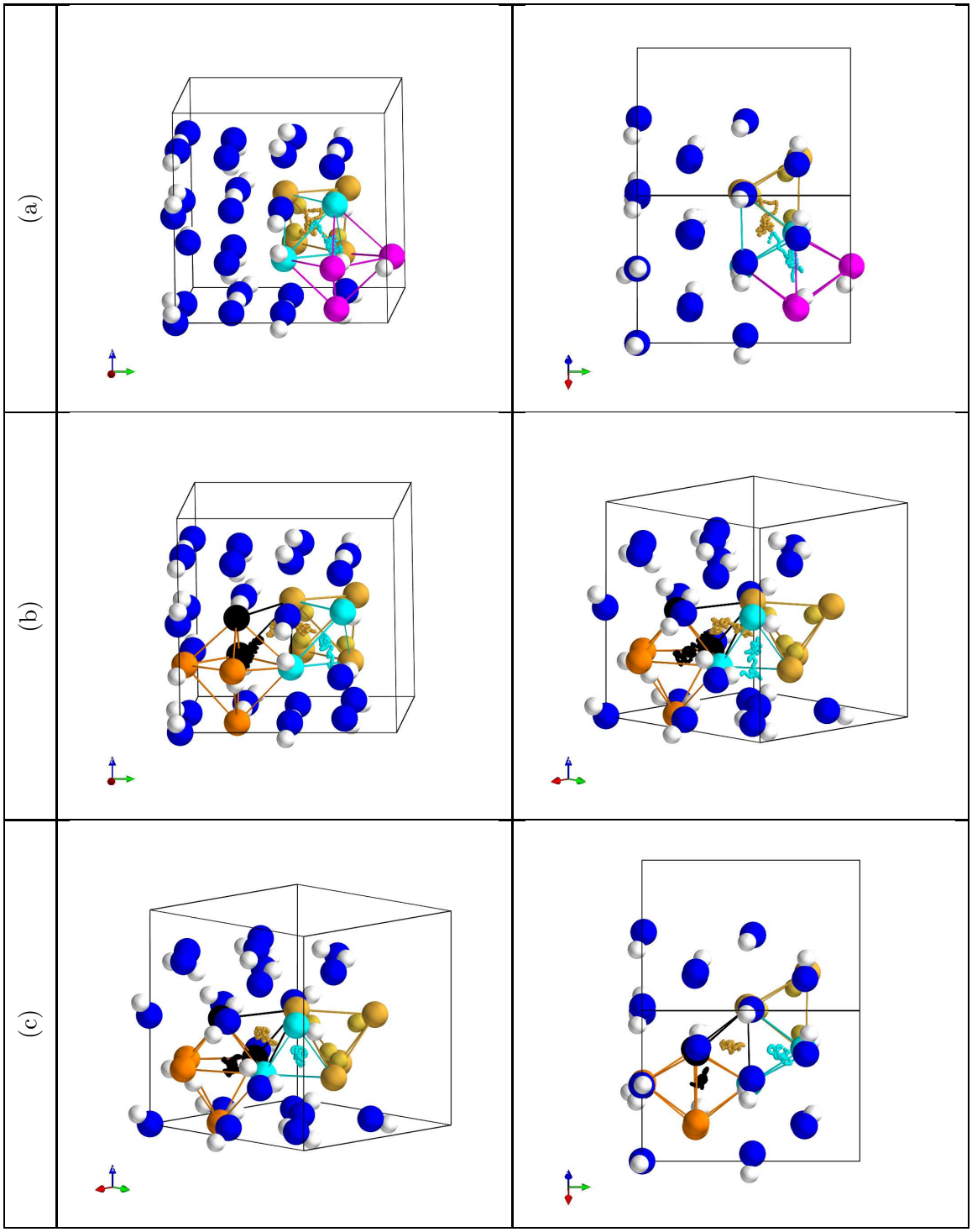

Figure 4.7: Trajectories for lithium migration associated with the defect formation in Li_2NH at 300 K: (a) before equilibration, 1–2 ps, (b) after equilibration, 10.5–12 ps and (c) 29–30 ps. Lithium trajectories are plotted every 0.01 ps. The average imide positions are used for the structure. Polyhedra traversed by the lithium trajectories have their vertices connected.

In addition to migrations which were defined as > 1 ps, shorter lithium oscillations back and forth between face-sharing tetrahedron and octahedron are observed at 300 K. An example of this is shown in Figure 4.8 where a lithium ion oscillates between T351 and O442; the polyhedra locations for the complete set of 64 lithium ions at 300 K are listed in Appendices B.3 and B.4. These oscillations are a consequence of the small internal volume of the tetrahedra which means lithium ions are likely to be close to one of the four tetrahedral faces. This is discussed further in Section 4.5.

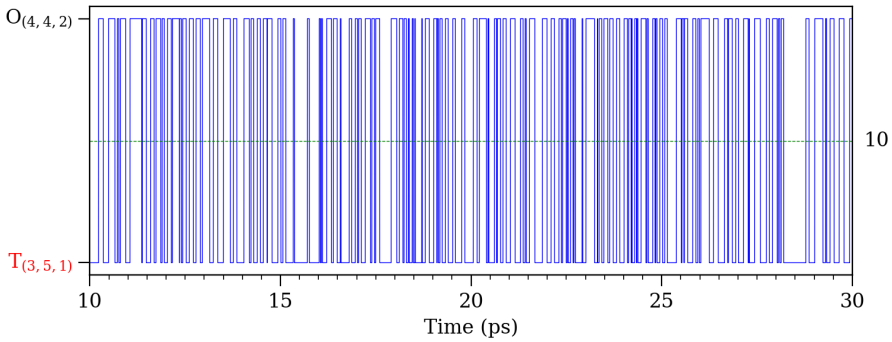

Figure 4.8: Lithium oscillation over 20 ps between a face-sharing tetrahedron and octahedron at 300 K.

At the end of initial cooling, the single Frenkel defect (T371, O688) remains in the structure. The vacant tetrahedron, T371, is replotted without the rest of the structure in Figure 4.9. The absence of a positive lithium is compensated by the $\overset{\delta\oplus}{\mathrm{H}}$ ions pointing into the tetrahedron, which is consistent with experimental observations.[54] On average, all four imide bonds point into the tetrahedron, imide bonds (A) and (B) point directly at the cation vacancy, along $\langle 111 \rangle$ directions while imide bonds (C) and (D) point towards opposite tetrahedral faces while remaining inside the tetrahedron. The simultaneous occurrence of a minority of Li^+ in octahedra and tetrahedral N—H order are the key features of all predicted low-temperature structures.

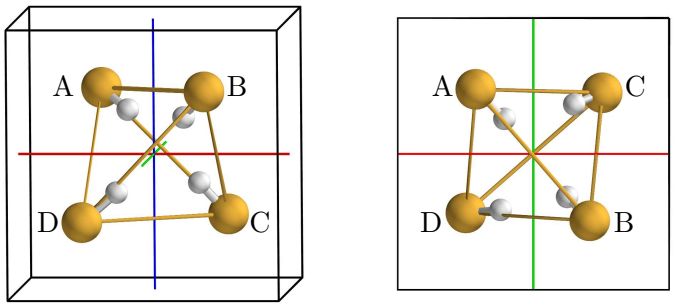

(a) (b)

Figure 4.9: Average imide positions of vacant tetrahedron T371 after equilibration at 300 K. An arbitrary box is constructed around the defect to orientate the images with respect to one another, with interior x, y and z-axes in red, green and blue respectively. Nitrogens are in yellow and hydrogens in white.

A Mercator projection for the N—H bond orientations of all 32 imide groups is shown in Figure 4.11 to evaluate the defect imide bonds in more detail; data points are shown every 10 fs to avoid over-plotting. Well-known limitations of this familiar projection method are included for reference in Appendix B.5. Ensemble averaged H positions around the N atom at the centre of the projected sphere are plotted in red with triangle markers for the 4 defect imides to set them apart from the other imides in the structure. Miller indices, polyhedron faces and face-boundries are included on the diagram: these elements are explained in Figure 4.10 which will be referred back to throughout the text. Additionally, the imides in the Frenkel defect are highlighted in yellow to coincide with the previous figure, and the four separate regions observed in Figure 4.11 correspond to the four individual imides.

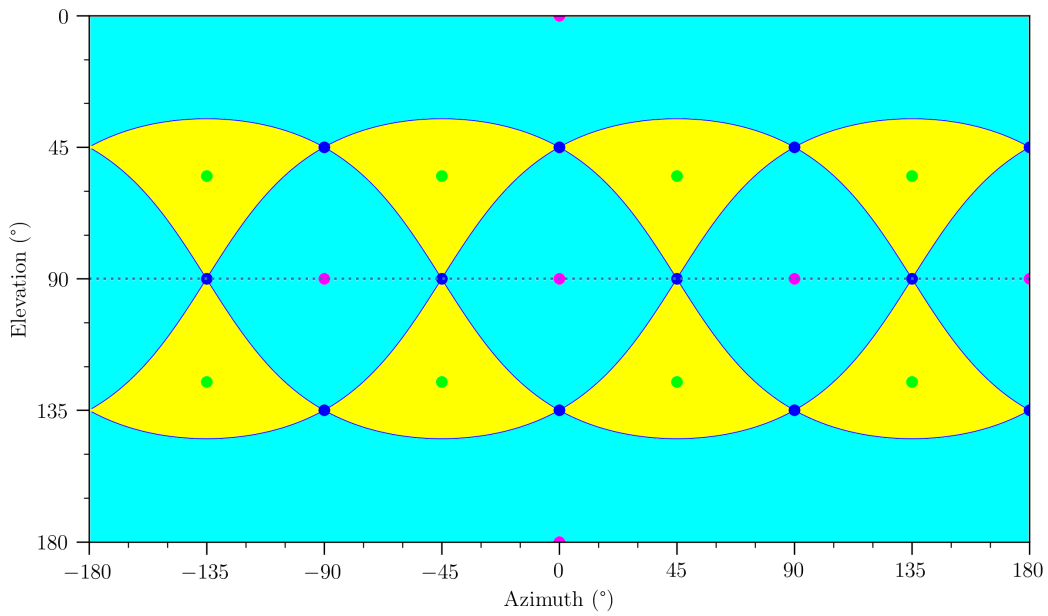

Figure 4.10: Mercator projection of polyhedral faces around the nitrogen. ⟨100⟩, ⟨110⟩ and ⟨111⟩ families of directions are plotted in magenta, dark blue and green respectively. Polyhedral faces are shown in yellow for tetrahedron and cyan for octahedron. Lines that connect the ⟨110⟩ directions correspond to the tetrahedron to octahedron face-boundaries.

In Figure 4.11, three of the four defect imides are orientated around ⟨111⟩ directions that correspond to the centre of the tetrahedron ($[1\bar{1}\bar{1}]$, $[1\bar{1}\bar{1}]$ and $[\bar{1}1\bar{1}]$). The distributions around $[1\bar{1}\bar{1}]$ and $[\bar{1}1\bar{1}]$ have ensemble average orientations close to being directly along the ⟨111⟩ , while the distributions around $[1\bar{1}\bar{1}]$ are on average between the $[1\bar{1}\bar{1}]$ and $[\bar{1}01]$. The fourth defect imide was not orientated around a ⟨111⟩ direction but instead located on average at the tetrahedron-to-octahedron face-boundary, near to the [101]. Imides from the vacant tetrahedron clearly re-orientate to restore the local positive charge lost by lithium ion migration, as significant distributions around the ⟨111⟩ directions are not observed for the other 28 imides in the figure. The Mercator projection however indicates that a complete set of $4\,H^+$ may not be strictly necessarily to restore the local positive charge vacancy, as $1\,H^+$ is observed along the face-boundary. The 4 N—H associated with

the defect orientate towards the interior of the vacant tetrahedra, in agreement with the literature.[54, 55, 56, 57] However, other orientations are clearly favoured for the remaining 28 imides and these will be discussed in Section 4.5.

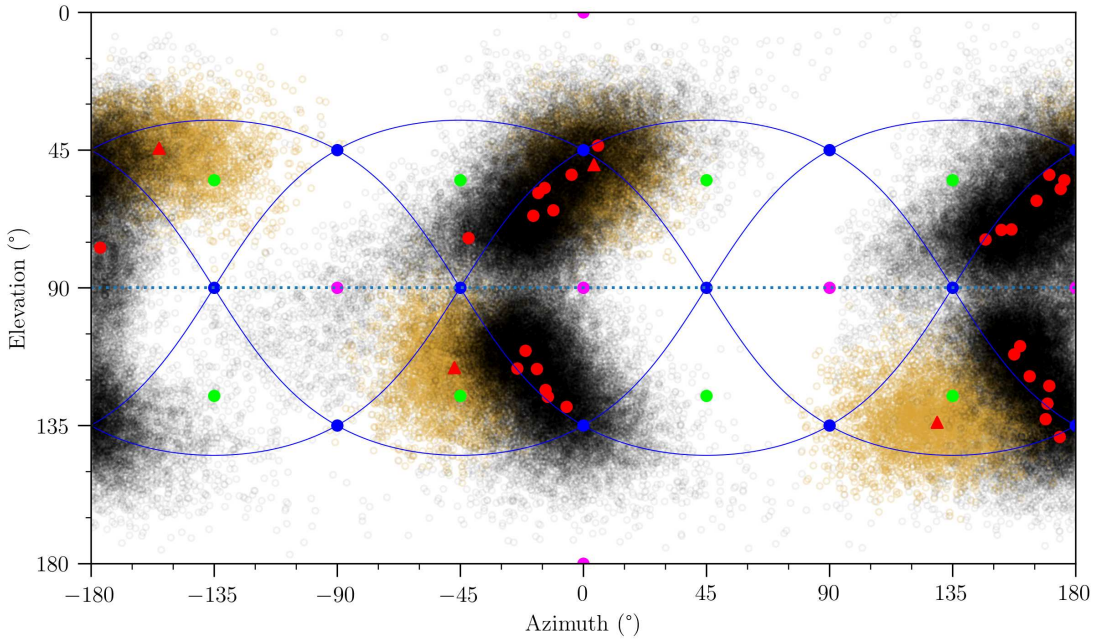

Figure 4.11: Mercator projection for the orientations of 32 H^+ around N in the Li_2NH supercell, after equilibration at 300 K. Imide orientations are displayed in black except for those from the vacant tetrahedron (T371) which are in yellow: plotted every 10 fs (64,000 orientations in total). Ensemble average positions of the 32 imides are shown in red, with △ for the four imides associated with the defect and ○ for the other 28. Graph labels are fully described in Figure 4.10.

The $Ima2$, $Imm2$ and $Fd\bar{3}m$ low-temperature structures that were previously reported for lithium imide all contained multiple Frenkel defects with lithium displaced from tetrahedra into octahedra. These are consistent with the defect observed in this simulation. This defect, however, does not replicate the defect arrangements found in the $Ima2$, $Imm2$ or $Fd\bar{3}m$ structures. The fact the defect was singular may however have been an artifact of the small simulation cell, given that the two defect polyhedra were as far apart as possible within the structure (see Figure 4.7 (c)). This suggests that the simulation cell may have

been too small to host multiple defects. The lithium imide supercell with 128 atoms should in theory have been able to accommodate lithium occupancies in $^4/_{32}$ octahedra, as in the reported low-temperature structures. However in practice, the spatial requirement for multiple lithium migration chains could have feasibly exceeded this. The low-temperature structure recovered therefore likely represents a slightly frustrated structure which is a favourable configuration in the absence of being able to form a much larger network of tetrahedral defects.

4.5 Structural analysis of the low-temperature phase

Having established that the structure contained a single lithium defect and traced its formation back to the high-temperature excursion during the initial equilibration period, the symmetry in the low-temperature phase was evaluated. The crystal system was first inspected from the cell parameters and volume in Figure 4.13. The initial structure was a $2 \times 2 \times 2$ cubic supercell with a length of 10.18 Å. This high-symmetry structure was immediately lost during the equilibration period, with a volume expansion (a) coinciding with the high-temperature excursion in Figure 4.5. The volume, disregarding the unequilibrated thermal expansion, had increased from 1055 $Å^3$ in the starting high-temperature configuration to an average of 1136.56 $Å^3$ during the production run (7.7 % increase). At low temperature the cell lengths are not cubic, b and c are similar in length, and a is approximately 0.5 Å smaller than both. The interaxial angles at 300 K are to close to 90° and the averages are shown on the diagram of $\alpha = 89.84°$, $\beta = 90.08°$ and $\gamma = 90.69°$. While the crystal system is unclear from Figure 4.13, it can be stated with confidence that the low-temperature phase is not cubic.

The lithium ions within tetrahedra are not located at the centre but offset towards the centre of the tetrahedral face which maximally avoids nitrogen. This location faciliates lithium ion oscillations between tetrahedra and octahedra.

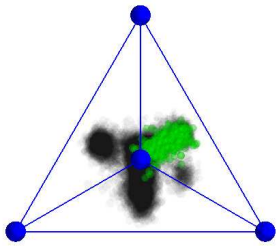

Figure 4.12: Lithium ions positions within the tetrahedra (32 of 64 overplot in a single tetrahedron).

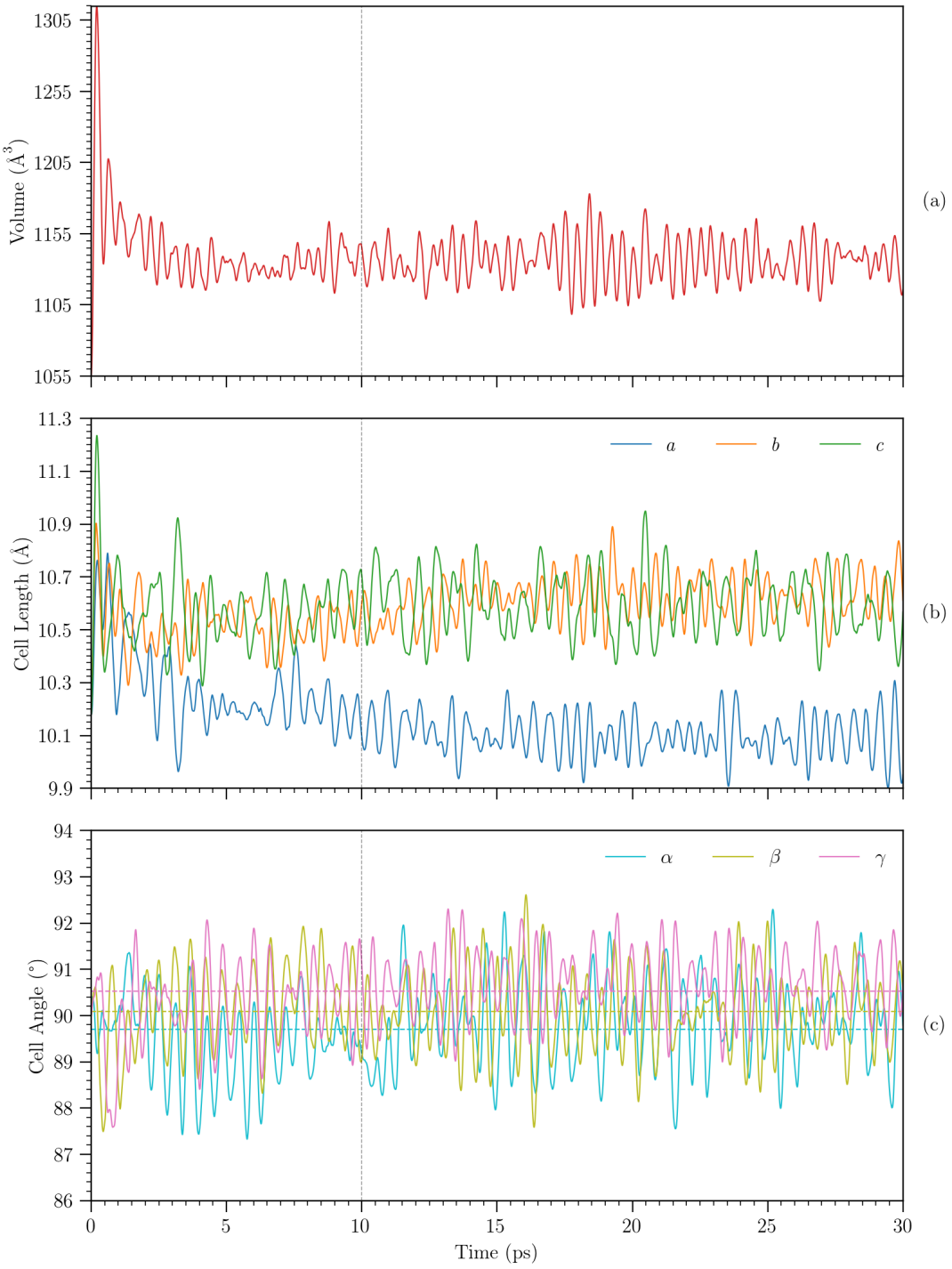

Figure 4.13: Li_2NH (a) volume, (b) cell lengths and (c) cell angles at 300 K during the equilibration and complete production run, including the supplementary data collection. The end of the equilibration period is signified by a vertical line. The average angles are plotted in (c) as dashed horizontal lines. In (b) $b = c$ is coincidental and (c) $\alpha = \beta = 90°$ while γ can vary.

Symmetry elements were identified from the ensemble average atomic positions and used to assign a point group. The ensemble average imide orientations and lithium positions with respect to their nitrogen were evaluated: the two sets of atomic positions were each collapsed onto a single nitrogen at the origin. Lithium up to 3 Å from any nitrogen had their orientation recorded, a cut-off distance was used for lithium because (unlike hydrogen) they are not bonded to the nitrogen.

Three-dimensional spherical histograms were used to represent these distributions around the nitrogen and have been plotted in all directions within the $\langle 100 \rangle$, $\langle 110 \rangle$ and $\langle 111 \rangle$ families. Spherical histograms each contained 1,000 equally distributed bins that were generated by Deserno's algorithm[110] (used previously in Section 3.5) and the counts were normalised to a picosecond so that different temperatures could be directly compared. Figure 4.14 summarises the features of these plots. Rotations between directions in each family were in a counter-clockwise direction around the c axis ([001] direction) whenever possible.

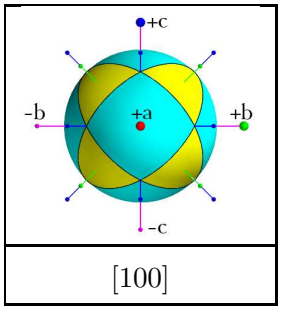

Figure 4.14: Spherical histogram of polyhedral faces around the nitrogen. Miller indices, polyhedron faces and crystal axes are shown looking down the [100] direction. $\langle 100 \rangle$, $\langle 110 \rangle$ and $\langle 111 \rangle$ families of directions are plotted as axes in magenta, dark blue and green respectively. Lattice points are used to orientate the crystal axes, with (1,0,0) in red used to represent $+a$, (0,1,0) in green for $+b$ and (0,0,1) in blue for $+c$. Crystal axes are labelled except for $-a$ because it is hidden behind the sphere. The centre of the sphere represents a nitrogen atom and therefore the 12 $\langle 110 \rangle$ directions correspond to the surrounding nitrogen in Li_2NH. Nitrogen are the vertices of the polyhedra and therefore polyhedron faces are constructed by connecting the $\langle 110 \rangle$ directions. The polyhedra faces are coloured in yellow for tetrahedra and cyan for octahedra, with tetrahedron-to-octahedron face boundaries marked by black lines. This colour code is consistent with Figure 4.10.

Imide orientations at 300 K (10–30 ps) are plotted in Tables 4.2–4.4. The ordering of the imides at low temperature has been the main topic of discussion in the literature, N—H bonds in the computed structure are clearly ordered and therefore identifying their symmetry is key to understanding the phase. Starting from the $\langle 100 \rangle$ family (Table 4.2), a mirror plane is observed down the [100] direction across the equator of the sphere and a two-fold rotational axis along the [001]. This mirror plane is also visible along the equators of the $[\bar{1}00]$, [010] and $[0\bar{1}0]$ directions. The two-fold can additionally be observed between the [100] and $[\bar{1}00]$ directions because the axes have not been inverted, the [100] was simply rotated counter clockwise in [001] to obtain $[\bar{1}00]$. The [001] figure was generated by a 90° clockwise rotation from the [100] along the [010] axis, and the $[00\bar{1}]$ by a 90° counter-

clockwise rotation along [010], followed by a 90° clockwise rotation along [00$\bar{1}$]. (0,0,1) and (0,1,0) points (a, b axes) have been exchanged between the [001] and [00$\bar{1}$] directions, to distinctly show the two-fold rotation down opposite directions. The symmetry elements together give a point group of *2/m* with a unique c-axis. The space group, however, must contain a 2_1 screw axis along c and glide plane perpendicular to c as the symmetry relationships represented on the sphere surface correspond to spatially distinct imides.

The ⟨110⟩ directions (Table 4.4) highlight the locus of all of the hydrogen positions as they track along the tetrahedron-to-octahedron face boundaries. The locus is captured from the ensemble average of all the imide orientations, as individually the imides are localised on the face boundaries. Imide orientations are distributed over 6 of the 12 ⟨110⟩ directions and theses can be divided into four sets of ([101], [1$\bar{1}$0]), ([1$\bar{1}$0]), [10$\bar{1}$]), ([$\bar{1}$01], [$\bar{1}$10]) and ([$\bar{1}$10], [$\bar{1}$0$\bar{1}$]). The entire set of ⟨110⟩ have been included for completeness in Table 4.4.

The imide orientations by tracking between two ⟨110⟩ avoid the ⟨111⟩ directions. ⟨111⟩ directions are shown in Table 4.3 and tabulated by the counter-clockwise rotation from [111] along the [001] axis. The [111], [$\bar{1}\bar{1}\bar{1}$], [$\bar{1}\bar{1}$1] and [11$\bar{1}$] directions (1st and 3rd columns) are furthest from the imides because only one of the three ⟨110⟩ that surround these directions have hydrogen tracking along it. The remaining four ⟨111⟩ directions have hydrogen positions tracking along two of three ⟨110⟩ that surround them, and small displacements off the face boundaries result hydrogen occupation near to these ⟨111⟩ directions.

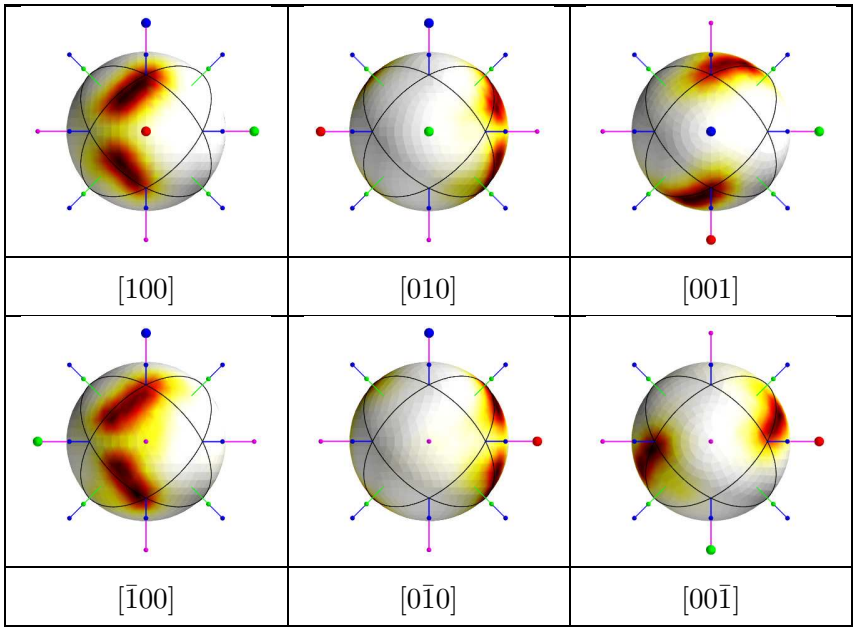

[100]	[010]	[001]
[$\bar{1}$00]	[0$\bar{1}$0]	[00$\bar{1}$]

Table 4.2: Spherical histograms of imide orientations at 300 K shown from the ⟨100⟩ directions. Crystal axes $+a$, $+b$ and $+c$ are represented by (1,0,0) in red, (0,1,0) in green and (0,0,1) in blue respectively. Graph labels are fully described in Figure 4.14.

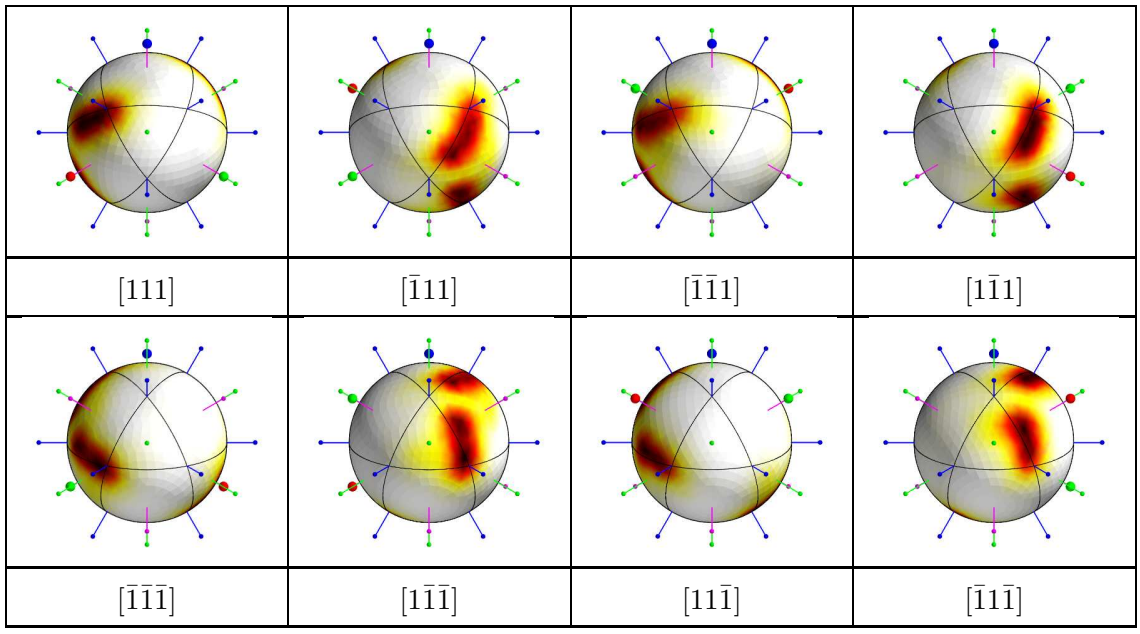

[111]	[$\bar{1}$11]	[$\bar{1}\bar{1}$1]	[1$\bar{1}$1]
[$\bar{1}\bar{1}\bar{1}$]	[1$\bar{1}\bar{1}$]	[11$\bar{1}$]	[$\bar{1}$1$\bar{1}$]

Table 4.3: Spherical histograms of imide orientations at 300 K shown from the ⟨111⟩ directions. Crystal axes $+a$, $+b$ and $+c$ are represented by (1,0,0) in red, (0,1,0) in green and (0,0,1) in blue respectively. Graph labels are fully described in Figure 4.14.

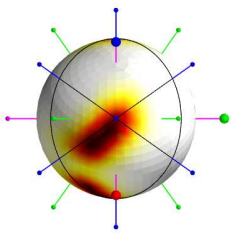	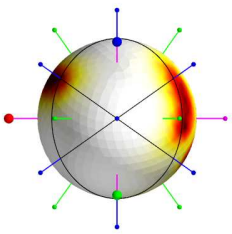	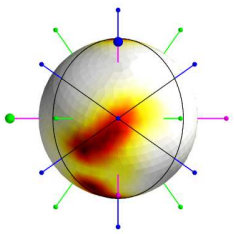
[101]	[011]	[$\bar{1}$01]
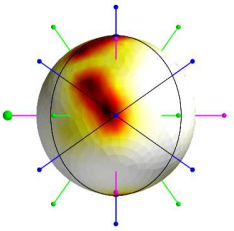	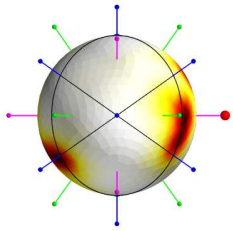	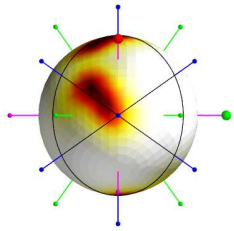
[$\bar{1}$0$\bar{1}$]	[0$\bar{1}\bar{1}$]	[10$\bar{1}$]
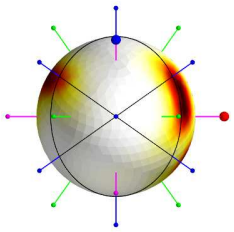	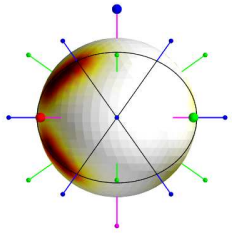	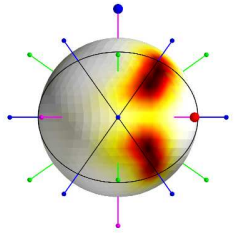
[0$\bar{1}$1]	[110]	[1$\bar{1}$0]
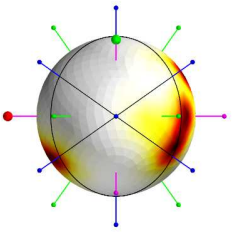	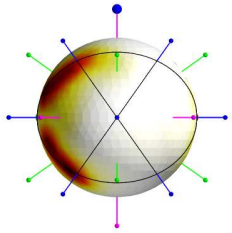	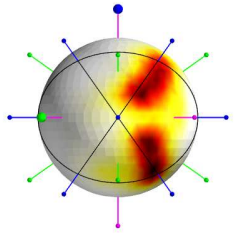
[01$\bar{1}$]	[$\bar{1}\bar{1}$0]	[$\bar{1}$10]

Table 4.4: Spherical histograms of imide orientations at 300 K shown from the ⟨110⟩ directions. Crystal axes $+a$, $+b$ and $+c$ are represented by (1,0,0) in red, (0,1,0) in green and (0,0,1) in blue respectively. Graph labels are fully described in Figure 4.14.

The *2/m* point-group symmetry was also observed for the lithium positions around nitrogen in Tables 4.6–4.8. The symmetry elements are most easily viewed from the ⟨100⟩ directions in Table 4.6 (rotations between directions within the ⟨100⟩ family are the same as those described for the imide group). There is a two-fold rotation axis along the [001]

direction and a mirror plane perpendicular in the ab-plane. This mirror plane is observed in the [100], [$\bar{1}$00], [010] and [0$\bar{1}$0] directions, while the two-fold is most easily viewed from the [001] and [00$\bar{1}$] directions.

The ⟨100⟩ directions correspond to octahedra faces and these are empty with the exception of the single Li^+ interstitial from the Frenkel defect. The lithium ions are mostly located along the ⟨111⟩ directions that correspond to the tetrahedra faces. The ⟨111⟩ directions in Table 4.7 can be separated into two subsets based on whether the lithium ions are more or less localised on the tetrahedra faces; with the lithium ions more localised in the 2nd and 4th columns than the 1st and 3rd. The distributions on the tetrahedra faces have an approximate three-fold symmetry where the lithium ions point down the three ⟨122⟩ directions. ⟨122⟩ directions are located midway between each pair of ⟨100⟩ that make up the tetrahedra edges and this three-fold symmetry is better defined in the more localised distributions (2nd and 4th columns). The more diffuse lithium ions along the ⟨111⟩ (1st and 3rd columns) are viewed as deformations of the localised distributions. ⟨110⟩ directions are included in Table 4.8 for completeness.

Taking into account these site symmetries, the ensemble average of the structure between 10–30 ps is consistent with an $I112/b$ structure (unique axis c). Figure 4.15 contains axis projections of the ensemble averaged structure and the unit cell for the $I112/b$ space group, and Table 4.5 details the transformations from $I112/b$ to the conventional $C2/c$ setting and supercell.

Table 4.5: $I112/b$ transformations.

Transformation	Coordinate transformation matrix	Shift of origin
$I112/b \rightarrow C2/c$	$\begin{pmatrix} 0 & -1 & 0 \\ 0 & 0 & 1 \\ 1 & -1 & 0 \end{pmatrix}$	$\begin{pmatrix} 0 & 0 & 0 \end{pmatrix}$
$I112/b \rightarrow$ supercell	$\begin{pmatrix} 0 & -2 & 0 \\ 1 & 0 & 0 \\ 0 & 0 & 2 \end{pmatrix}$	$\begin{pmatrix} 1/8 & 0 & 1/4 \end{pmatrix}$

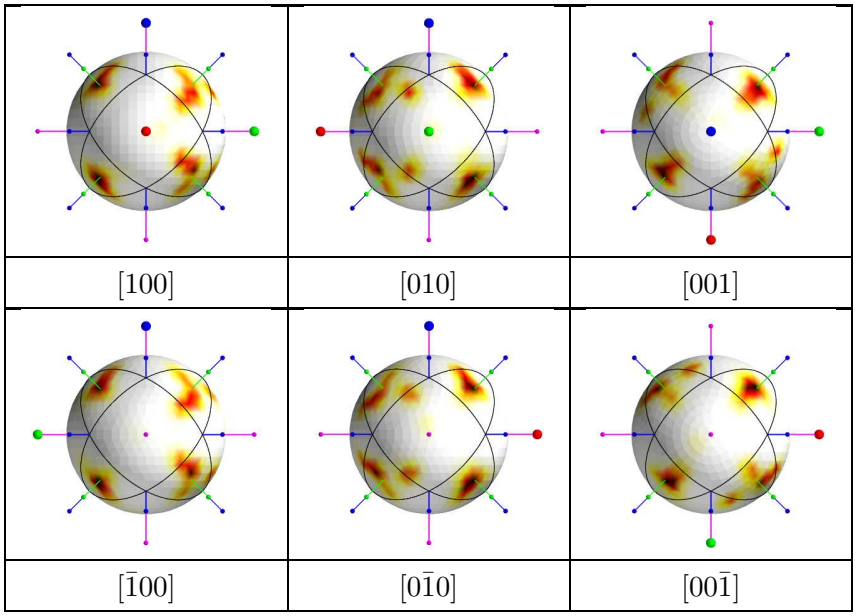

Table 4.6: Spherical histograms of lithium orientations with respect to nitrogen at 300 K shown from the ⟨100⟩ directions. Crystal axes $+a$, $+b$ and $+c$ are represented by (1,0,0) in red, (0,1,0) in green and (0,0,1) in blue respectively. Graph labels are fully described in Figure 4.14.

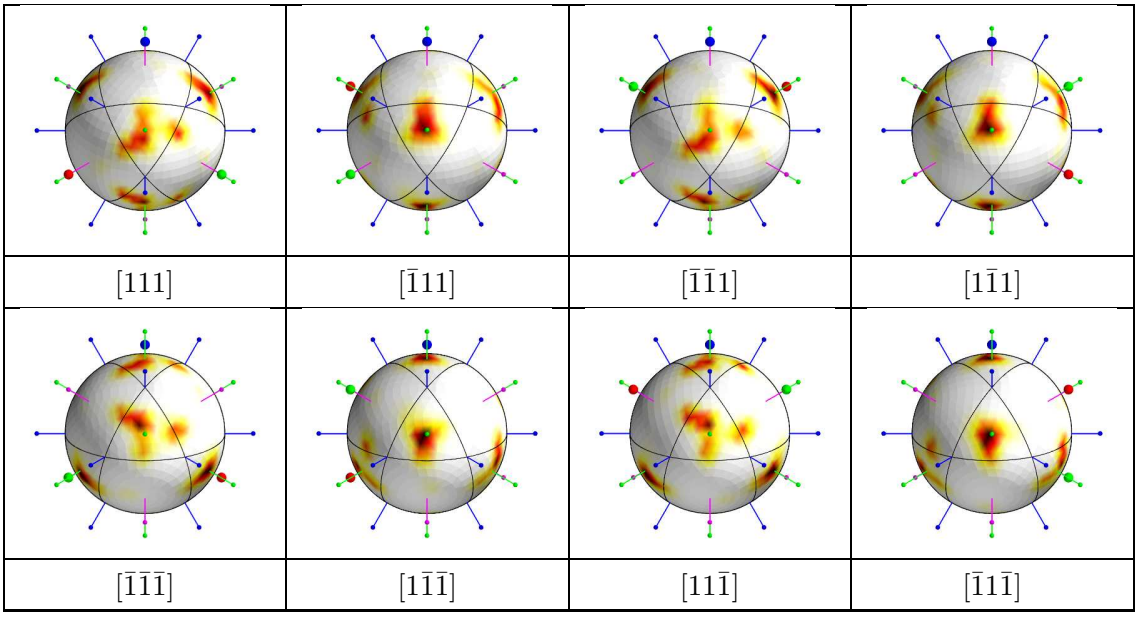

Table 4.7: Spherical histograms of lithium orientations with respect to nitrogen at 300 K shown from the ⟨111⟩ directions. Crystal axes $+a$, $+b$ and $+c$ are represented by (1,0,0) in red, (0,1,0) in green and (0,0,1) in blue respectively. Graph labels are fully described in Figure 4.14.

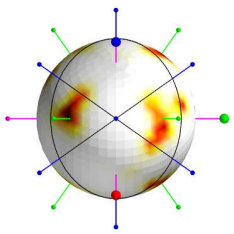	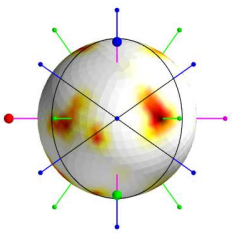	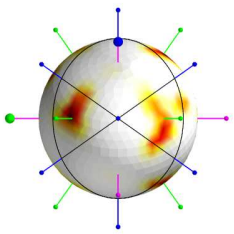
[101]	[011]	[$\bar{1}$01]
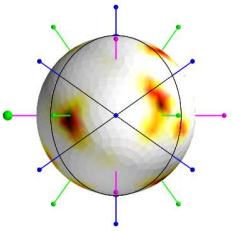	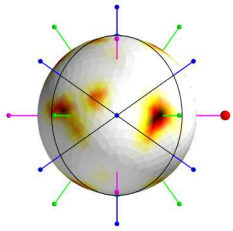	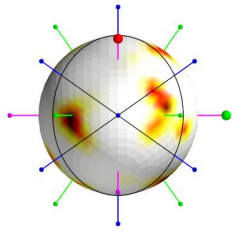
[$\bar{1}$0$\bar{1}$]	[0$\bar{1}\bar{1}$]	[10$\bar{1}$]
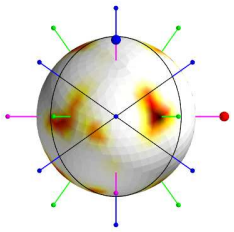	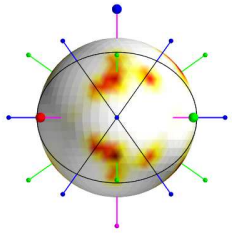	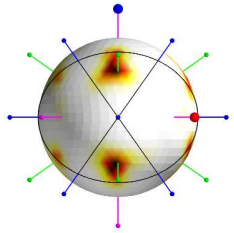
[0$\bar{1}$1]	[110]	[1$\bar{1}$0]
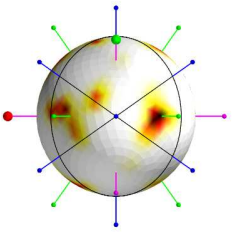	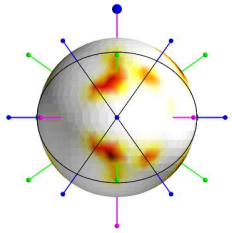	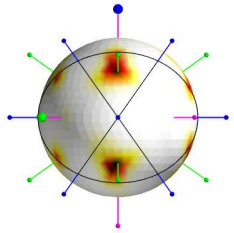
[01$\bar{1}$]	[$\bar{1}\bar{1}$0]	[$\bar{1}$10]

Table 4.8: Spherical histograms of lithium orientations with respect to nitrogen at 300 K shown from the ⟨110⟩ directions. Crystal axes $+a$, $+b$ and $+c$ are represented by (1,0,0) in red, (0,1,0) in green and (0,0,1) in blue respectively. Graph labels are fully described in Figure 4.14.

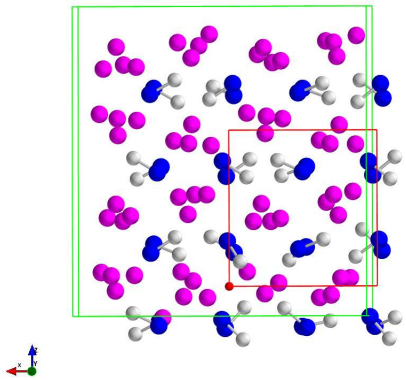

(a)

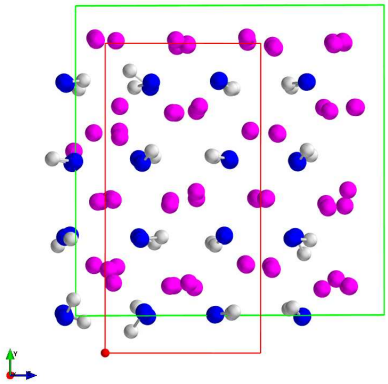

(b)

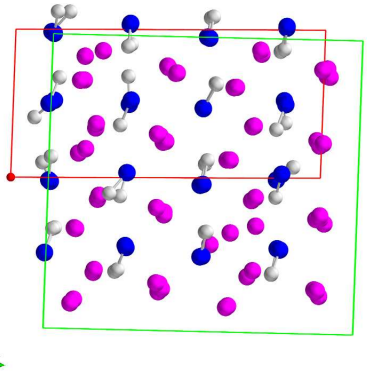

(c)

Figure 4.15: Ensemble averaged low-temperature lithium imide structure with the unit cell for the $I112/b$ space group shown, viewed along the (a) x-axis (b) y-axis and (c) z-axis. Lithium are shown in magenta, nitrogen in blue and hydrogen in white.

At 400 K, the structure remained trapped in the same *2/m* point group symmetry observed at 300 K. This simulation was a continuation from 300 K and the overall structure was unchanged from the beginning to the end of the production run. The same general structural features were identified at 400 K for the imide orientations and lithium orientations with respect to nitrogen; the distributions were observed broadened which is expected from increased thermal motion. To avoid restating the points made with the 300 K data, the 400 K data are included but not discussed, with spherical histograms given in Tables 4.9, 4.10, 4.11, 4.12, 4.13 and 4.14.

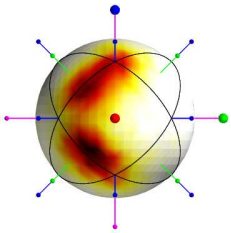	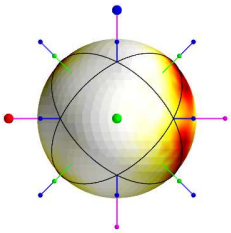	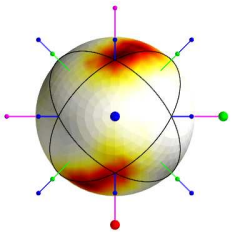
[100]	[010]	[001]
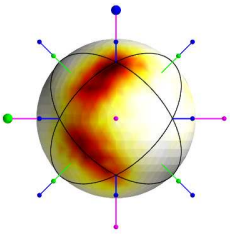	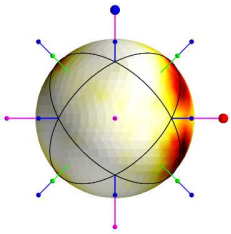	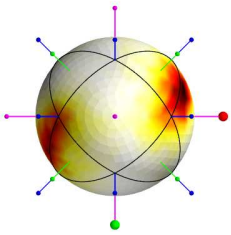
[$\bar{1}$00]	[0$\bar{1}$0]	[00$\bar{1}$]

Table 4.9: Spherical histograms of imide orientations at 400 K shown from the $\langle 100 \rangle$ directions. Crystal axes $+a$, $+b$ and $+c$ are represented by (1,0,0) in red, (0,1,0) in green and (0,0,1) in blue respectively. Graph labels are fully described in Figure 4.14.

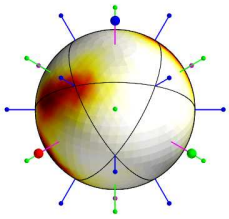	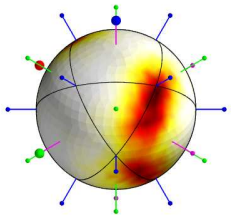	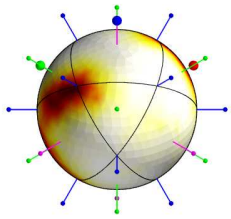	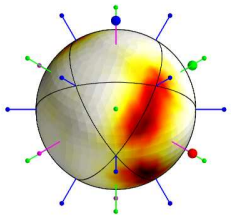
$[111]$	$[\bar{1}11]$	$[\bar{1}\bar{1}1]$	$[1\bar{1}1]$
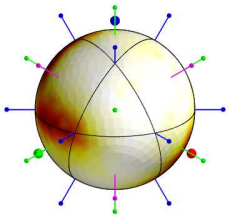	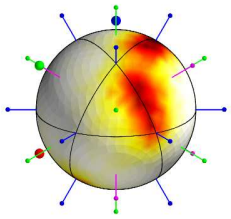	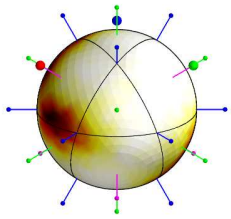	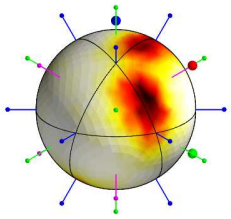
$[\bar{1}\bar{1}\bar{1}]$	$[1\bar{1}\bar{1}]$	$[11\bar{1}]$	$[\bar{1}1\bar{1}]$

Table 4.10: Spherical histograms of imide orientations at 400 K shown from the $\langle 111 \rangle$ directions. Crystal axes $+a$, $+b$ and $+c$ are represented by (1,0,0) in red, (0,1,0) in green and (0,0,1) in blue respectively. Graph labels are fully described in Figure 4.14.

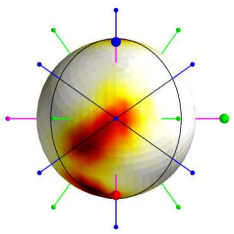	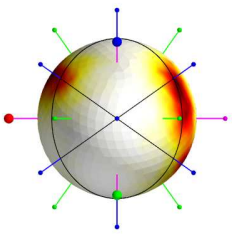	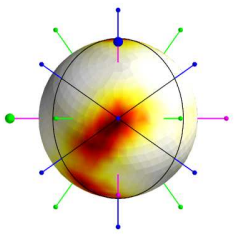
[101]	[011]	[$\bar{1}$01]
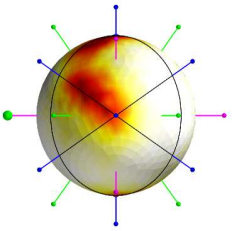	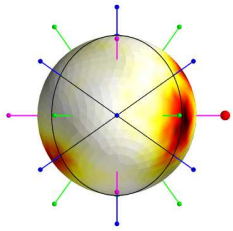	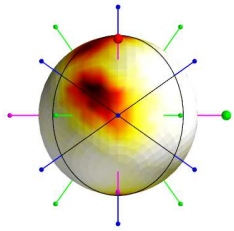
[$\bar{1}$0$\bar{1}$]	[0$\bar{1}\bar{1}$]	[10$\bar{1}$]
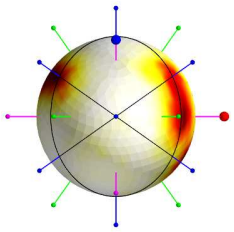	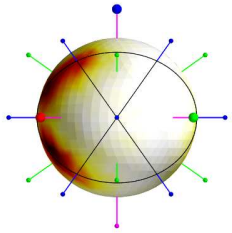	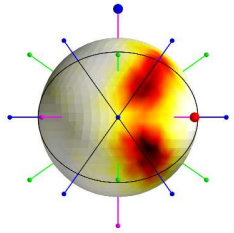
[0$\bar{1}$1]	[110]	[1$\bar{1}$0]
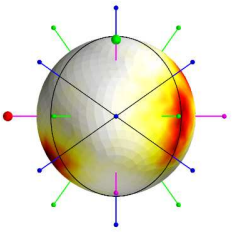	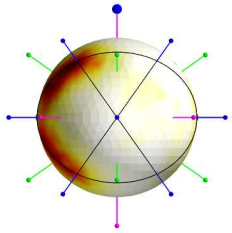	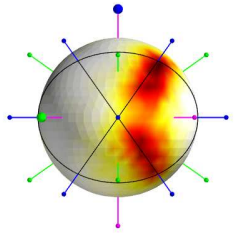
[01$\bar{1}$]	[$\bar{1}\bar{1}$0]	[$\bar{1}$10]

Table 4.11: Spherical histograms of imide orientations at 400 K shown from the ⟨110⟩ directions. Crystal axes $+a$, $+b$ and $+c$ are represented by (1,0,0) in red, (0,1,0) in green and (0,0,1) in blue respectively. Graph labels are fully described in Figure 4.14.

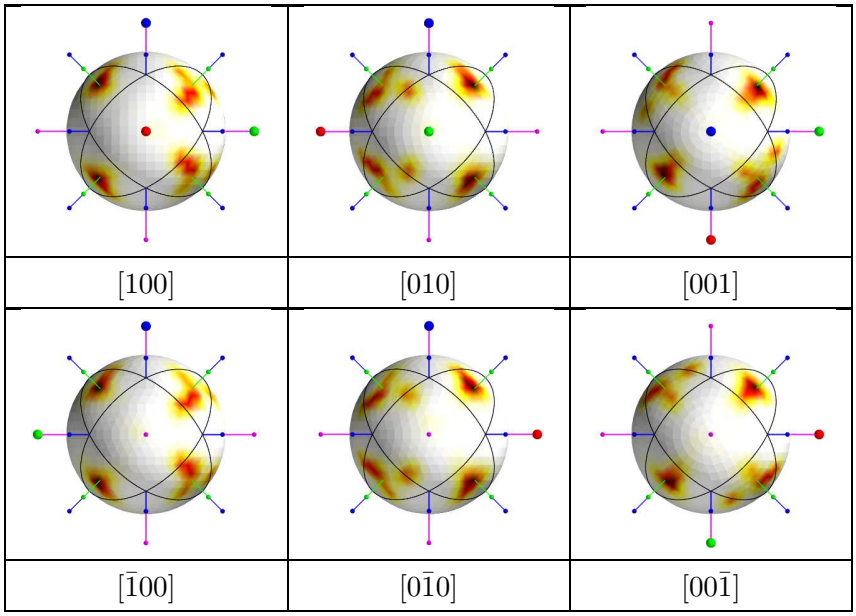

Table 4.12: Spherical histograms of lithium orientations with respect to nitrogen at 400 K shown from the ⟨100⟩ directions. Crystal axes $+a$, $+b$ and $+c$ are represented by (1,0,0) in red, (0,1,0) in green and (0,0,1) in blue respectively. Graph labels are fully described in Figure 4.14.

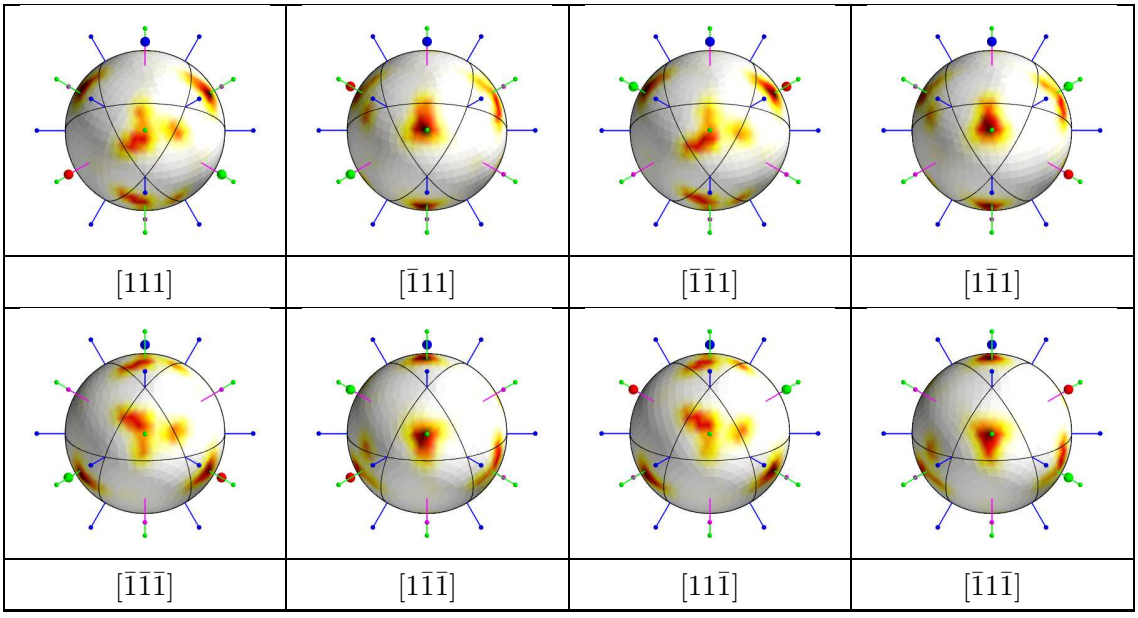

Table 4.13: Spherical histograms of lithium orientations with respect to nitrogen at 400 K shown from the ⟨111⟩ directions. Crystal axes $+a$, $+b$ and $+c$ are represented by (1,0,0) in red, (0,1,0) in green and (0,0,1) in blue respectively. Graph labels are fully described in Figure 4.14.

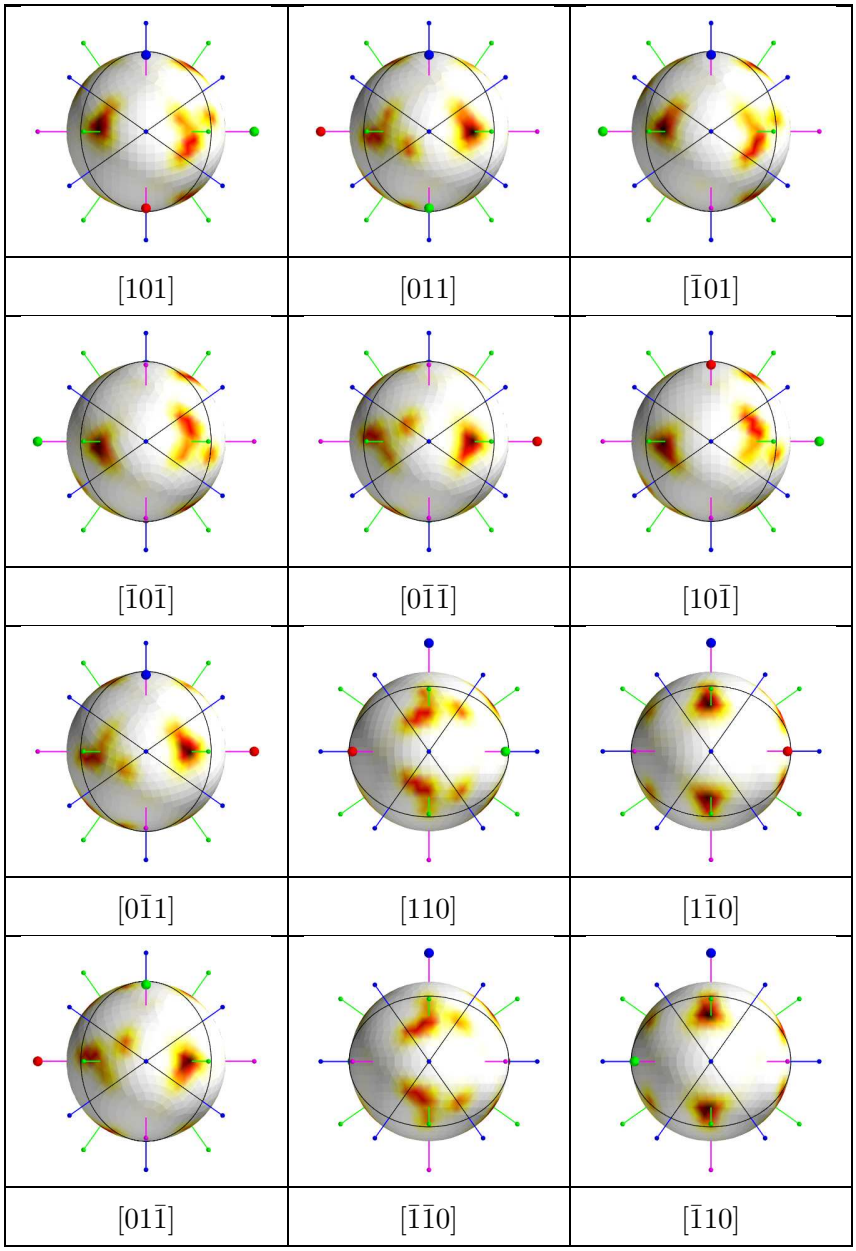

Table 4.14: Spherical histograms of lithium orientations with respect to nitrogen at 400 K shown from the ⟨110⟩ directions. Crystal axes $+a$, $+b$ and $+c$ are represented by (1,0,0) in red, (0,1,0) in green and (0,0,1) in blue respectively. Graph labels are fully described in Figure 4.14.

4.6 Structural changes during heating to 700 K

Lithium migration after the initial defect chain at 300 K does not reoccur until the structure reaches 500 K; the first Li^+ movements are observed at 38.3 ps which is 3.3 ps into the 500 K production run. Correlated lithium movements have been separated into chains of motion in Figure 4.16 for simplicity. Lithium movement restarted with a tetrahedron-to-tetrahedron migration from T551 in chain 1. The net result of this chain was that an octahedral defect propagated from O662 to O482. Lithium Frenkel defects formed at 500 K in chains 2, 5, 6, 7, and 8, which together with the 300 K defect meant that $^6/_{32}$ octahedra were occupied by the end of the 500 K run. Chain 3 propagated the chain 1 defect from O482 to O648, with lithium exiting O482 2.4 ps after it was first occupied. Uniquely during this chain, O622 was simultaneously occupied by two lithium ions; however, this occurred for only 13 fs. In chain 4, an octahedral defect propagated from O644 to O864 and, in chain 9, O446 propagated to O622. Li_2NH at 500 K contains 6 defects. However, 2 of the 6 defects were repaired in the 2 ps that followed (these are not shown here as they occurred during the 600 K equilibration): O864 (Chain 4) to T755 (Chain 5) and O486 (Chain 6) to T371 (original 300 K defect).

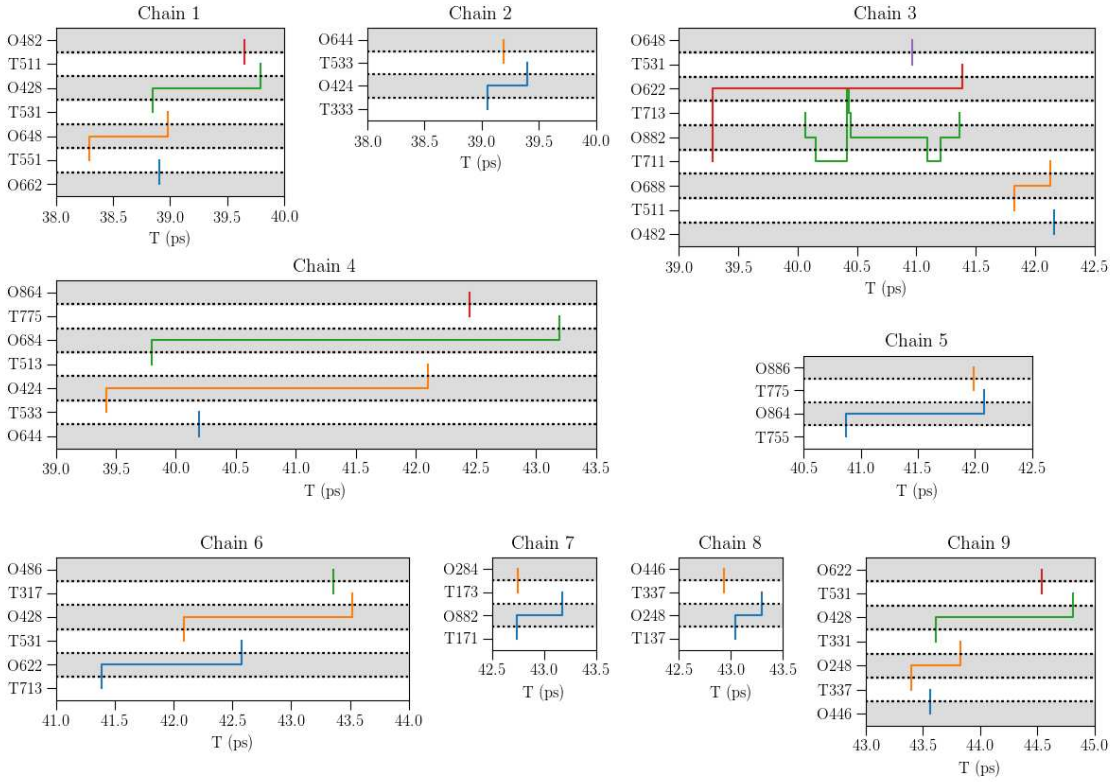

Figure 4.16: Lithium migration in Li_2NH at 500 K separated into nine chains of connected lithium movement. Polyhedra are assigned either T or O followed by a unique three number index for their location within Li_2NH. Grey regions correspond to octahedra and white regions tetrahedra. Colours are used to identify lithium movement within each chain but have no interchain relationship.

Before lithium migration at 38.3 ps, the structure at 500 K was locked in the low-temperature $I112/b$ phase; this movement corresponds to a phase change. Figure 4.17 contains 1 fs time interval averages of the (a) volume and (b) cell lengths over 300–700 K. The volume is observed (after initial equilibration) to expand as the temperature is increased from 300–500 K and then contracts from 39 ps because of the phase change. The 500 K run is divided into three phases with distinct volumes: (i) a high-volume phase at 35–38 ps, (ii) mid-volume phase at 40–42 ps and (iii) low-volume phase at 43–45 ps.

The high-volume phase is $I112/b$ and the cell length trends are the same as those observed at 300 K, where b and c are similar in length and a is smaller than both. Between the

high-volume and mid-volume phases the cell lengths underwent domain-switching in a and c, and during this period there was also significant lithium movement; see chains 1–4 in Figure 4.16. Changes in cell parameters are not evident from examination of the volume alone. The mid-volume phase was identified as an intermediary phase because the volume was relatively constant. During this phase, the cell became metrically approximately cubic. On the evolution of the low-volume phase, this cubic intermediary structure was lost and the cell lengths became different. The low-volume phase is highly defective as, from 43.3 ps, six lithium ions are displaced into octahedral interstices. There is on average a 28.8 Å^3 difference between the 500 K high-volume and low-volume phases.

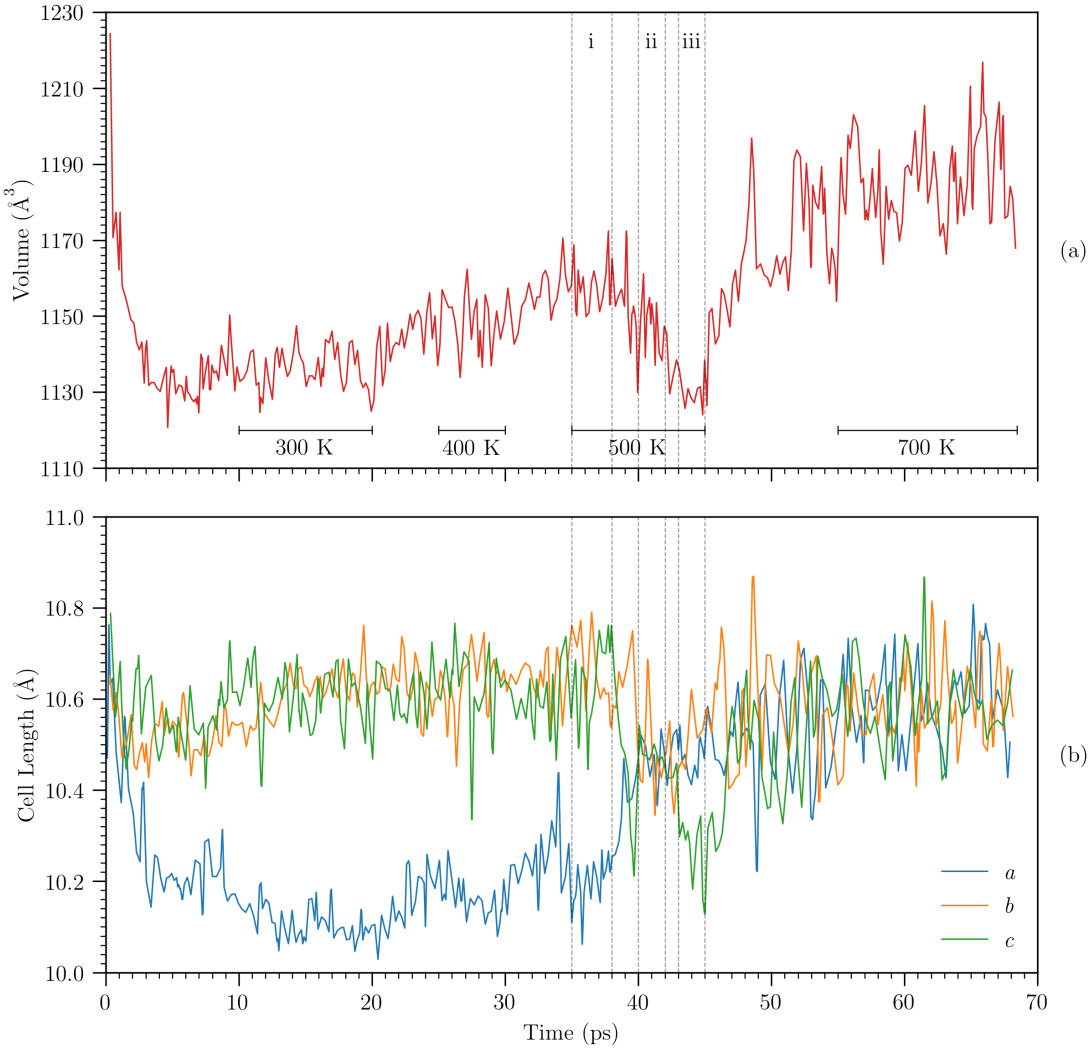

Figure 4.17: Midpoint (a) volumes and (b) cell lengths of Li_2NH heated from 300–700K, the original run is shown without the supplementary timesteps at 20 ps and 50 ps. 500 K (i) high-volume (ii) mid-volume and (iii) low-volume phases. The lines with vertical bars at either end correspond to production runs.

The orientations of Li around N were plotted for all these phases as two-dimensional histograms in Figure 4.18. Scatter plots of H orientations around N are shown in Figure 4.19. Mercator projections were chosen rather than sets of three-dimensional histograms because of the shorter time frames collected for the three phases; scatter plots were more appropriate for the imide orientations given their large dispersion. As Li^+ ions move

through the structure, their orientation with respect to N was captured for ions that were limited to a 3.0 Å distance from nitrogen.

Lithium orientations in the high-volume phase (i) have the same general distribution as the 300 K phase in Table 4.7. The lithium orientations are mainly localised inside the tetrahedra and the same distortions at 300 K were observed along the [111], $[\bar{1}\bar{1}\bar{1}]$, $[\bar{1}\bar{1}1]$, $[11\bar{1}]$ directions. The hydrogen orientations in the high-volume phase are collectively the same as those at 300 K (Figure 4.11), with orientations along the octahedron-to-tetrahedron face boundaries and octahedron directions mostly vacant. Locally however these orientations are very different and this is evident from the average imide positions. Fewer average imide orientations are located along the face boundaries and the points are generally more clustered, in contrast to the 300 K data where the orientations are dispersed across the boundaries.

In the mid-volume phase (ii), the lithium ions with respect to the nitrogen are cubic in arrangement; the lithium ions are localised along the ⟨111⟩ directions and the aforementioned lithium orientation distortions in (i) have been lost. There is also a greater population of lithium inside octahedral interstices because during this period defects have formed and the lithium are readily moving through the structure. Relative to the nearest nitrogen, lithium ions are mostly positioned between the ⟨111⟩ directions along a ⟨100⟩ diagonal. Hydrogen in the mid-volume phase exhibits higher symmetry orientations with points clustered along the polyhedral face boundaries. This ordering however is explained by the short duration of the run; 2 ps provides a snapshot of hydrogen positions but is not adequate time to sample all hydrogen orientations. The mid-volume phase was an intermediate step in the overall volume decrease at 500 K, between the monoclinic structure at high volume and cubic structure at low volume. This phase is cubic from the lithium arrangement and if the crystal structure had been long-lived, would expect the hydrogen to have sampled more orientations and therefore recover a disordered cubic arrangement of hydrogen.

The orientations of lithium around nitrogen are similar in the low-volume phase (iii) as the mid-volume phase, with lithium along the ⟨111⟩ directions in a cubic configuration. At low volume the lithium are much more localised to the ⟨111⟩ and because this phase is the most defected of the three, containing six lithium ions displaced into octahedra, there is also significant population of the ⟨100⟩ directions. Hydrogen are more dispersed in the low-volume phase than in the mid-volume phase, still this distribution is not completely disordered, as for example, both the [010] and [0$\bar{1}$0] directions are less populated. This again relates to the short time frame for collecting hydrogen orientations. Nevertheless, the hydrogen distribution is almost cubic and the lithium arrangement is cubic in the low-volume structure.

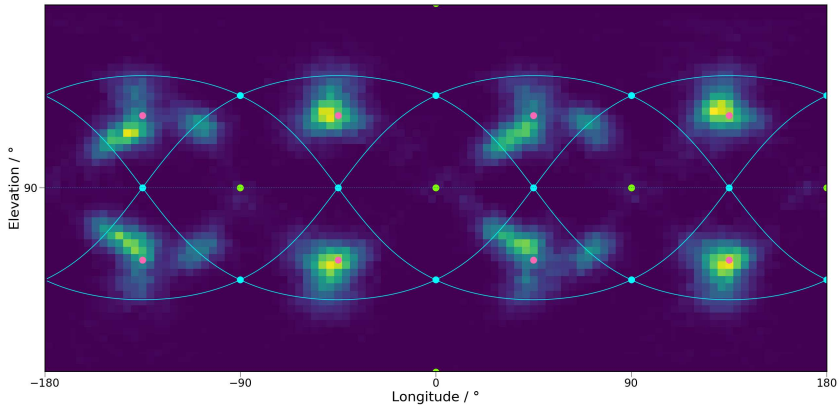

(i) High volume. 35–38 ps.

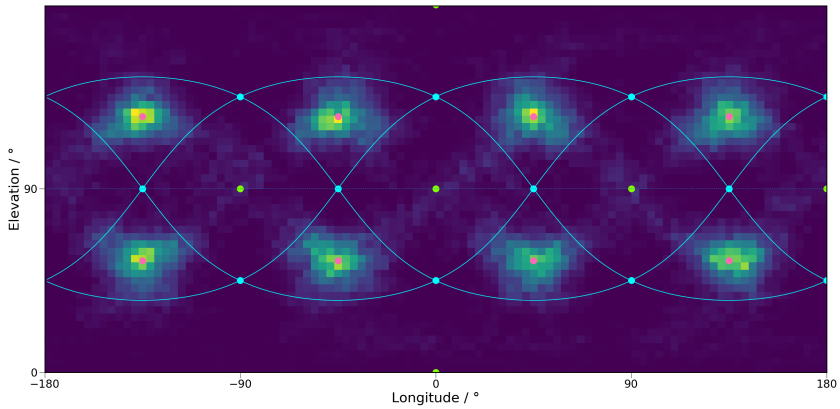

(ii) Mid volume. 40–42 ps.

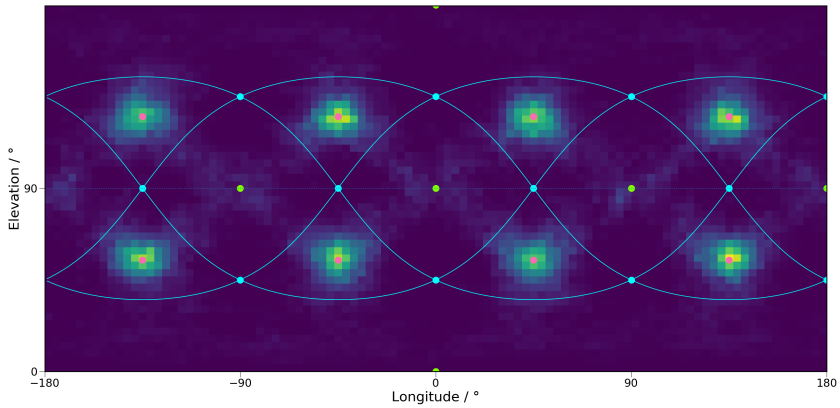

(iii) Low volume. 43–45 ps.

Figure 4.18: 2D-histograms of Mercator projections for the orientations of Li around N in the Li_2NH supercell at 500 K: separated into three phases based on the volume. Angles are calculated for Li up to 3.0 Å away from N. Graph labels are fully described in Figure 4.10 with light blue used alternatively for the ⟨110⟩ directions and face boundaries so that they are visible on the histogram colourmap. 5,000 bins used (100x × 50y).

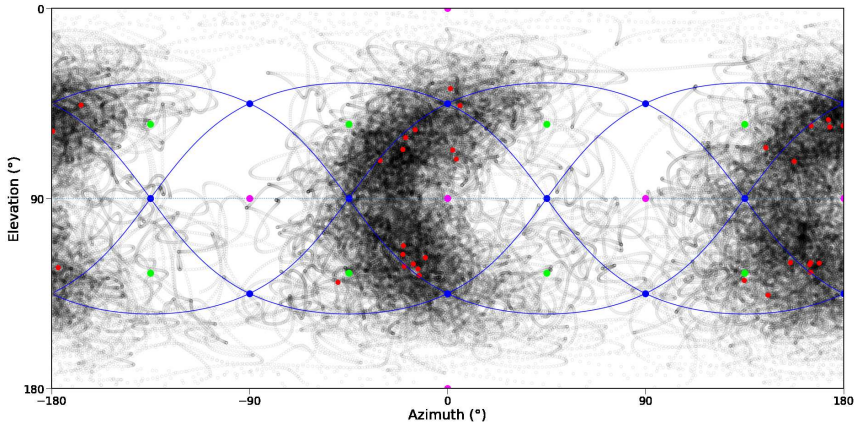

(i) High volume. 35–38 ps, plotted every 7.5 fs.

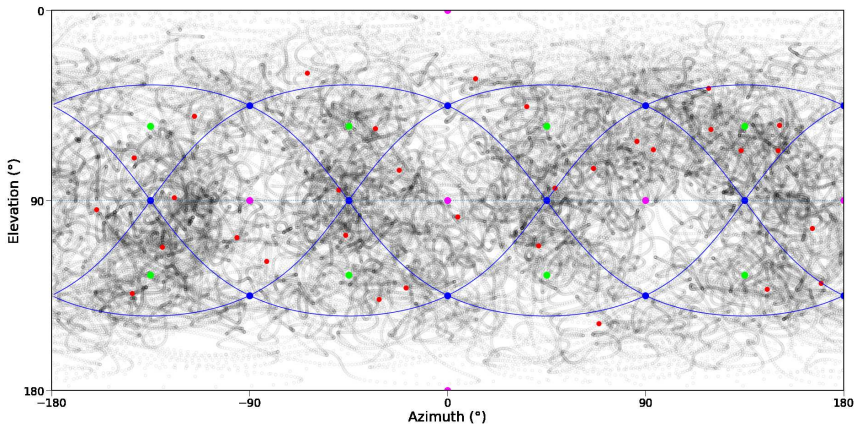

(ii) Mid volume. 40–42 ps, plotted every 5 fs.

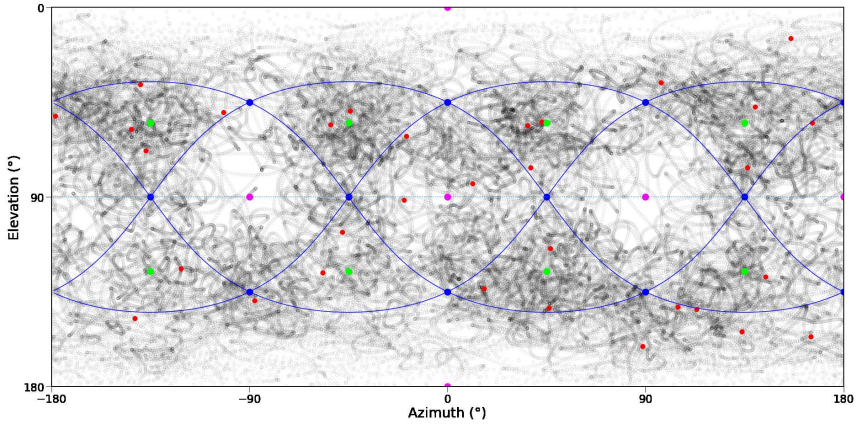

(iii) Low volume. 43–45 ps, plotted every 5 fs.

Figure 4.19: Mercator projections for the orientations of 32 H^+ around N in the Li_2NH supercell at 500 K: separated into three phases based on the volume. Ensemble average positions of the 32 imides are shown in red. Graph labels are fully described in Figure 4.10.

At 600–700 K the volume has expanded and the cell lengths all oscillate within the range ∼10.4–10.8 Å without any one length being significantly distinct, which is indicative of a cubic phase. The interaxial angles remain close to 90°. All features at 600 K and 700 K are generically the same and so the 700 K data are discussed given the longer calculation time. To ascertain the symmetry of the high-temperature structure, lithium positions around nitrogen were plotted as three-dimensional histograms. ⟨111⟩, ⟨100⟩ and ⟨110⟩ directions are shown in Tables 4.15, 4.16, and 4.17. Beginning from the ⟨111⟩ views, three-fold symmetry is observed for lithium along all eight directions (four three-fold axes of rotation); this is consistent with cubic symmetry, where the four body diagonals of a cube are equivalent. There is four-fold symmetry depicted along the ⟨100⟩ directions (three axes of rotation) and two-fold symmetry depicted along the ⟨110⟩ directions (six axes of rotation). All these rotational symmetries correspond to cubic symmetry. Three mirror planes are observable looking down each direction within the ⟨100⟩ and ⟨110⟩ families. Two of the mirror planes are perpendicular to the direction of view: one is horizontal along the equator of the sphere and one is vertical with a line from the North to South Pole (equivalent to the prime meridian). The third mirror plane is parallel to the direction of view, through the hemisphere. Lithium are arranged in a cubic geometry on the histogram, with 8 Li^+ located along the ⟨111⟩ directions around the central nitrogen. The migration of lithium within the phase is visible from the octahedral faces. Lithium occupation of the octahedra is however small by comparison to the tetrahedra, which correspond to ⟨111⟩ directions. The lithium positions are consistent with the reported cubic anti-fluorite $Fm\bar{3}m$ structure.

A powder diffraction pattern was calculated from the average MD structure in Figure 4.20. The four major peaks from the experimental pattern were recovered in the calculated structure; with additional minor peaks in (i) due to an averaged structure of 128 atoms being unable to capture (in a single configuration) uniformly distributed imide groups or a full representation of the lithium arrangements.

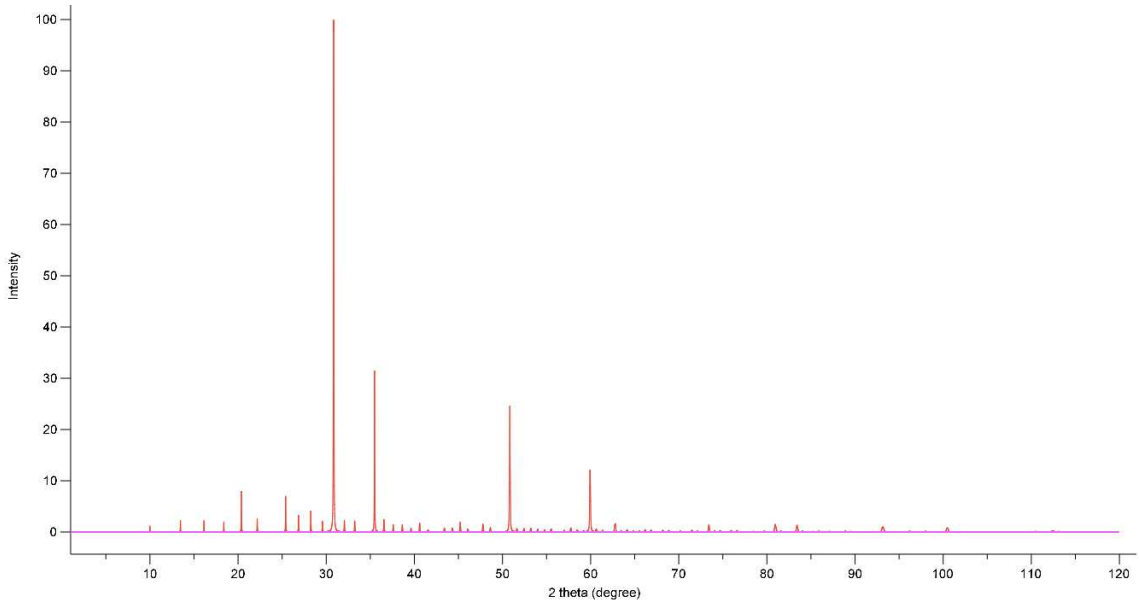

(i) Average MD structure at 700 K.

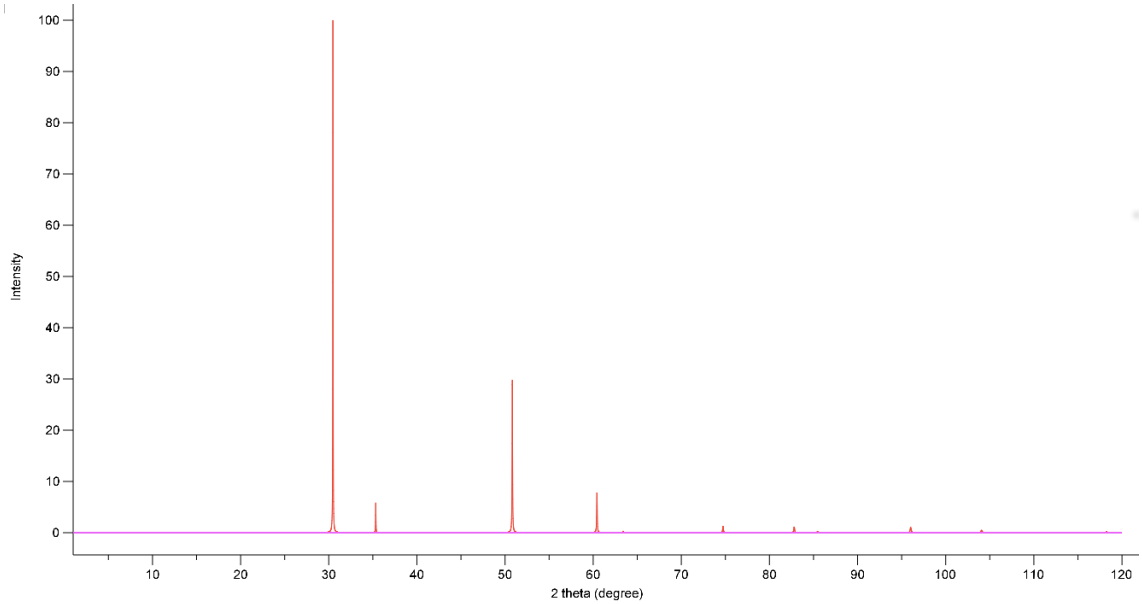

(ii) Experimental neutron powder diffraction pattern of the $Fm\bar{3}m$ phase.

Figure 4.20: Powder diffraction patterns of the high-temperature structure of lithium imide. The pattern for the average MD structure (i) was calculated using VESTA (Ref. 115) and (ii) sourced from the ICSD (Ref. 114).

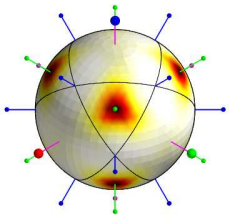	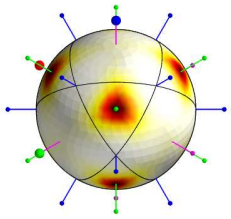	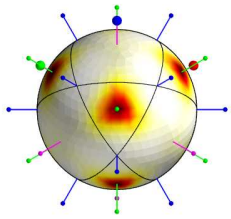	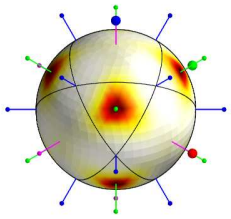
[111]	[$\bar{1}$11]	[$\bar{1}\bar{1}$1]	[1$\bar{1}$1]
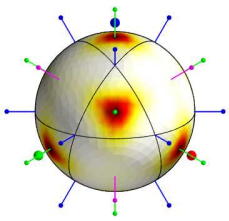	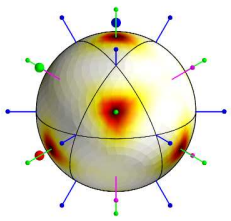	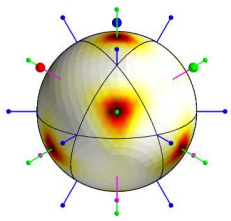	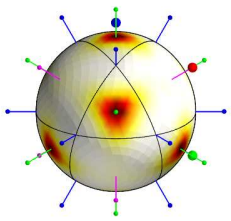
[$\bar{1}\bar{1}\bar{1}$]	[1$\bar{1}\bar{1}$]	[11$\bar{1}$]	[$\bar{1}$1$\bar{1}$]

Table 4.15: Spherical histograms of lithium orientations with respect to nitrogen at 700 K shown from the ⟨111⟩ directions. Crystal axes $+a$, $+b$ and $+c$ are represented by (1,0,0) in red, (0,1,0) in green and (0,0,1) in blue respectively. Graph labels are fully described in Figure 4.14.

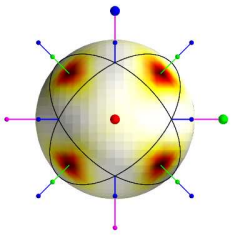	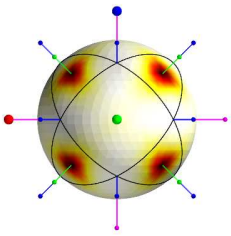	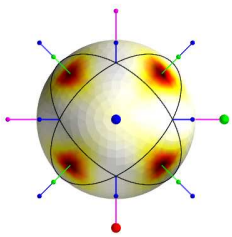
[100]	[010]	[001]
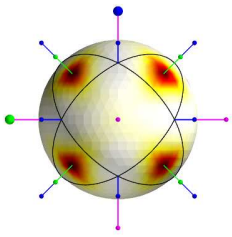	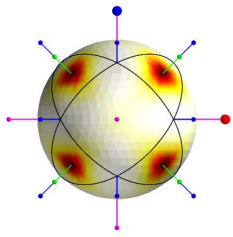	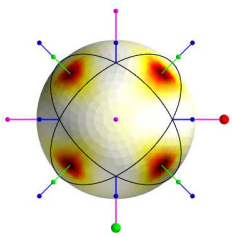
[$\bar{1}$00]	[0$\bar{1}$0]	[00$\bar{1}$]

Table 4.16: Spherical histograms of lithium orientations with respect to nitrogen at 700 K shown from the ⟨100⟩ directions. Crystal axes $+a$, $+b$ and $+c$ are represented by (1,0,0) in red, (0,1,0) in green and (0,0,1) in blue respectively. Graph labels are fully described in Figure 4.14.

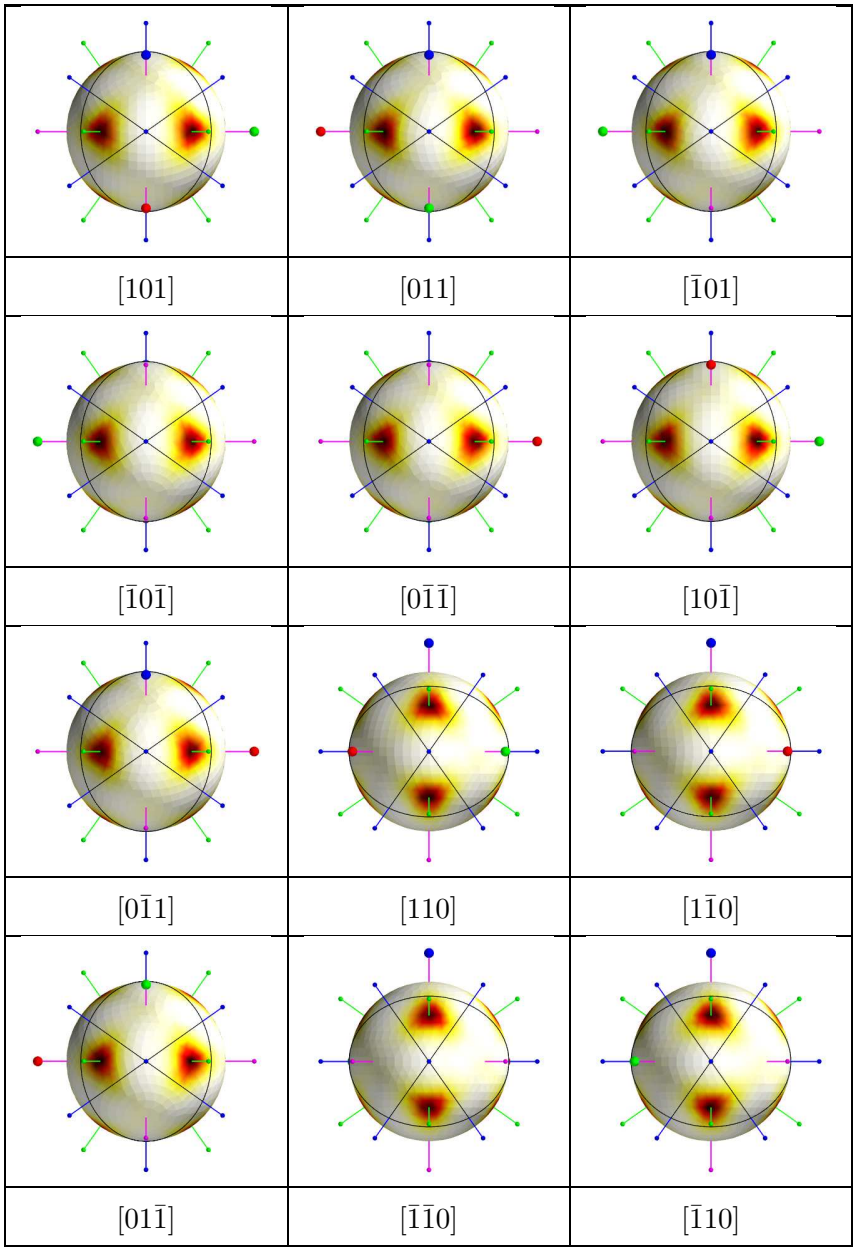

Table 4.17: Spherical histograms of lithium orientations with respect to nitrogen at 300 K shown from the ⟨110⟩ directions. Crystal axes $+a$, $+b$ and $+c$ are represented by (1,0,0) in red, (0,1,0) in green and (0,0,1) in blue respectively. Graph labels are fully described in Figure 4.14.

Imide orientations at 700 K are disordered and the hydrogen are uniformly distributed around the nitrogen in Figure 4.21. The local imide orientations are also dispersed. A Mercator projection was selected because a series of three-dimensional histograms pro-

vided no additional information for these distributions. Disordered imide orientations are consistent with a cubic $Fm\bar{3}m$ structure. In previous studies,[54] the hydrogen distribution in the high temperature is approximated by locating the hydrogen at $192\,l$ sites around the $\langle 111 \rangle$ directions. The hydrogen are essentially uniformly distributed in Figure 4.21.

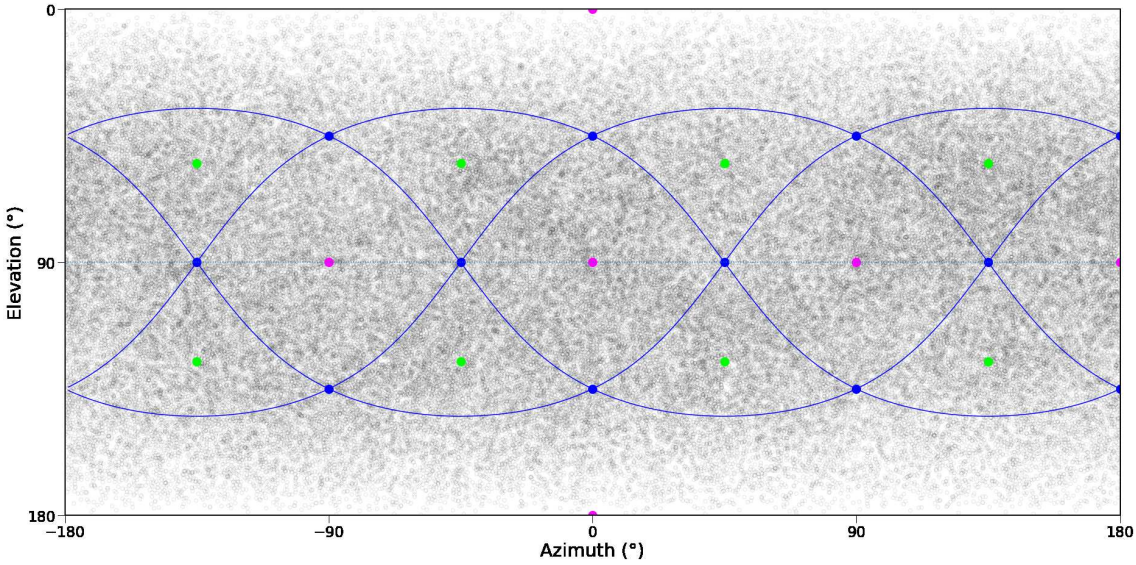

Figure 4.21: Mercator projection for the orientations of 32 H^+ around N in the Li_2NH supercell at 700 K. 13.47 ps run plotted every 5 fs to avoid excessive over-plotting. Graph labels are fully described in Figure 4.10.

4.7 Lithium mobility at 700 K

After the 500 K run the simulation cell was heated to 600 K for 5 ps then 700 K for 5 ps in the original simulation (without supplementary collection), and held at 700 K from 55–68 ps. At higher temperatures, lithium movement within the structure increased and by 700 K it became impractical to trace all the migrations using schematic diagrams (e.g. Figures 4.6 and 4.16). Instead a histogram of tetrahedron-to-tetrahedron lithium movements was produced using 1 ps bins. These are illustrated in Figure 4.22 and, hereafter, are referred to as moves.

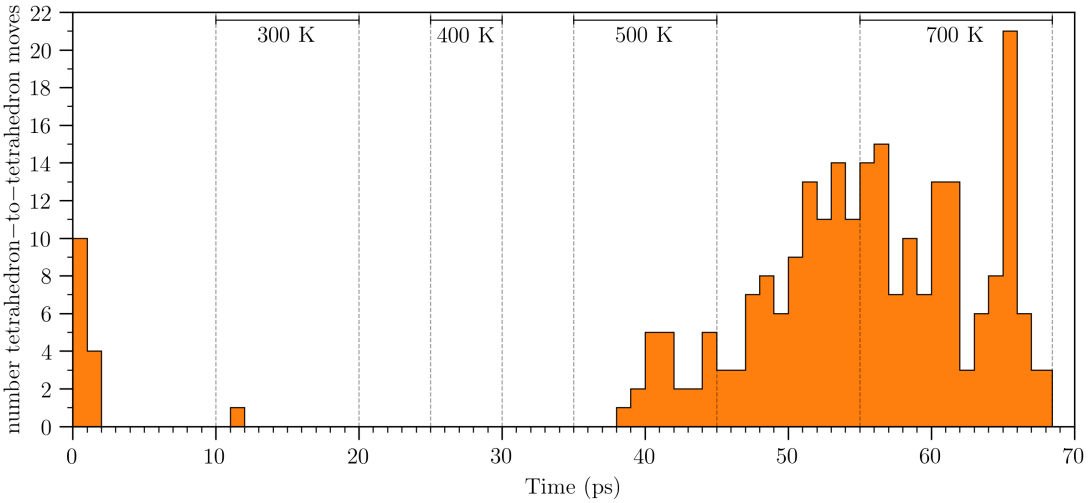

Figure 4.22: Tetrahedron-to-tetrahedron lithium movements per picosecond, the original run is shown with Li_2NH heated from 300–700 K without the supplementary timesteps. The last bin is shorter because the run ended prematurely at 68.4575 ps (68.0000–68.4575 ps). Production runs are labelled.

Figure 4.22 also summarizes the lithium motion already discussed at $\leq$ 500 K; the first defect was formed at high temperature during the initial equilibration period, from 14 lithium moves in the first 2 ps. At 11–12 ps, a single move occurred and this was the only lithium migration at either 300 K or 400 K, including the additional 300 K run (given that the initial movement was at higher temperature). At 38 ps and 500 K, lithium migration resumed. There were 22 moves in the 7 ps that followed which resulted in five additional defects being formed in the structure.

Over the 700 K run, there were a total of 129 moves in 12.45 ps or 10.36 ps^{-1}, compared to 3.14 ps^{-1} at 500 K once migration had started. Lithium ions were much more mobile at higher temperature, as to be expected and the likelihood of forming a defect increases with the greater number of moves. A maximum of 21 moves were observed between 65–66 ps which coincided with the highest average temperature recorded over a given picosecond of 797 K (see Figure 4.5). Lithium movements are correlated which results in a knock-on, cascade effect throughout the structure and explains why a high number of moves can

occur over a single picosecond. Substantial lithium motion is a defining feature of the high-temperature phase.

4.8 Rapidly cooling the high-temperature structure

The 300 K lithium imide phase obtained on heating was a frustrated structure due to the formation of a single Frenkel defect. The high-temperature phase was cooled to determine if the same or a different low-temperature phase would be recovered, and thus establish whether the initial low-temperature structure was a consequence of initial rapid heating.

The initial structure used on cooling was taken as the last configuration from heating to 700 K; this structure contained lithium defects that had formed at high temperature and a defected initial structure is unavoidable in starting the calculation from a high-temperature phase. In cooling rapidly from 700–300 K, four defects were recovered in the low-temperature phase. The pathways taken by lithium through the structure in the defect formations are mapped out in Figures 4.23, 4.24 and 4.25. These are a simplified alternative to Figures 4.6 and 4.16 because of the complexity of lithium migration in cooling; separate lithium migration chains have been connected in the figures. The polyhedra are identified from their triplet index and the two types are presented pictorially with a diamond for octahedra and triangle for tetrahedra. The polyhedra that are coloured-in are occupied by a lithium ion in the final 300 K structure. In a defect-free structure, the tetrahedra are all occupied and octahedra all unoccupied. Initial defects in the starting structure (empty tetrahedra or occupied octahedra) are highlighted by a double outline on the polyhedra symbols. The lithium ions are identified from their original tetrahedra location in the structure. These are indicated in parentheses along with the time of the polyhedra change to the nearest 0.1 ps (except when multiple lithium movements occurred within 0.1 ps). The lithium ion migrations that formed the low-temperature structure are shown from the collective schematics and these are separated based on closed loops of lithium motion considering time. For example, O864 is in both Figure 4.23 and 4.25 because the lithium migrations are 2 ps apart. As anticipated, the majority of movements

occurred in the early stages of cooling at high temperature. The final structure contained four unoccupied tetrahedra: T131, T135, T735 and T771, and four occupied octahedra: O284, O464, O684 and O864.

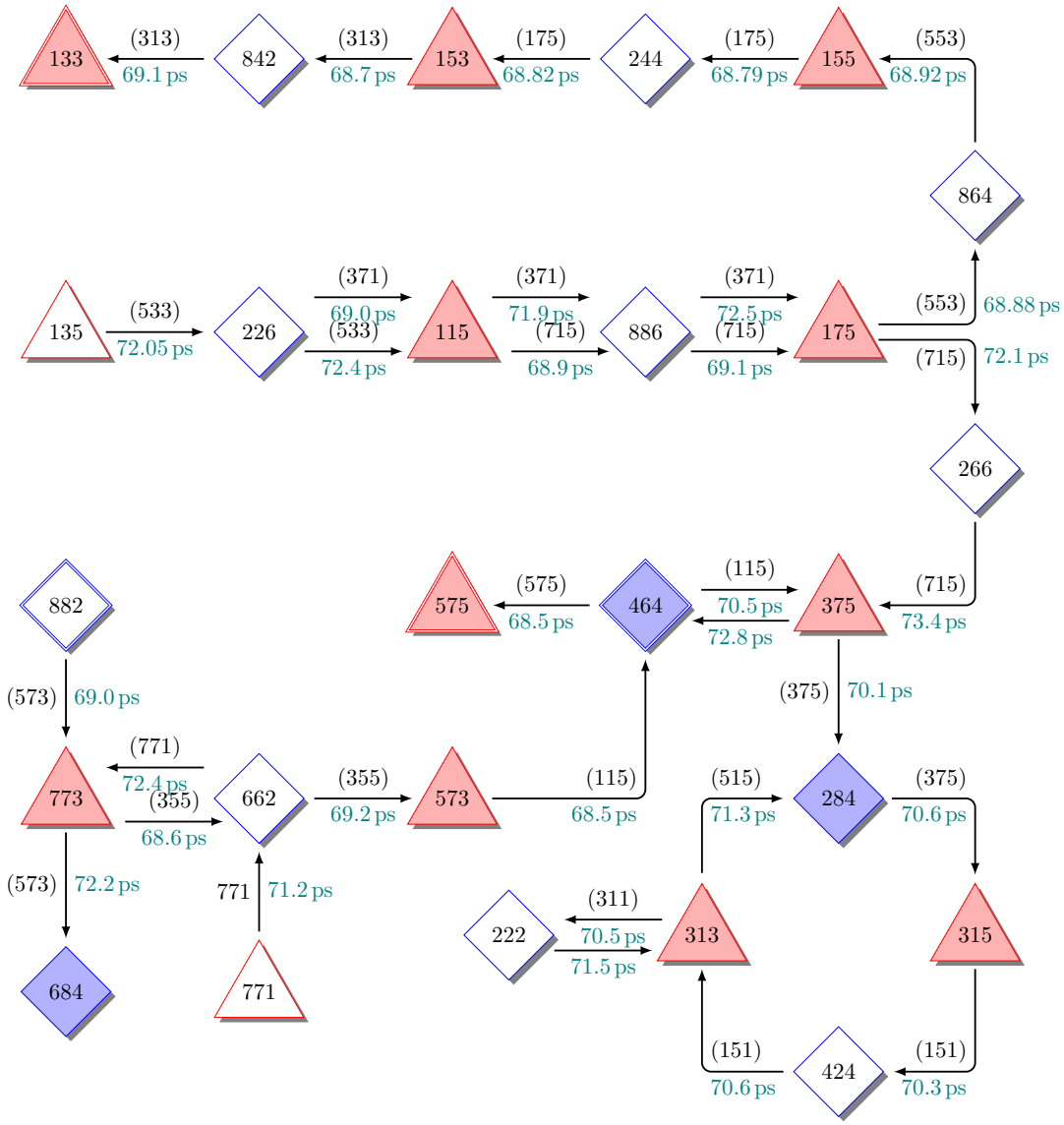

Figure 4.23: Li^+ pathways taken through Li_2NH for defect formations in cooling between 68.5–73.4 ps, 700–455 K. Red triangles denote tetrahedra and blue diamonds octahedra, polyhedra that are coloured-in are occupied by a lithium ion in the 300 K structure. The Li^+ indexes are shown on the arrows in parentheses along with times for the polyhedra changes. T135, T771, O284, O464 and O684 defects from the low-temperature phase are traced.

Figure 4.23 can be split into four distinct events. First at < 70 ps the initial defect in T133

was repaired by Li(313) which resulted in the sequential movement of Li(175) from T155 and Li(553) from T175 into octahedra. Secondly, between 70.1 and 71.5 ps the O284 defect was formed. The initial formation at 70.1 ps was repaired at 70.6 ps and then reformed at 71.3 ps: Li(375, 151, 311 and 515) cycled in that order between nearby polyhedra, and this series of polyhedra changes stopped when the O222 defect was repaired. Thirdly, the O464 defect was formed; this was present in both the initial and end structures. However, the two are shown to be unrelated. The initial defect is best considered to be a temporary occupancy rather than a true defect because an unoccupied tetrahedron (T575) was face-sharing O464, and therefore the "defect" was immediately restored. The O464 defect formation began at 68.5 ps when Li(115) moved from T573 to O464 and the return direction was sealed off by Li(355) occupying T573. Li(115) exited O464 at 70.5 ps and returned at 72.8 ps (480 K) reforming the defect. Lastly, the initial lithium defect in O882 was displaced to O684 at 72.2 ps. T773, which connects O882 to O684, was vacated of its initial lithium during the defect migration and it was then reoccupied by Li(771), leaving T771 unoccupied in the final structure.

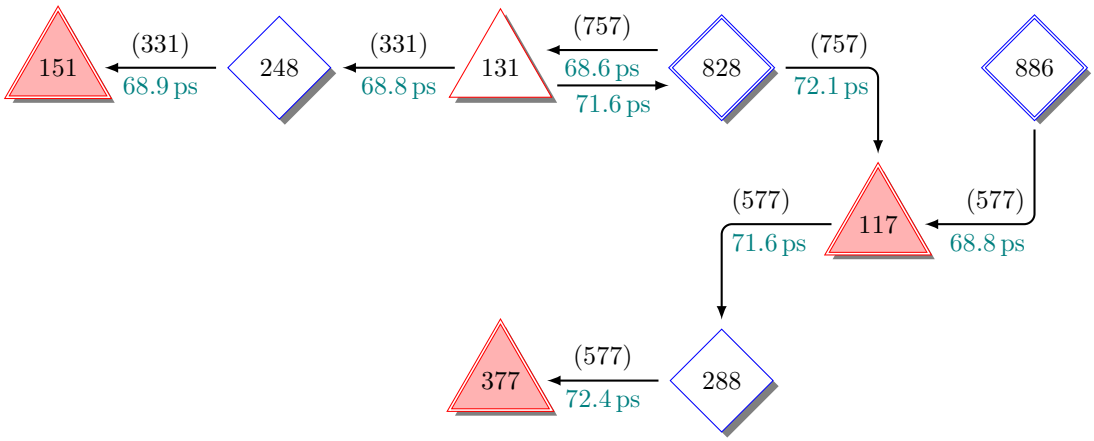

Figure 4.24: Li^+ pathways taken through Li_2NH for defect formations in cooling between 68.6–72.4 ps, 695–505 K. The T131 defect from the low-temperature phase is traced.

Figure 4.24 details the repair of one defect (O828, T151) and the relocation of a tetrahedral vacancy (T377 to T131). The O828/T151 initial defect was swiftly repaired at 68.6–68.9 ps,

with the sequential movement of Li(757) from O828 to T131 and Li(331) from T131 to T151 via O248. Initially O886 was occupied and T117 was unoccupied; this however was a temporary lithium excursion and not a true defect pair because the polyhedra are face-sharing, thus the regular structure was restored. The tetrahedral vacancy in the initial structure was displaced from T377 to T131 by the collective motion of Li(757) and Li(577), between 71.6–72.1 ps. The initial defect in T377 was occupied by Li(577) which had travelled from T117 to T377 via O288. Li(757) in T131 occupied the newly created vacancy in T117 and T131 was not reoccupied.

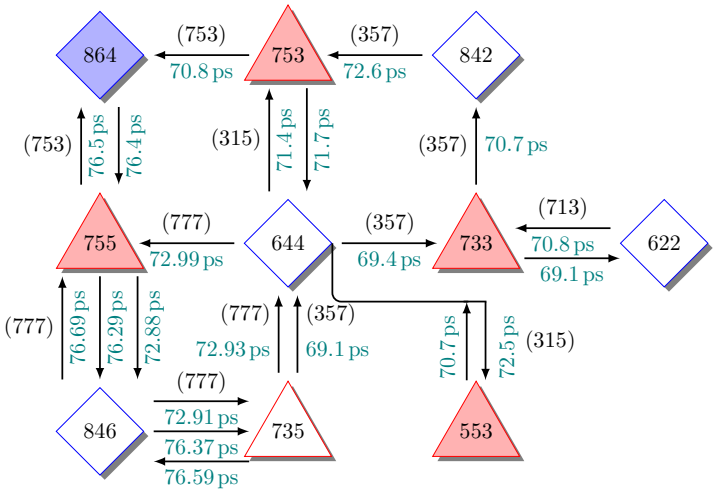

Figure 4.25: Li^+ pathways taken through Li_2NH for defect formations in cooling between 69.1–76.69 ps, 670–290 K. T735 and O864 defects from the low-temperature phase are traced.

Figure 4.25 differs from 4.23 and 4.24 by not containing any polyhedra that were defects in the starting structure, and therefore traces the formation of a defect pair created entirely during the cooling process (T735, O864). The vacancy in T735 was first formed at 69.1 ps and Li(357) which initially occupied it travels a large distance through the structure, from T735 to T753 going via O644, T733 and O842. T735 is then occupied twice by Li(777) as it cycles between T755, O846, T735 and O644, momentarily at 72.91–72.93 ps and again at 76.37–76.59 ps. T735 was not reoccupied after Li(777) exits. O864 was occupied by Li(753)

at 70.8 ps, completing the T735/O864 defect pair. The return pathway for Li(753) was blocked by Li(357), the lithium that caused the initial vacancy in T735. Li(753) remained inside O864 for the majority of the cooling period (5.4 ps), however, at low-temperature O864 was temporarily unoccupied and reoccupied.

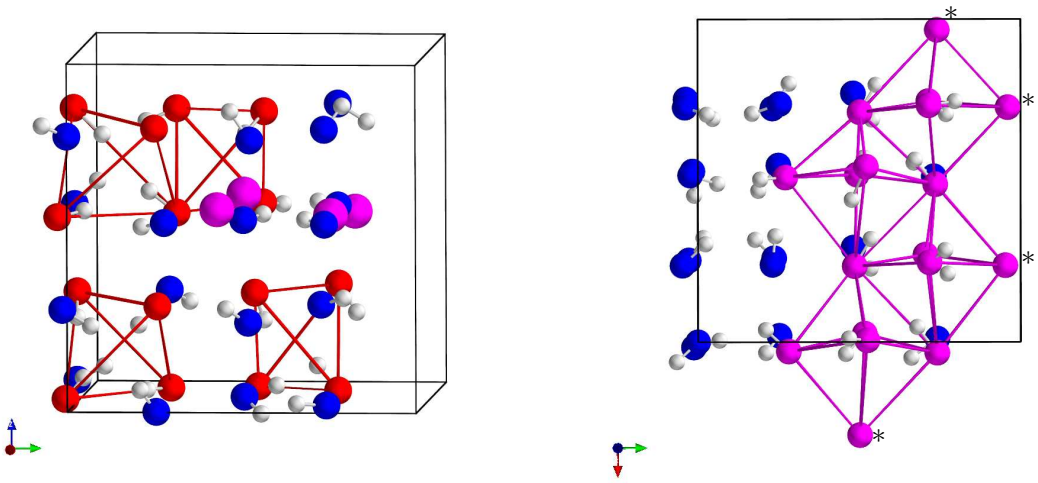

(a) Empty tetrahedra

(b) Li^+ occupied octahedra

Figure 4.26: Li_2NH low-temperature phase obtained in cooling the structure from 700–300 K. Four Frenkel defect pairs are shown, with unoccupied tetrahedra in (a) and occupied octahedra in (b). Only the defect lithium ions are shown. Lithium ions are shown in magenta, nitrogen in blue or the colour of the polyhedra, and hydrogen in white. Atoms in (b) with an asterisk (*) have been repeated from the periodicity of the simulation cell in order to construct the octahedra.

The low-temperature phase from cooling is given in Figure 4.26. The same general features from the first low-temperature structure are observed, vacant tetrahedra Li^+ sites and octahedral Li^+ interstitials; however, this phase differs as it contains four Frenkel defects rather than one. N—H tetrahedral ordering around the vacant Li^+ sites are not observed in their entirety because of the short calculation time, with a longer collection period this feature would be expected to be recovered. The four Li^+ occupied octahedra are edge-sharing and together these form a 1D chain of defects (shown in b). This motif was

previously reported for the low-temperature phase by Herbst and Hector within the $Ima2$ structure.[55] The unoccupied tetrahedra are positioned apart and as far as possible from the chain of octahedra, with the exception of one of the unoccupied tetrahedra which is face-sharing with an occupied octahedra. Symmetry of the low-temperature phase could not be determined from the short time frame of the calculation, due to limited sampling of phase space.

4.9 Conclusions

In this Chapter, the crystal structure of lithium imide has been analysed over the temperature range of 300–700 K in a greater level of detail than previous computational descriptions.[56, 57, 112] The results of the MD simulations can be reliably applied to future computational and experimental work, as the computed structures were in agreement with the existing literature—the experimentally reported high-temperature structure was recovered, with an order-disorder phase transition observed, and the defining low temperature structural features found in all prior low-temperature phases, namely Li^+ in octahedra and tetrahedral N—H ordering, were recovered.

The initial lattice constant of 5.09 Å was too small which created a high-energy system at the start of the calculation. However, the difference in the lattice was beneficial because it annealed in a single Frenkel defect and caused significant structural changes which avoided atoms being trapped in their initial configuration. The low-temperature structure was determined from observations of the ensemble average nitrogen environments to have 2/m point group symmetry, and was subsequently fitted to the space group symmetry $I112/b$. It is a slightly frustrated structure that is a favourable configuration in the absence of being able to form a much larger network of defects. This is a consequence of the small 2×2×2 supercell; the single defect represents a reasonably high defect-concentration. This supercell was the largest that could be computationally afforded and provided the possibility of recovering the $Fd\bar{3}m$ space group; as the best fitted experimental average structure for the low-temperature phase. In rapidly cooling the structure from 700–300 K, a total

of four Frenkel defects were created in the low-temperature phase. These defects in the low-temperature phase are solutions to what is expected to be a number of different similar defect schemes with permissible energies of <700 K. With access to more computational resources, a larger supercell would improve the thermal stability and allow for larger, more complex lithium defect schemes to be explored in the low-temperature structure.

It was not until the model temperature was raised to 500 K that the $I112/b$ structure disappeared. As anticipated, this correlates with the beginning of substantial lithium migration within the structure. A phase transition around 500 K from monoclinic to cubic phases is shown from the ensemble average nitrogen environments. The cubic structure, which was recovered in the 500 K low-volume phase, is observed most clearly from the lithium arrangements along the $\langle 111 \rangle$ directions around nitrogen, but is also shown from a hydrogen disordering that is heading towards being essentially spherically symmetric. By the end of the 500 K run, although the atoms within the cell are locally cubic, the structure is metrically tetragonal. At 600–700 K, the $Fm\bar{3}m$ crystal structure that was reported in the literature was recovered. In this cubic phase, the lithium ions are orientationally fixed but are spatially free to move throughout the structure, while the hydrogen are orientationally disordered (uniformly distributed) but spatially restricted by the ∼1.04 Å nitrogen-hydrogen bond.

The migration of lithium ions has been traced throughout the material and the formation of lithium Frenkel defects is key to the mechanism for observed phase transitions. In addition to ion migration, significant lithium oscillations are observed between occupied tetrahedra and their face-sharing empty octahedra. This is facilitated by the fact that the lithium ions are offset within the tetrahedra towards the centre of the tetrahedral face. The descriptions of lithium ion mobility, although simple for rare events at 300 K, become progressively more difficult to illustrate and describe with increased ion mobility at elevated temperatures. There is inherent complexity in the visualisation of correlated lithium motions at higher temperatures, as extended correlated motions are difficult to represent in two-dimensions.

5

Conclusions and Outlook

The lithium hydride and lithium imide systems investigated in this thesis are key components of the broader Li–N–H system for chemical energy storage. This work follows on from the previous computational investigation of Li_3N as part of the Li–N–H system,[116] with more recent applications of the Li–N–H system in ammonia decomposition and synthesis considered. Li–N–H materials are of importance for both hydrogen storage and in the storage of energy as ammonia, as the lithium imide-amide system has been demonstrated to outperform traditional supported transition metal catalysts for cracking ammonia.[49] Although good atomistic understanding can be accomplished from experiments, computer simulations are able to provide detailed complementary insights at the atomic level. Combined computational and experimental studies are essential for understanding the complexity in these systems, and this thesis complements previous experimental research.[31, 49, 109, 117]

In Chapter 3, the interactions of NH_3 on LiH were investigated as part of the formation mechanism for $LiNH_2$. A surface model was chosen to evaluate these interactions as a more realistic representation than those used in previous studies. This has led to new insights that have been developed from geometric considerations of NH_3 on the LiH surface as the molecular motion across the surface and its stable configuration are related to its distorted tetrahedral shape. The stable configuration (shuttlecock-up) was shown to be held in place by the formation of three points of contact to the surface. Two ammonia molecules were subsequently observed to propagate as a dimer along the surface. This study was extended to molecules on the LiH surface with geometries closely related to ammonia. Water, with only two hydrogen bonds and with the consequent formation of only two points of contact to the surface, was able to move more freely. Methane, however, only experienced repulsive interactions with the surface as a non-polar molecule. Fluorine substitutions in ammonia led to additional insights from disrupting the electronic distributions within the molecules and the addition of steric hindrance. The surface interactions of monofluoroamine were dominated by electrostatic attraction to the single fluorine, while in difluoroamine, dihydrogen bonding was favoured over N—Li because the fluorine ions had significantly altered the stable electronic configuration. Trifluoroamine was so reactive that it dissociated immediately upon contact with the surface. Fluorine substitutions are inherently difficult to handle experimentally due to the increased reactivity and this demonstrates one of the advantages of a computational approach where these systems could be studied with comparative ease. Preferential N—H orientational distributions were identified for imide/amide defects embedded in LiH, and these distributions were observed to form a cubic cage structure in order to avoid the surrounding lithium ions.

In Chapter 4, the two phases of the Li_2NH crystal structure were examined in detail, with a particular emphasis on Li^+ mobility which is of importance for ammonia decomposition in the lithium amide-imide system. The 2×2×2 supercell chosen was a compromise between being small enough to be computable while still being able to replicate the experimental $Fd\bar{3}m$ low-temperature phase. The low-temperature defects observed were consistent with those previously reported with the simultaneous observation of a minority of Li^+ ions on octahedral sites alongside tetrahedral N—H ordering toward the Li^+ vacancy. At

all temperatures, the most stable configuration is for lithium ions to remain inside the tetrahedra. The nature and number of defects in the lithium imide structure has been shown to depend on the temperature gradient as two separate low-temperature phases were obtained; a single defect was observed on heating while four correlated defects forming a 1D chain were observed on cooling. On heating to 700 K, a monoclinic to cubic phase transition ($I112/b \rightarrow Fm\bar{3}m$) was observed with the structural transition around 500 K. The high-temperature phase obtained was cubic both metrically over the time average structure and locally from the atomic arrangements; the lithium ions are orientationally fixed but spatially free while the hydrogen ions are orientationally disordered but spatially restricted.

5.1 Future work

Having completed a study of the LiH surface and Li_2NH structure, this investigation could be extended to Li_2NH surfaces and surface and bulk $LiNH_2$. LiH + NH_3 is the simplest surface model within Li–N–H system for chemical energy storage and the atomic-scale insights from this system provide the foundation for future investigations of NH_3 on more the complex surfaces. The nature of the Li_2NH surface for ammonia-decomposition catalysis is of fundamental importance for the understanding of catalysis mechanisms and the better understanding, obtained in this thesis, of its bulk structure is a prerequisite for the construction of a surface.

Given the limitations of a 2×2×2 supercell of Li_2NH, it would be beneficial to investigate larger Li^+ defect formation schemes and correlated Li^+ motions from multiple supercell configurations, such as 4×4×2 and 4×4×4 supercells. The two different Frenkel defect arrangements recovered in the low-temperature phase were obtained under very different conditions and this has highlighted the importance of the temperature gradient to defect formations within Li_2NH. This should be further explored using larger supercell models. Furthermore, having established the low-force pathways for amide and imide groups embedded in the LiH, this work could be extended to evaluate Li_2NH formation in LiH.

As light-metal amides and imides are a recently discovered class of ammonia decomposition catalyst there are opportunties for similar computational studies of non Li–N–H systems: the precise mechanisms for these ammonia-decomposition systems are unknown, and the majority haven't been studied *in silico*. The Na–N–H system for ammonia decomposition should be studied for comparison to Li–N–H, as sodium amide is unlike all other reported light-metal amides, due to its decomposition product being sodium metal rather than the imide (see equations 1.8 and 1.9). It is not fully understood why sodium metal is formed or how it interacts with ammonia. Computational studies of lithium-calcium imide ($Li_2Ca(NH)_2$) would expand upon the lithium imide work, as a ternary system consisting of both $Li(NH)_4$ tetrahedron (found in Li_2NH) and $Ca(NH)_6$ octahedron. At low-temperatures $Li_2Ca(NH)_2$ exhibits a higher ammonia decomposition rate than Li_2NH and the low-temperature surface structure is unknown.[118] Additionally, this thesis has highlighted the importance of molecular shape to the interactions of NH_3 on the surface of LiH. Further research into how the molecular shape of ammonia affects its motions across similar non Li–N–H surfaces should be performed, including interactions with NaH and KH. Complementary experimental studies by *in situ* Scanning Transmission Electron Microscopy could be used to identify the surface interactions of ammonia proposed from the calculations.

The software written to trace Li^+ mobility in Li_2NH can be used to examine ion migrations in other Li–N–H systems, including non-stoichiometric phases of Li_2NH as the most active form of the catalyst for ammonia decomposition. The mobility of Li^+ ions are essential to the function of many materials and technologies unrelated to the Li–N–H system, such as solid-state lithium batteries. Conductivity measurements are commonly solely performed for the analysis of ion mobility in molecular dynamics simulations, and therefore details of how the ions move within a structure are lost. The code developed to trace Li^+ ions through $(NH)_4$ tetrahedra and $(NH)_6$ octahedra in lithium imide can be easily repurposed to trace ion mobility of different ions through structures unrelated to Li_2NH. This thesis shows ion mobility to be an inherently difficult problem to understand pictorially (especially at higher temperatures), and therefore future work could include the development of Virtual Reality tools in order to better explore this space.

Bibliography

[1] E. S. Raymond, *The Cathedral & the Bazaar: Musings on Linux and Open Source by an Accidental Revolutionary*, "O'Reilly Media, Inc.", 2001.

[2] O. Edenhofer, R. Pichs-Madruga, Y. Sokona, E. Farahani, S. Kadner, K. Seyboth, A. Adler, I. Baum, S. Brunner, P. Eickemeier, B. Kriemann, J. Savolainen, S. Schlmer, C. von Stechow, T. Zwickel and J. C. Minx, *IPCC, 2014: Summary for Policymakers. In: Climate Change 2014: Mitigation of Climate Change. Contribution of Working Group III to the Fifth Assessment Report of the Intergovernmental Panel on Climate Change*, 2014.

[3] V. Masson-Delmotte, P. Zhai, H. O. Portner, D. Roberts, J. Skea, P. R. Shukla, A. Pirani, W. Moufouma-Okia, C. Pean, R. Pidcock, S. Connors, J. B. R. Matthews, Y. Chen, X. Zhou, M. I. Gomis, E. Lonnoy, T. Maycock, M. Tignor and T. Waterfield (eds.), *IPCC, 2018: Global warming of 1.5C. An IPCC Special Report on the impacts of global warming of 1.5C above pre-industrial levels and related global greenhouse gas emission pathways, in the context of strengthening the global response to the threat of climate change, sustainable development, and efforts to eradicate poverty*, 2018.

[4] U. N. F. C. on Climate Change (UNFCC)., *UNFCC*, 2009.

[5] B. Dudley, *BP Statistical Review of World Energy*, 2015, 48.

[6] C. McGlade and P. Ekins, *Nature*, 2015, **517**, 187–190.

[7] N. Dean, *Nature Energy*, 2017, **2**, 17017.

[8] C. Vaalma, D. Buchholz, M. Weil and S. Passerini, *Nature Reviews Materials*, 2018, **3**, 1–11.

[9] K. Mizushima, P. C. Jones, P. J. Wiseman and J. B. Goodenough, *Materials Research Bulletin*, 1980, **15**, 783 – 789.

[10] T. Ogasawara, A. Dbart, M. Holzapfel, P. Novk and P. G. Bruce, *Journal of the American Chemical Society*, 2006, **128**, 1390–1393.

[11] A. Simpson and A. Lutz, *International Journal of Hydrogen Energy*, 2007, **32**, 4811–4820.

[12] L. Schlapbach and A. Zttel, *Nature*, 2001, **414**, 353–358.

[13] Royal Society (Great Britain), *Options for producing low-carbon hydrogen at scale.*, 2018.

[14] M. L. Trudeau, *MRS Bulletin*, 1999, **24**, 23–26.

[15] M. Yadav and Q. Xu, *Energy & Environmental Science*, 2012, **5**, 9698.

[16] U. D. of Energy, *US Department of Energy Office of Energy Efficiency and Renewable Energy and The FreedomCAR and Fuel Partnership*, 2009, 22.

[17] *DOE Hydrogen and Fuel Cells Program: 2011 Annual Merit Review Proceedings - Hydrogen Storage*, 2011, `https://www.hydrogen.energy.gov/annual_review11_storage.html`.

[18] D. S. November 2007, *Fuelling the future: solid phase hydrogen storage*, `eic.rsc.org/feature/fuelling-the-future-solid-phase-hydrogen-storage/2020153.article`.

[19] A. Zttel, *Materials Today*, 2003, **6**, 24 – 33.

[20] A. Zttel, P. Sudan, P. Mauron, T. Kiyobayashi, C. Emmenegger and L. Schlapbach, *International Journal of Hydrogen Energy*, 2002, **27**, 203 – 212.

[21] J. Weitkamp, M. Fritz and S. Ernst, *International Journal of Hydrogen Energy*, 1995, **20**, 967 – 970.

[22] H. W. Langmi, A. Walton, M. M. Al-Mamouri, S. R. Johnson, D. Book, J. D. Speight, P. P. Edwards, I. Gameson, P. A. Anderson and I. R. Harris, *Journal of Alloys and Compounds*, 2003, **356-357**, 710 – 715.

[23] W. I. F. David, *Faraday Discussions*, 2011, **151**, 399.

[24] B. Bogdanovi and M. Schwickardi, *Journal of Alloys and Compounds*, 1997, **253-254**, 1–9.

[25] P. Chen, Z. Xiong, J. Luo, J. Lin and K. L. Tan, *Nature*, 2002, **420**, 302–304.

[26] P. Chen, Z. Xiong, J. Luo, J. Lin and K. L. Tan, *The Journal of Physical Chemistry B*, 2003, **107**, 10967–10970.

[27] D. H. Gregory, *Journal of Materials Chemistry*, 2008, **18**, 2321.

[28] P. Chen and M. Zhu, *Materials Today*, 2008, **11**, 36 – 43.

[29] F. W. Dafert and R. Miklauz, *Monatshefte fr Chemie*, 1910, **31**, 981–996.

[30] J. A. Kilner, S. J. Skinner, S. J. C. Irvine and P. P. Edwards, *Functional Materials for Sustainable Energy Applications*, Elsevier, 2012.

[31] J. W. Makepeace, M. O. Jones, S. K. Callear, P. P. Edwards and W. I. F. David, *Physical Chemistry Chemical Physics*, 2014, **16**, 4061.

[32] S. Isobe, T. Ichikawa, K. Tokoyoda, N. Hanada, H. Leng, H. Fujii and Y. Kojima, *Thermochimica Acta*, 2008, **468**, 35–38.

[33] R. Juza and K. Opp, *Z. Anorg. Allg. Chem.*, 1951, **266**, 313–324.

[34] T. Ichikawa, N. Hanada, S. Isobe, H. Leng and H. Fujii, *The Journal of Physical Chemistry B*, 2004, **108**, 7887–7892.

[35] S. Isobe, T. Ichikawa, S. Hino and H. Fujii, *The Journal of Physical Chemistry B*, 2005, **109**, 14855–14858.

[36] Y. H. Hu and E. Ruckenstein, *The Journal of Physical Chemistry A*, 2003, **107**, 9737–9739.

[37] W. Osborn, T. Markmaitree and L. L. Shaw, *Nanotechnology*, 2009, **20**, 204028.

[38] J. Lamb, D. Chandra, W.-M. Chien, D. Phanon, N. Penin, R. ern and K. Yvon, *The Journal of Physical Chemistry C*, 2011, **115**, 14386–14391.

[39] T. Kar, S. Scheiner and L. Li, *Journal of Molecular Structure: THEOCHEM*, 2008, **857**, 111–114.

[40] A. Yamane, F. Shimojo, K. Hoshino, T. Ichikawa and Y. Kojima, *Journal of Molecular Structure: THEOCHEM*, 2010, **944**, 137–145.

[41] A. Yamane, F. Shimojo, K. Hoshino, T. Ichikawa and Y. Kojima, *Journal of Alloys and Compounds*, 2011, **509**, S728–S731.

[42] W. I. F. David, J. W. Makepeace, S. K. Callear, H. M. A. Hunter, J. D. Taylor, T. J. Wood and M. O. Jones, *Journal of the American Chemical Society*, 2014, **136**, 13082–13085.

[43] J. W. Erisman, M. Sutton, J. Galloway, Z. Klimont and W. Winiwarter, *Nature Geoscience - NAT GEOSCI*, 2008, **1**, 636–639.

[44] S. F. Yin, B. Q. Xu, X. P. Zhou and C. T. Au, *Applied Catalysis A: General*, 2004, **277**, 1 – 9.

[45] S. Yin, B. Xu, S. Wang, C. Ng and C. Au, *Catalysis Letters*, 2004, **96**, 113–116.

[46] R. Z. Srensen, L. J. E. Nielsen, S. Jensen, O. Hansen, T. Johannessen, U. Quaade and C. H. Christensen, *Catalysis Communications*, 2005, **6**, 229 – 232.

[47] A. Klerke, S. K. e. Klitgaard and R. Fehrmann, *Catalysis Letters*, 2009, **130**, 541–546.

[48] J. Larminie, A. Dicks and M. S. McDonald, *Fuel cell systems explained*, J. Wiley Chichester, UK, 2003, vol. 2.

[49] J. W. Makepeace, T. J. Wood, H. M. A. Hunter, M. O. Jones and W. I. F. David, *Chemical Science*, 2015, **6**, 3805–3815.

[50] F. Schth, R. Palkovits, R. Schlgl and D. S. Su, *Energy Environ. Sci.*, 2012, **5**, 6278–6289.

[51] T. Bell and L. Torrente-Murciano, *Topics in Catalysis*, 2016, **59**, 1438–1457.

[52] S. Mukherjee, S. V. Devaguptapu, A. Sviripa, C. R. F. Lund and G. Wu, *Applied Catalysis B: Environmental*, 2018, **226**, 162 – 181.

[53] W. I. F. David, M. O. Jones, D. H. Gregory, C. M. Jewell, S. R. Johnson, A. Walton and P. P. Edwards, *Journal of the American Chemical Society*, 2007, **129**, 1594–1601.

[54] M. P. Balogh, C. Y. Jones, J. Herbst, L. G. Hector and M. Kundrat, *Journal of Alloys and Compounds*, 2006, **420**, 326–336.

[55] J. F. Herbst and L. G. Hector, *Physical Review B*, 2005, **72**, 125120.

[56] G. Miceli, M. Ceriotti, M. Bernasconi and M. Parrinello, *Physical Review B*, 2011, **83**, 054119.

[57] T. Mueller and G. Ceder, *Physical Review B*, 2010, **82**, 174307.

[58] S. Chen, S. Perathoner, C. Ampelli and G. Centi, in *Horizons in Sustainable Industrial Chemistry and Catalysis*, ed. S. Albonetti, S. Perathoner and E. A. Quadrelli, Elsevier, 2019, vol. 178 of Studies in Surface Science and Catalysis, pp. 31 – 46.

[59] D. Zhu, L. Zhang, R. E. Ruther and R. J. Hamers, *Nature Materials*, 2013, **12**, 836.

[60] H. Li, J. Shang, Z. Ai and L. Zhang, *Journal of the American Chemical Society*, 2015, **137**, 6393–6399.

[61] S. Licht, B. Cui, B. Wang, F.-F. Li, J. Lau and S. Liu, *Science*, 2014, **345**, 637–640.

[62] S. Chen, S. Perathoner, C. Ampelli, C. Mebrahtu, D. Su and G. Centi, *Angewandte Chemie International Edition*, 2017, **56**, 2699–2703.

[63] W. Gao, J. Guo, P. Wang, Q. Wang, F. Chang, Q. Pei, W. Zhang, L. Liu and P. Chen, *Nature Energy*, 2018, **3**, 1067–1075.

[64] K. Murrell and D. Holroyd, *The Harwell Dekatron Computer*, The National Museum of Computing, 2013.

[65] E. Strohmaier, J. Dongarra, H. Simon and M. Meuer, *TOP500 List - November 2018 | TOP500 Supercomputer Sites*, 2018, `https://www.top500.org/list/2018/11/`.

[66] G. van Rossum, *Technical Report CS-R9526*, 1995.

[67] K. J. Millman and M. Aivazis, *Computing in Science Engineering*, 2011, **13**, 9–12.

[68] T. E. Oliphant, *Computing in Science Engineering*, 2007, **9**, 10–20.

[69] S. van der Walt, S. C. Colbert and G. Varoquaux, *Computing in Science Engineering*, 2011, **13**, 22–30.

[70] W. McKinney, *Proc. of the 9th Python in science conf.*, 2010, 6.

[71] J. D. Hunter, *Computing in Science Engineering*, 2007, **9**, 90–95.

[72] P. Ramachandran and G. Varoquaux, *Computing in Science & Engineering*, 2011, **13**, 40–51.

[73] F. Perez and B. E. Granger, *Computing in Science Engineering*, 2007, **9**, 21–29.

[74] F. Giustino, *Materials Modelling using Density Functional Theory: Properties and Predictions*, Oxford University Press, 2014.

[75] D. S. Sholl and J. A. Steckel, *Density Functional Theory*, John Wiley & Sons, Inc., 2009.

[76] P. A. M. Dirac, *Proceedings of the Royal Society A: Mathematical, Physical and Engineering Sciences*, 1929, **123**, 714–733.

[77] P. Hohenberg and W. Kohn, *Physical Review*, 1964, **136**, B864–B871.

[78] W. Kohn and L. J. Sham, *Physical Review*, 1965, **140**, A1133–A1138.

[79] J. P. Perdew, AIP Conference Proceedings, Antwerp (Belgium), 2001, pp. 1–20.

[80] F. School, *Jacob's Ladder*, 1490.

[81] D. M. Ceperley and B. J. Alder, *Physical Review Letters*, 1980, **45**, 566–569.

[82] F. Herman, J. P. Van Dyke and I. B. Ortenburger, *Physical Review Letters*, 1969, **22**, 807–811.

[83] J. P. Perdew, K. Burke and M. Ernzerhof, *Physical Review Letters*, 1996, **77**, 3865–3868.

[84] CASTEP, *Setting the exchange-correlation functional*, `https://www.tcm.phy.cam.ac.uk/castep/documentation/WebHelp/content/modules/castep/tskcastepsetelecxc.htm`.

[85] J. VandeVondele, M. Krack, F. Mohamed, M. Parrinello, T. Chassaing and J. Hutter, *Computer Physics Communications*, 2005, **167**, 103–128.

[86] D. Vanderbilt, *Physical Review B*, 1990, **41**, 7892–7895.

[87] B. G. Pfrommer, M. Cote, S. G. Louie and M. L. Cohen, *J. Comput. Phys.*, 1997, **131**, 233–240.

[88] L. Verlet, *Physical Review*, 1967, **159**, 98–103.

[89] W. C. Swope, H. C. Andersen, P. H. Berens and K. R. Wilson, *The Journal of Chemical Physics*, 1982, **76**, 637–649.

[90] R. Feynman, A. Hibbs and D. Styer, *Quantum Mechanics and Path Integrals*, Dover Publications, 2010.

[91] M. J. Gillan, D. Alf and A. Michaelides, *The Journal of Chemical Physics*, 2016, **144**, 130901.

[92] S. J. Clark, M. D. Segall, C. J. Pickard, P. J. Hasnip, M. I. J. Probert, K. Refson and M. C. Payne, *Zeitschrift fr Kristallographie - Crystalline Materials*, 2005, **220**, 567–570.

[93] J. Hutter, M. Iannuzzi, F. Schiffmann and J. VandeVondele, *Wiley Interdisciplinary Reviews: Computational Molecular Science*, 2014, **4**, 15–25.

[94] J. Bijvoet and A. Karssen, Proceedings of the Koninklijke Nederlandse Academie van Wetenschappen, 1922, pp. 27–27.

[95] A. Lazicki, P. Loubeyre, F. Occelli, R. J. Hemley and M. Mezouar, *Physical Review B*, 2012, **85**, 054103.

[96] H. J. Monkhorst and J. D. Pack, *Phys. Rev. B*, 1976, **13**, 5188–5192.

[97] W. Sun and G. Ceder, *Surface Science*, 2013, **617**, 53–59.

[98] P. W. Tasker, *Journal of Physics C: Solid State Physics*, 1979, **12**, 4977–4984.

[99] N. V. Skorodumova, K. Hermansson and B. Johansson, *Physical Review B*, 2005, **72**, 125414.

[100] S. Sawada and K. Nakamura, *Journal of Physics C: Solid State Physics*, 1979, **12**, 1183–1193.

[101] Y. W. Tsang and L. M. Falicov, *Physical Review B*, 1975, **12**, 2441–2447.

[102] M. R. Welton-Cook and M. Prutton, *Surface Science*, 1977, **64**, 633 – 640.

[103] L. Bengtsson, *Physical Review B*, 1999, **59**, 12301–12304.

[104] R. D. Shannon, *Acta Crystallographica Section A*, 1976, **32**, 751–767.

[105] D. K. Smith and H. R. Leider, *Journal of Applied Crystallography*, 1968, **1**, 246–249.

[106] W. I. F. David, R. M. Ibberson and T. Matsuo, *Proceedings of the Royal Society A: Mathematical, Physical and Engineering Sciences*, 1993, **442**, 18.

[107] B. Cordero, V. Gmez, A. E. Platero-Prats, M. Revs, J. Echeverra, E. Cremades, F. Barragn and S. Alvarez, *Dalton Transactions*, 2008, 2832.

[108] A. D. Mulliner, P. C. Aeberhard, P. D. Battle, W. I. F. David and K. Refson, *Physical Chemistry Chemical Physics*, 2015, **17**, 21470–21475.

[109] J. W. Makepeace and W. I. F. David, *The Journal of Physical Chemistry C*, 2017, **121**, 12010–12017.

[110] M. Deserno, *Max-Planck-Institut fr Polymerforschung:German*, 2004, 1.

[111] R. A. Forman, *The Journal of Chemical Physics*, 1971, **55**, 1987–1988.

[112] G. Miceli, M. Ceriotti, S. Angioletti-Uberti, M. Bernasconi and M. Parrinello, *The Journal of Physical Chemistry C*, 2011, **115**, 7076–7080.

[113] T. Noritake, H. Nozaki, M. Aoki, S. Towata, G. Kitahara, Y. Nakamori and S. Orimo, *Journal of Alloys and Compounds*, 2005, **393**, 264–268.

[114] K. Ohoyama, Y. Nakamori, S. Orimo and K. Yamada, *Journal of the Physical Society of Japan*, 2005, **74**, 483–487.

[115] K. Momma and F. Izumi, *Journal of Applied Crystallography*, 2011, **44**, 1272–1276.

[116] A. D. Mulliner, P. D. Battle, W. I. F. David and K. Refson, *Phys. Chem. Chem. Phys.*, 2016, **18**, 5605–5613.

[117] J. W. Makepeace, T. J. Wood, P. L. Marks, R. I. Smith, C. A. Murray and W. I. F. David, *Phys. Chem. Chem. Phys.*, 2018, **20**, 22689–22697.

[118] J. W. Makepeace, H. M. A. Hunter, T. J. Wood, R. I. Smith, C. A. Murray and W. I. F. David, *Faraday Discussions*, 2016, **188**, 525–544.

Appendix A: Lithium hydride

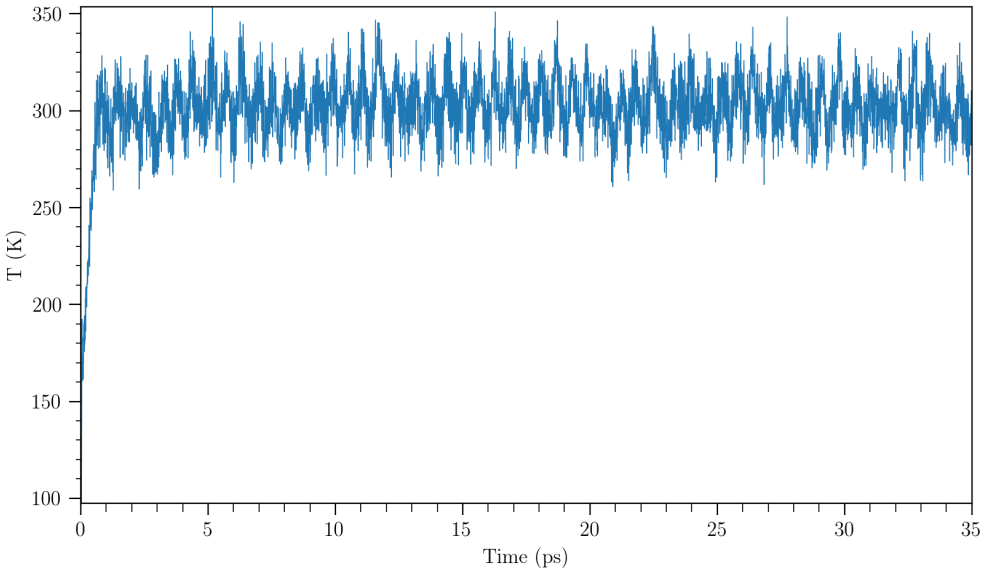

Figure A.1: Computationally evaluated temperature of NH_3 on the LiH surface at 300 K.

Appendix B: Lithium imide

Figure B.1: Connectivity of octahedra to tetrahedra.

O.	T.	O.	T.
222	111, 311, 131, 331, 113, 313, 133, 333	226	115, 315, 135, 335, 117, 317, 137, 337
622	511, 711, 531, 731, 513, 713, 533, 733	626	515, 715, 535, 735, 517, 717, 537, 737
442	331, 531, 351, 551, 333, 533, 353, 553	446	335, 535, 355, 555, 337, 537, 357, 557
842	131, 731, 151, 751, 133, 733, 153, 753	846	135, 735, 155, 755, 137, 737, 157, 757
262	151, 351, 171, 371, 153, 353, 173, 373	266	155, 355, 175, 375, 157, 357, 177, 377
662	551, 751, 571, 771, 553, 753, 573, 773	666	555, 755, 575, 775, 557, 757, 577, 777
482	311, 511, 371, 571, 313, 513, 373, 573	486	315, 515, 375, 575, 317, 517, 377, 577
882	111, 711, 171, 771, 113, 713, 173, 773	886	115, 715, 175, 775, 117, 717, 177, 777
424	313, 513, 333, 533, 315, 515, 335, 535	428	311, 511, 331, 531, 317, 517, 337, 537
824	113, 713, 133, 733, 115, 715, 135, 735	828	111, 711, 131, 731, 117, 717, 137, 737
244	133, 333, 153, 353, 135, 335, 155, 355	248	131, 331, 151, 351, 137, 337, 157, 357
644	533, 733, 553, 753, 535, 735, 555, 755	648	531, 731, 551, 751, 537, 737, 557, 757
464	353, 553, 373, 573, 355, 555, 375, 575	468	351, 551, 371, 571, 357, 557, 377, 577
864	153, 753, 173, 773, 155, 755, 175, 775	868	151, 751, 171, 771, 157, 757, 177, 777
284	113, 313, 173, 373, 115, 315, 175, 375	288	111, 311, 171, 371, 117, 317, 177, 377
684	513, 713, 573, 773, 515, 715, 575, 775	688	511, 711, 571, 771, 517, 717, 577, 777

Figure B.2: Connectivity of tetrahedra to octahedra.

T.	O.	T.	O.	T.	O.
111	288, 828, 882, 222	533	622, 442, 424, 644	175	864, 266, 284, 886
311	288, 428, 482, 222	733	622, 644, 842, 824	375	464, 266, 284, 486
511	688, 428, 482, 622	153	842, 262, 244, 864	575	464, 666, 684, 486
711	688, 622, 828, 882	353	442, 262, 244, 464	775	666, 684, 864, 886
131	828, 248, 222, 842	553	442, 662, 644, 464	117	886, 226, 288, 828
331	428, 248, 222, 442	753	662, 644, 842, 864	317	486, 226, 288, 428
531	428, 648, 622, 442	173	262, 864, 882, 284	517	486, 626, 688, 428
731	648, 622, 828, 842	373	262, 464, 482, 284	717	626, 688, 886, 828
151	248, 868, 842, 262	573	662, 464, 482, 684	137	226, 846, 828, 248
351	248, 468, 442, 262	773	662, 684, 864, 882	337	226, 446, 428, 248
551	648, 468, 442, 662	115	284, 824, 886, 226	537	626, 446, 428, 648
751	648, 662, 868, 842	315	284, 424, 486, 226	737	626, 648, 846, 828
171	868, 262, 288, 882	515	684, 424, 486, 626	157	846, 266, 248, 868
371	468, 262, 288, 482	715	684, 626, 824, 886	357	446, 266, 248, 468
571	468, 662, 688, 482	135	824, 244, 226, 846	557	446, 666, 648, 468
771	662, 688, 868, 882	335	424, 244, 226, 446	757	666, 648, 846, 868
113	882, 222, 284, 824	535	424, 644, 626, 446	177	266, 868, 886, 288
313	482, 222, 284, 424	735	644, 626, 824, 846	377	266, 468, 486, 288
513	482, 622, 684, 424	155	244, 864, 846, 266	577	666, 468, 486, 688
713	622, 684, 882, 824	355	244, 464, 446, 266	777	666, 688, 868, 886
133	222, 842, 824, 244	555	644, 464, 446, 666		
333	222, 442, 424, 244	755	644, 666, 864, 846		

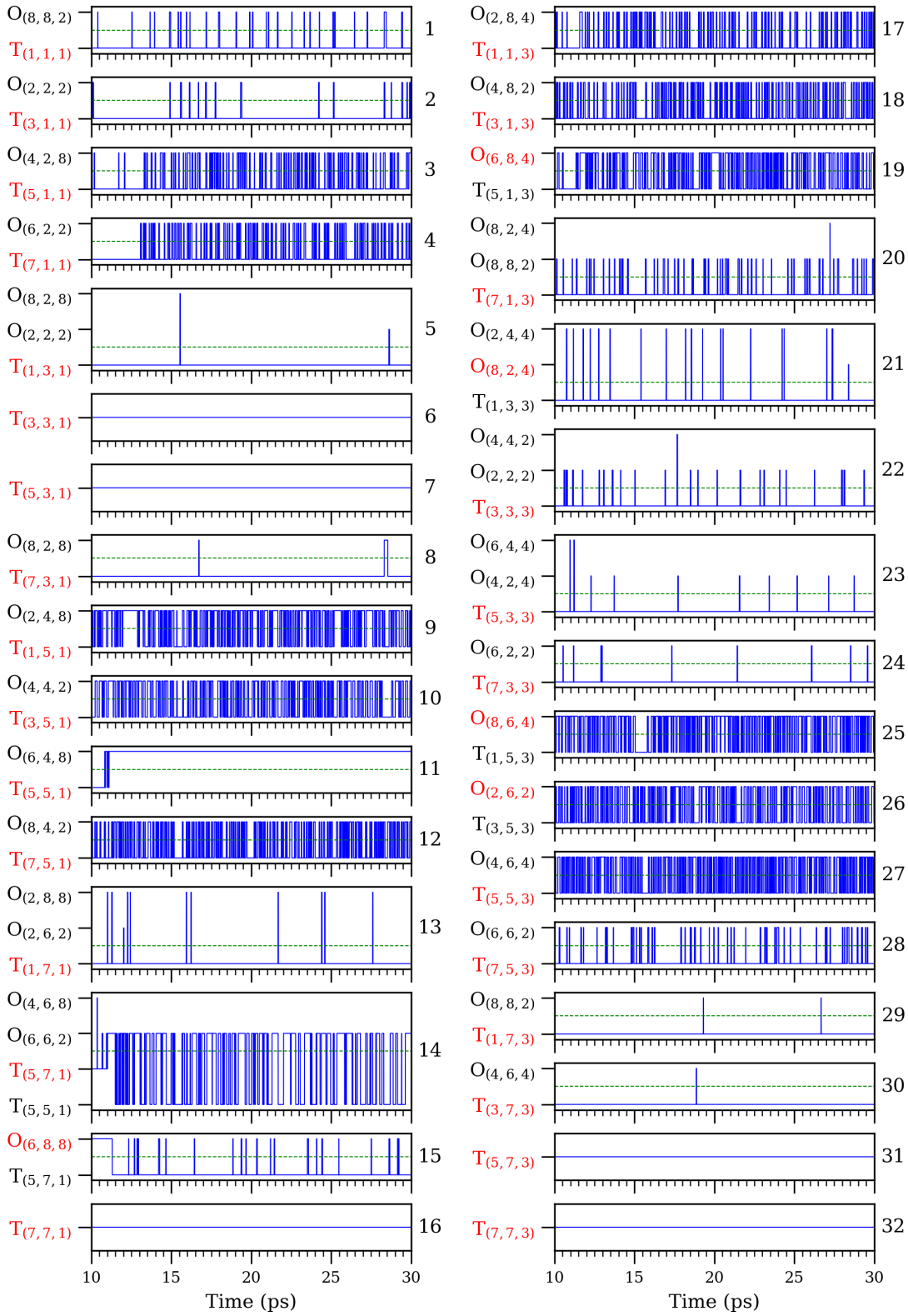

Figure B.3: All lithium movement over 20 ps between face-sharing tetrahedra and octahedra at 300 K. Figure 1 of 2.

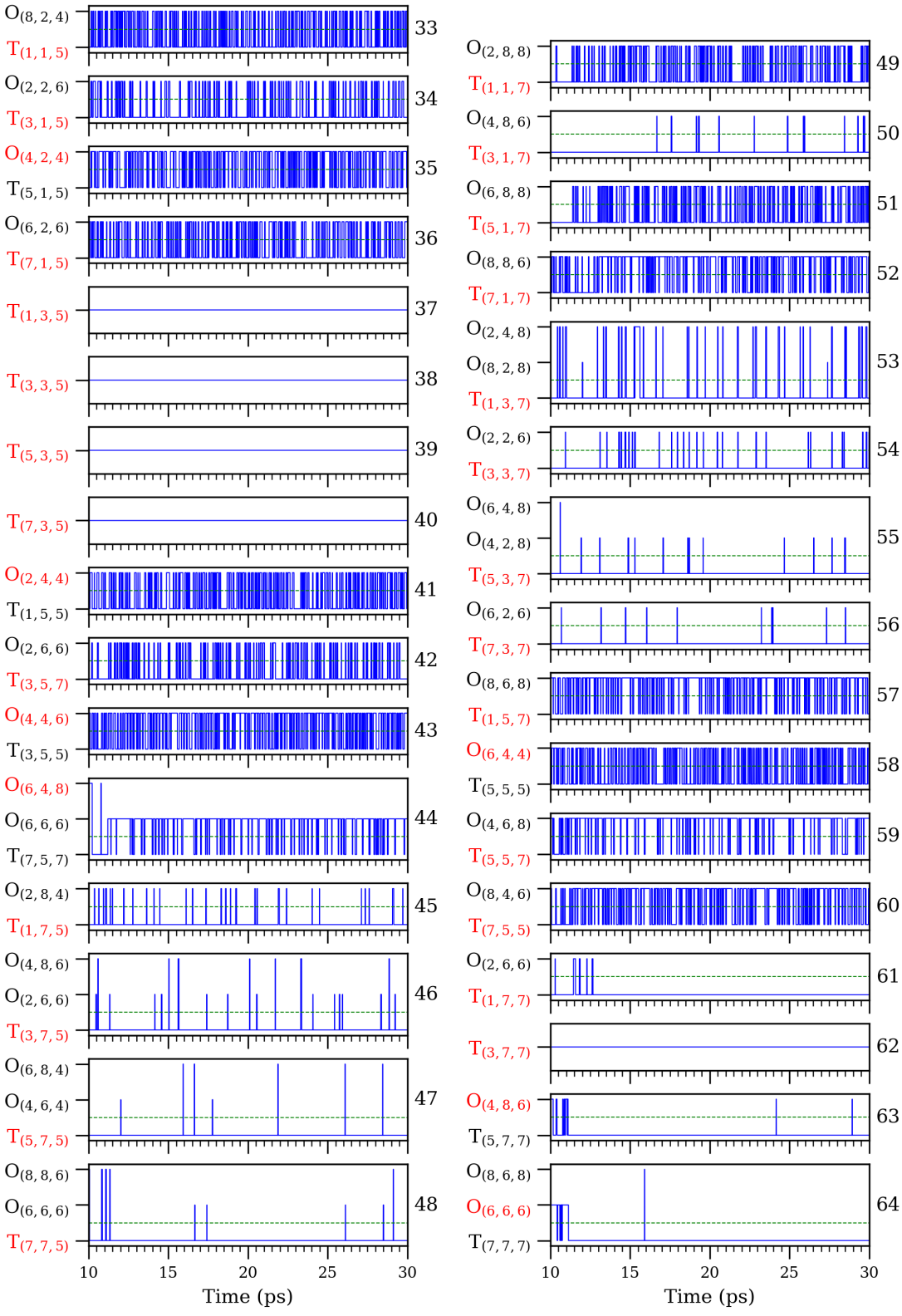

Figure B.4: All lithium movement over 20 ps between face-sharing tetrahedra and octahedra at 300 K. Figure 2 of 2.

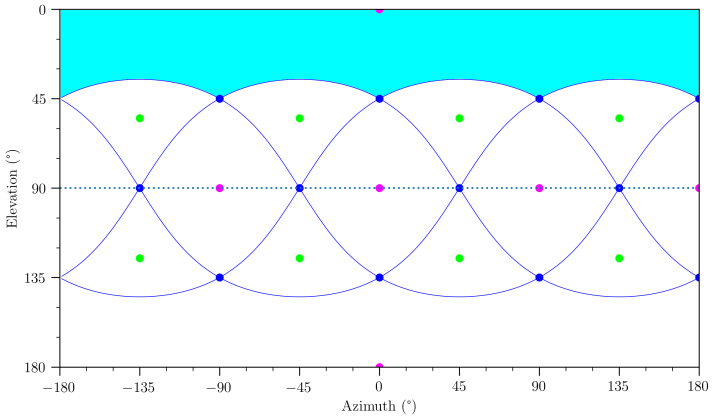

(a)

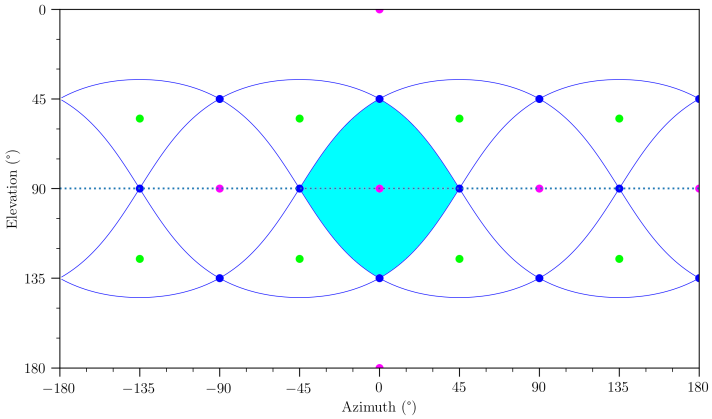

(b)

Figure B.5: Distortion in Mercator projections. The highlighted regions in (a) and (b) are the same physical size on a sphere.

Mercator projections are used in this thesis to represent spherical distributions of atoms in two dimensions. Two octahedral faces from the lithium imide structure are highlighted in Figure B.5; these are dimensionally identical, however, on the projection the region in (a) is much larger than (b). In Mercator projections objects are larger the further they are from the equator and distortions are an inherent problem of any two-dimensional representation of a sphere.

Appendix C: List of Simulations

Figure C.1: (Chapter 3) Alkali metal hydride surfaces.

Calculation	**Structure**	**Description**	**Temp. (K)**	**Software package**	**Pseudo-potential**	**Cutoff (eV)**
Geometry Optimisation	$Li_{126}H_{126}$	7-layer asymmetric slab with the bottom 2-layers fixed.	0	CASTEP	Ultrasoft	750
Geometry Optimisation	$Na_{126}H_{126}$	7-layer asymmetric slab with the bottom 2-layers fixed.	0	CASTEP	Ultrasoft	750
Geometry Optimisation	$K_{126}H_{126}$	7-layer asymmetric slab with the bottom 2-layers fixed.	0	CASTEP	Ultrasoft	750
Geometry Optimisation	$Rb_{126}H_{126}$	7-layer asymmetric slab with the bottom 2-layers fixed.	0	CASTEP	Ultrasoft	750
Geometry Optimisation	$Cs_{126}H_{126}$	7-layer asymmetric slab with the bottom 2-layers fixed.	0	CASTEP	Ultrasoft	750

Figure C.2: (Chapter 3) Molecules on the surface of lithium hydride.

Calculation	**Molecule**		**Surface structure**	**Description**	**Temp. (K)**	**Software package**	**Basis set**	**Pseudo-potential**	**Cutoff (Ry)**	**Time (ps)**
MD	1	NH_3	$Li_{250}H_{250}$	Molecules on LiH 5-layer asymmetric slab with bottom 2-layers fixed.	300	CP2K	DZVP	GTH	320	30
MD	2	NH_3	$Li_{250}H_{250}$	Molecules on LiH 5-layer asymmetric slab with the bottom 2-layers fixed.	300	CP2K	DZVP	GTH	320	20
MD	2	NH_3	$Li_{250}H_{250}$	Molecules on LiH 5-layer asymmetric slab with the bottom 2-layers fixed.	300	CP2K	DZVP	GTH	320	35
MD	9	NH_3	$Li_{250}H_{250}$	Molecules on LiH 5-layer asymmetric slab with the bottom 2-layers fixed.	300	CP2K	DZVP	GTH	320	20
MD	1	H_2O	$Li_{250}H_{250}$	Molecules on LiH 5-layer asymmetric slab with the bottom 2-layers fixed.	300	CP2K	DZVP	GTH	320	30
MD	2	H_2O	$Li_{250}H_{250}$	Molecules on LiH 5-layer asymmetric slab with the bottom 2-layers fixed.	300	CP2K	DZVP	GTH	320	29.95
MD	2	CH_4	$Li_{250}H_{250}$	Molecules on LiH 5-layer asymmetric slab with the bottom 2-layers fixed.	300	CP2K	DZVP	GTH	320	10
MD	1	NFH_2	$Li_{250}H_{250}$	Molecules on LiH 5-layer asymmetric slab with the bottom 2-layers fixed.	300	CP2K	DZVP	GTH	500	24.18
MD	1	NF_2H	$Li_{250}H_{250}$	Molecules on LiH 5-layer asymmetric slab with the bottom 2-layers fixed.	300	CP2K	DZVP	GTH	500	24.44
MD	2	NF_2H	$Li_{250}H_{250}$	Molecules on LiH 5-layer asymmetric slab with the bottom 2-layers fixed.	300	CP2K	DZVP	GTH	500	10
MD	1	NF_3	$Li_{250}H_{250}$	Molecules on LiH 5-layer asymmetric slab with the bottom 2-layers fixed.	300	CP2K	DZVP	GTH	500	3.66
MD	2	NF_3	$Li_{250}H_{250}$	Molecules on LiH 5-layer asymmetric slab with the bottom 2-layers fixed.	300	CP2K	DZVP	GTH	500	3.75

Figure C.3: (Chapter 3) Amide/imide defects in lithium hydride.

Calculation	**Structure**	**Description**	**Temp. (K)**	**Software package**	**Basis set**	**Pseudo-potential**	**Cutoff**	**Time (ps)**
MD	$Li_{250}H_{251}N$	Amide embedded on the surface of a LiH 5-layer asymmetric slab with the bottom 2-layers fixed.	300	CP2K	DZVP	GTH	320 Ry	30
MD	$Li_{250}H_{251}N$	Amide embedded one layer beneath the surface of a LiH 5-layer asymmetric slab with the bottom 2-layers fixed.	300	CP2K	DZVP	GTH	320 Ry	30
Single point	$Li_{65}H_{64}N$	400 separate calculations to sample N—H orientations of an imide defect inside bulk LiH.	0	CASTEP	–	Ultrasoft	750 eV	–
Single point	$Li_{65}H_{66}N$	400 separate calculations to sample N—H orientations of an amide defect inside bulk LiH.	0	CASTEP	–	Ultrasoft	750 eV	–

Figure C.4: (Chapter 4) Lithium imide structure.

Calculation	**Structure**	**Description**	**Temp. (K)**	**Software package**	**Basis set**	**Pseudo-potential**	**Cutoff (Ry)**	**Time (ps)**
MD	$Li_{64}(NH)_{32}$	Lithium imide ($Fm\bar{3}m$ starting structure) heated in 100 K steps.	300–700	CP2K	DZVP	GTH	320	68.45
MD	$Li_{64}(NH)_{32}$	Additional data collected in heating lithium imide.	300	CP2K	DZVP	GTH	320	10
MD	$Li_{64}(NH)_{32}$	Additional data collected in heating lithium imide.	600	CP2K	DZVP	GTH	320	5
MD	$Li_{64}(NH)_{32}$	Lithium imide cooled rapidly.	700–300	CP2K	DZVP	GTH	320	8.4

Appendix D: List of Software

Short Description	**Function**	**Additional Comments**
Batch create calculations files	Copies a template calculation (user created) and generates a series of convergence tests from a set input parameters chosen by the user: either a set of k-points or cut-off energies.	Written in BASH.
Batch submit calculations	Iterates through subfolders and submits calculations to the server job queue. The processor core count and simulation run times are hard coded by the user. It is primarily intended for convergence testing.	Written in BASH.
Superimpose a grid over an image for analysis	Superimposes a fine grid over an image so that the location of the points on a graph can be identified. Pixel dimensions of the original image are used to measure the grid.	
Plot data in 3D	Creates 3D models from input atomic coordinates. Individual scripts are written for each scene rendered.	Mayavi 3D plotting package used.
Construct the surface of a sphere	Creates a polygon mesh to approximate the 3D surface of a sphere from a set of coordinate points (atomic positions, typically hydrogen) using Delaunay triangulation. A colour map is constructed and either the forces or histogram counts are projected onto the polygon mesh.	Mayavi 3D plotting package used.
Constructs imide and amide distributions	Generates regularly spaced coordinates on the surface of a sphere from the implementation of Deserno's algorithm. This create a uniform imide distribution. For amide distributions, the first hydrogen is taken from the uniform imide distribution, and the second is generated from a random point along a circle that is drawn 102° from the first hydrogen.	
Track Li^+ mobility in Li_2NH	First, polyhedra are constructed from the starting configuration in the trajectory file to determine how the nitrogen sub-lattice is connected—with the atoms assigned an index grouped by their respective elements. Looking from each lithium ion the 4 closest nitrogen atoms that make up the individual tetrahedron are identified, and their indices stored as lists (of length 4). An array of periodic cell additions is created to account for the edge cases where the nearest nitrogen atoms to a lithium are not located in the same period. Tetrahedron indices are calculated to account for the	**Written with Dr T. Wood.**

	direction of the 64 tetrahedra with respect to one another (i.e. the index triplets in Figure 4.4). This entire procedure is repeated for the 32 octahedra: with the indices of the nitrogen in each octahedron stored as lists (of length 6), periodic cell additions and the octahedron indices determined. Secondly, the connectivity between indexed polyhedra is calculated. Tetrahedron-tetrahedron connectivity is by edge-sharing and therefore each tetrahedron is connected to 6 others: this is stored as 64 lists each containing 6 tetrahedra indices along with tetrahedron-tetrahedron directional relationships. Tetrahedron-octahedron connectivity is by face-sharing, each tetrahedron is connected to 4 octahedra, and each octahedron to 8 tetrahedra. This connectivity is calculated in both directions and stored in lists along with tetrahedron-octahedron directional relationships. Octahedron-octahedron edge-sharing connectivity is also calculated, with each octahedron connected to 12 octahedra. Thirdly, having completely indexed the structure, with the relationships of the atoms in the polyhedra, polyhedra positions and connectivities determined, the lithium movements between polyhedra are calculated. Iteratively at every time step the polyhedron locations for all of the lithium within the structure are determined. The polyhedra connectivities are used to reduce the computational costs, as lithium can only move between connected polyhedra in 0.5 fs (i.e. a single polyhedron). An output file is created detailing every polyhedra change for the lithium, including the time step and any periodic adjustments for the polyhedra. Lastly, the compute polyhedra changes file and lists of polyhedra connectivities are used to construct plots of lithium migrations over time. The polyhedra connectivities function as search directions to locate connected lithium motions.	
Constructs Mercator Projections	2D azimuth and elevation angles are calculated from 3D Cartesian coordinates for the atomic positions. Azimuth and elevation angles are sorted into an ordered array and 2D histograms compute.	